Title	Design of Ag-based Plasmonic Nanocatalysts Using Mesoporous Silica for Efficient Catalysis under Visible Light Irradiation
Author(s)	Verma, Priyanka
Citation	大阪大学, 2017, 博士論文
Version Type	VoR
URL	https://doi.org/10.18910/67148
rights	
Note	

博士学位論文

Design of Ag-based Plasmonic Nanocatalysts Using Mesoporous Silica for Efficient Catalysis under Visible Light Irradiation

（メソポーラスシリカを利用する可視光応答型プラズモニック銀ナノ粒子触媒の設計）

Priyanka VERMA

プリヤンカ バルマ

2017 年 6 月

Division of Materials and Manufacturing Science

Graduate School of Engineering

Osaka University

大阪大学

大学院工学研究科

マテリアル生産科学専攻

CONTENTS

Chapter I

General Introduction

1.1 Background

The emergence of global warming, environmental pollution and energy crisis is becoming one of the major concern to the lives of humanity.[1] The idea of harvesting inexhaustibly abundant sunlight and converting it into chemical energy as a promising, clean and renewable source of energy, demands the development of numerous light conversion technologies.[2] Besides, photovoltaics (solar-to-electrical energy conversion), photocatalysis (solar-to-chemical energy conversion) has also received an enormous attention to address the intermittency of solar radiation.[3-5] In the recent years, tremendous research has been focused on photocatalysis for its promising applications for energy production and environmental remediation.[6-8] It can play a significant role in resolving the challenging problems of today and shaping a more sustainable future via processes like water splitting,[9] CO_2 conversion,[10] CH_4 reforming,[11] artificial photosynthesis,[12] synthesis of drugs,[13] waste water treatment,[14] degradation of organic molecules in aqueous media and in air.[15] In 1972, Fujishima and Honda studied the efficient utilization of UV light by employing TiO_2 photoanode with a Pt counter electrode, initiated a wide spectrum of research in photocatalysis.[16] TiO_2 photocatalyst became very popular due to its oxidizing ability and excellent stability, but its band gap of 3.2 eV limits its potential applications only under UV irradiation (~4 %).[17] Consequently, over the past few decades noble metal (mainly Ag and Au) nanostructures based heterogeneous photocatalyst are being extensively studied to design visible light sensitive composite materials in order to exploit the ~ 44 % of substantial fraction of solar spectrum of light irradiation. Noble metals, possessing novel optical properties, are capable of showing Localized Surface Plasmonic Resonance (LSPR), which is an extraordinary approach to utilize solar energy in plasmonic photocatalysis.[18,19] The study of plasmonic catalysis has seen a tremendous revolution in the last two decades and is continuously emerging as a most rapidly growing research field in nanoscience and technology.[20-22] It deals with the generation and transmission of excitons in metal nanostructures upon irradiating visible light of appropriate wavelength. In this chapter, I will focus on explaining the basics of plasmonics and some of the recent key developments in the design and synthesis of Ag and Au-based functional plasmonic nanocatalysts for their application in various catalytic reactions.

Fundamentals of LSPR

The particles of sizes varying from 1-100 nm known as nanoparticles (NPs), show unique and fascinating characteristics, which are not observed in ordinary materials. The beautiful, bright and attracting colors exhibited by Ag, Au and Cu NPs in solid and colloidal form are primarily due to the physical phenomenon called as Surface Plasmon Resonance (SPR). Metal NPs having size smaller than the wavelength of light display strong dipolar excitation upon visible light irradiation. The collective oscillation of the conduction electrons in the metallic NPs upon irradiation by beam of visible light is known as SPR. A resonance condition establishes when the frequency of incident light matches with the frequency of valence electrons oscillating against the restoring force. The SPR established in nanometer sized structures is called as *Localized Surface Plasmon Resonance (LSPR)*. A representative image of displacement of electronic cloud in plasmonic metal nanosphere is illustrated in Figure 1 (A). The excited plasmons, decay by radiative and non-radiative decay mechanisms are shown in Figure 1 (B). The frequency of oscillation at which resonance takes place is known as Surface Plasmon Energy. This energy is dependent on the dielectric properties of metal, surrounding medium, morphology and size of NPs. The collective oscillations of electrons at nanoscale region generating large field enhancements inside and near the NPs. The field enhancements are widely applicable in innumerous technologies like surface enhanced Raman scattering (SERS), optical sensing, metamaterials, nanophotonics, photothermal therapies, tip-enhanced Raman spectroscopy (TERS), and optical devices. The applications also depend if the optical response occurs at the *surface of bulk metal* or *inside the NPs of metal*. In the case of former, a bulk piece of metal undergoes electromagnetic excitation to produce plasmons on the surface by interacting with the incoming wave, finding its application in SPR spectroscopy, a useful tool for bio-sensing. The latter leads to resonant oscillation of confined electron gas within metal NP, hence leading to overall absorption and scattering phenomenon called as Surface Plasmon Band (SPB).

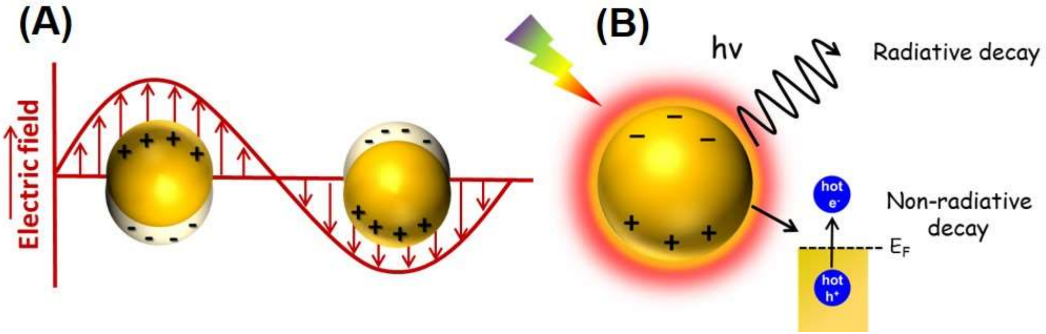

Figure 1. (A) Schematic illustration of LSPR excitation on metallic NPs and (B) decay mechanism of excited plasmons.

History

The emission of electrons from the metal's surface when shined by the light of sufficient intensity, popularly known as *photoelectric effect*. This phenomenon was discovered by Heinrich Hertz in 1887 while carrying out the experiments on illuminating electrodes to create electric sparks. A more detailed explanation was provided by Einstein's in 1905 that light is carried in discrete quantized wavepackets of energy E and frequency v linked by Planck's constant h, $E= hv$. This has led to the conclusion that every metal's surface has a threshold energy or work function, below which electrons cannot be ejected from its surface. In the last two decades, plasmonics has emerged which utilizes the optoelectronic properties of noble metal nanostructures and semiconductors at nanoscale range.[23] The study of conduction electrons of plasmas in metal species is popularly termed as Plasmonics. It is a new flourishing field for integrating optics with nanoscience and technology. Until before three decades, the problem of diffraction limit in optics has restricted its application in nanoscale regimes, but plasmonics has offered a new benchmark to study sub-wavelength optics.

The fundamental idea of plasmonics was started as long as back in the fourth century, when Romans created the famous Lycurgus cup, which is still on display at the British Museum in London.[24] It is extraordinary in many aspects mainly because of its wonderful fabrication and unusual optical properties. The exquisite glass appears green in reflected light and translucent red in transmitted light due to the presence of Ag and Au NPs within the glass matrix. These NPs of different size and morphology scatter the light because of their comparable size to the wavelength of light and produce different colors. It can be cited as one of the astonishing example to begin the history of plasmonics. The first mentioning of the Lycurgus cup was made in 1845, but no detailed description was available until 1950.[25] Another observation in the early studies of plasmonics was initiated by an American astronomer, Wood who described his theories in 1902, popularly known as Wood anomalies. He observed a drop in the illumination of light from maximum to minimum at certain conditions while performing his experiments on studying spectrum of continuous light diffracted by metallic grating. He could not provide a sufficient interpretation for the observation and hence it was named as *singular anomalies* which remained as the most fascinating phenomenon in optics for all twentieth century.[26] Soon after Wood's discovery, several other optics specialists got fascinated towards the problem and proposed their point of view. The first attempt of providing suitable explanation was provided by Rayleigh stating that the anomaly occurs at the wavelength corresponding to the scattering waves passing tangentially from the surface of grating. The grating expression is shown as expression (1), where θ_n represents angle of incidence, θ is the angle of diffraction, λ is the wavelength in vacuum and d is the period of the grating.

$$\sin(\theta_n) = \sin(\theta) + n\lambda / d \qquad (1)$$

After Rayleigh many other scientists including Strong, Fano, Hessel and Oliner have proposed their theories but the modern analysis began only at the beginning of 1970s.

The theoretical understanding of optical properties in metals has its origin from the Maxwell's simple classical equations. The behavior of metal nanostructures in response to the electromagnetic fields can be understood by the electromagnetic theory proposed by Maxwell in 1861.[27] Classical theory is adequate to describe the interaction of metals because of the closely placed energy levels created by the free carriers in comparison to the thermal excitations $k_B T$ at room temperature. Metals are known to be great reflectors under visible region of the spectrum and therefore, the electromagnetic waves cannot propagate through it. At microwave and far-IR region (low frequency) of the spectrum, they can be used as conductors as they can allow only negligible fraction of light to pass through them. Shifting towards little higher frequency regimes towards near IR and visible region, the penetration of light increases and leads to dissipation. At much higher frequency (UV) regions, metals allow the complete propagation of the electromagnetic waves through them and attain dielectric character. In the case of noble metals like Ag and Au, their transitions between electronic bands lead to strong absorption in the regime. The basic electromagnetic equations of Maxwell relating dielectric displacements (**D**), electric fields (**E**), magnetic field (**H**) and magnetic induction (**B**) with external charge ($\boldsymbol{\rho}_{\mathbf{ext}}$) and current densities ($\mathbf{J}_{\mathbf{ext}}$) can be presented in the simplest form (expression 2-5) as follows:

$$\nabla \cdot D = \rho_{ext} \qquad (2)$$

$$\nabla \cdot B = 0 \qquad (3)$$

$$\nabla \times E = -\frac{\partial B}{\partial t} \qquad (4)$$

$$\nabla \times H = J_{ext} + \frac{\partial D}{\partial t} \qquad (5)$$

These equations form the basis of theoretical understanding for studying optical properties of metal nanostructures. The popular expression of plasmonic frequency, shown in equation (6), also found its basis from the Maxwell's equations where ω_p, N, e, ε_0 and m_{eff} represent plasmonic frequency, number density of charge carriers, electronic charge, effective mass and permittivity of free space, respectively. [27]

$$\omega_p = \sqrt{\frac{Ne^2}{\varepsilon_0 m_{eff}}} \qquad (6)$$

The plasma frequency, ω_p, can be defined as the frequency of collective oscillation of free electrons gas presuming that all the electrons are moving in phase. When the frequency of incident light ω_L is less than the plasmonic frequency ω_p the charge carriers screen out the incident light and lead to reflection. On the other hand, if ω_L exceeds the ω_p, complete transmission of light take place since it is too fast for charge carriers to respond to it. A resonance condition is acquired only when ω_L becomes equal to ω_p, known as Localized surface plasmon resonance. The charge permittivity ε_0 generally ignores the dissipation caused by the motion of charge carriers within the material. The modified or the actual permittivity can be calculated as per Drude model by equation (7);

$$\varepsilon_m = 1 - \frac{\omega_p^2}{\omega^2 + i\gamma\omega} \qquad (7)$$

Where γ is the relaxation frequency between different scattering events. The quantum of charge oscillations can be defined as plasmons. These plasmons can undergo decay via radiatively and non-radiatively (Figure 1B). Radiative decay involves the re-emission of photons while non-radiative decay occurs due to creation of electrons and holes (e^-- h^+), also known as Landau damping (LD). LD is considered as a pure quantum mechanical phenomenon in which the transfer of plasmon takes place into an e^-- h^+ pair within a time scale of femtoseconds. Generally, the electron excitation in any solid leads to two types of carriers, an electron (e^-) and hole (h^+). The generation of *hot* electrons takes place only if their energies are larger than the thermal excitations at ambient temperatures.

Plasmonics in conventional catalytic reactions

As of today, metal NPs are being used as industrial catalysts for variety of application reactions, including ammonia synthesis, hydrocarbon reforming, organic coupling, oxidation, hydrogenation and chemoselective reactions. An important key step in any heterogeneous catalytic reaction is its rate-determining step governed by the amount of activation energy that is needed to complete the catalytic process. Various efforts are now being centered in the rational design of catalysts for reducing energy barrier and making robust and energy efficient.

The light interaction of plasmonic NPs creates an electromagnetic dipole through surface plasmonic resonance. This dipole can induce localized heating or the charge carrier generation by enhanced optical field and carry out transformation reaction in the reactants adsorbed on the surface of it. In the case of bimetallic or multi-metallic NPs, the dipole can further polarize the molecules for efficient adsorption and catalytic activity. This polarization can help in utilizing visible light irradiation for activating non-plasmonic reactants and hence reducing the activation energy of the overall process. As per recent reports, in the chemical reactions on the surface of metal NPs (Ag, Au or Cu), diameter < 30 nm, the principle mode of plasmon relaxation is the non-radiative Landau damping by generating energetic charge carriers. These charge carriers can also move within neighboring NPs via tunneling process. In the recent past, there have been many reported examples of plasmon driven photo catalytic reactions, which can find immense significance in industrial applications. For example, an interesting study reports the selectivity improvement of propylene oxide by 20 % on using the SPR effect of Cu NPs.[28] Halas *et al.* has successfully demonstrated the H_2 dissociation on the surface of plasmonic Au NPs in the size range of 5-20 nm at a light intensity of 2 W cm^{-2}.[29] Other few studies explain the plasmon enhanced reaction of nitroaromatics reduction, carbon-carbon coupling, water splitting, hydrogen production from storage materials, benzyl alcohol oxidation and many others.[30-33]

In the next sub-section, I will summarize some of the recent studies reported in the field of plasmon-driven photochemistry for metal NPs supported on inert support material, followed by the possible mechanism of enhancements and applications of some interesting reported results.

Metal nanocatalysts on insulator silica support

The present thesis is focused on the design and synthesis of plasmonic metal NPs supported on inert mesoporous silica materials and the study of their photocatalytic activities under visible light irradiation. Specifically, mesoporous silica, SBA-15 has been utilized to grow metal NPs within the channels of silica because of its large surface area and ordered porous structure. Using metal NPs solely for plasmonic catalysis made them to act as both photosensitive and catalytic component. Significant efforts have recently been devoted to achieve NPs with precise architectures, in which the size, composition and morphology are controlled; changes to these parameters enable the catalytic activity and selectivity of such catalysts to be tuned. Mesoporous-silica-based support materials used in the design and functionalization of photocatalytic systems offer the following advantages: 1) Tunable pore sizes (2–20 nm) and large surface areas which can offer much larger interior space that can accommodate larger organic molecules.; 2) Fine connectivity of the pores facilitating the transfer of organic substrates; 3) Remarkable transparency in the wide wavelength range of UV/Vis spectrum; 4) Amorphous frameworks with a large number of silanol groups for post modification. The above merits can offer opportunities in the development of efficient photocatalytic systems within the world of nanopores. A representative image of metal NPs supported on mesoporous silica synthesized by microwave assisted deposition is shown in Figure 2(A). In the whole thesis, the strategy of synthesizing bimetallic NPs is carried out by LSPR-assisted deposition metal in the presence of visible light irradiation, as represented in Figure 2(B). Supported metal NPs are stable and less vulnerable to aggregation than the free standing metal NPs. Therefore, they can act as potential candidates for large scale implementations. The inert silica support cannot be excited by visible light (less than 3.0 eV) due to its large band gap of ~9.0 eV and hence it is difficult for them to participate in the hot charge carrier generation.

Supported Ag and Au NPs on inert support materials have been researched well as plasmonic photocatalysts due to their extraordinary catalytic activities. The first observation was made by Zhu *et al.* for the oxidation of volatile organic compounds to CO_2 employing Au NPs supported on inert ZrO_2 and SiO_2. It was observed that Au NPs on optically inert SiO_2 was found to be active under red light irradiation, giving clear evidence for plasmon-driven chemical reactions with visible light.[34]

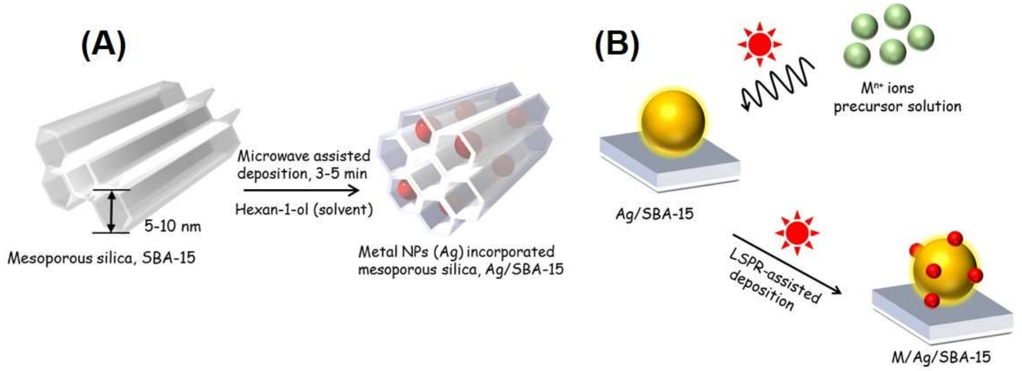

Figure 2. Synthetic strategy of synthesizing (A) plasmonic NPs within SBA-15 and (B) bimetallic NPs by LSPR-assisted deposition under visible light irradiation.

Also, organic dyes, such as sulforhodamine-B (SRB) and methyl orange (MO), could be degraded over supported metal catalysts on insulating oxides (ZrO_2, SiO_2 and zeolites) under visible light irradiation.[35–37] The photocatalytic activity of Au NPs on supported insulators was attributed to be electronic effect in nature. For Au NPs, the transition of 5d electrons to the 6sp band (interband transition) causes considerable UV absorption.[35] In addition, the plasmonic resonance of Au NPs originates from the intraband transition of their 6sp electrons, leading to visible light absorption. Under visible light illumination, the electrons of Au NPs gain energy through plasmonic resonance and migrate to higher potential intraband levels, in which they are then captured by oxygen molecules, leaving the Au NPs with positive charges. To maintain the electric charge neutrality, Au NPs will seize the electrons from the adsorbed organic molecules, thereby oxidizing these organic compounds.

Linic *et al.* observed the 4-fold enhancement in the partial oxidation reaction of ethylene to ethylene oxide as compared to the conventional process employing plasmonic Ag cubes. This reaction is of wide commercial importance due to its billions of worth in the market today. Supported Ag NPs on inert oxides (Ag/zeolite-Y, Ag/ZrO_2 and Ag/SiO_2) also showed good photocatalytic activity in the degradation of organic dyes, such as SRB and methylene blue (MB).[38,39] Through plasmonic excitation of 5sp electrons, the supported Ag NPs even surpassed N-doped TiO_2 in the oxidation of organic molecules under visible light irradiation.[38] A number of reactions have been explored, including the reduction of substituted nitroaromatic compounds on supported Ag nanoparticles illuminated by UV–vis light at an intensity of a few hundred milliwatts per square centimeter. As per one recent report, Au nanorods were synthesized with tips covered with small Pt clusters for the electron-driven hydrogen evolution reaction from water. The reaction was observed at room temperature using methanol as the hole scavenger with low intensity visible light of only a few milliwatts per square centimetre. Other examples include a number of hydrocarbon oxidation and organic coupling reactions on Au–Pd, Ag-Pd and Au–Cu bimetallic nanostructures.[40–44] Other reported studies include the hydrogen production from ammonia borane using bimetallic alloys of CoPd, PdAg and RuNi supported on mesoporous silica illuminated by an ~300 $mWcm^{-2}$ visible light source, and the room-temperature esterification of benzaldehyde with alcohol to produce ethyl benzoate using Ag nanoparticles on various supports illuminated by an ~300 $mW\ cm^{-2}$ visible light source.[45-47] An important strategy of preparing bimetallic NPs containing plasmonic nanostructures (Ag and Au have been used) in combination with another, more chemically reactive metal (for example, Pt and Pd) is continuously being explored for enhanced and efficient activities. In the present thesis, I have also explored various combinations of chemically active metal integrated with plasmonic Ag and Au nanostructures to study their enhancements under visible light irradiation. The mechanistic pathways suggest that it can also induce charge-carrier processes from plasmonic metal to the chemically active metal and then reaction taking place on the surface of latter.

Mechanism of enhancements

As per simple explanation, SPR is the collective oscillation of free electrons, when light of suitable frequency impinges on the metal nanostructures, consequently enhancing the light absorption. The SPR distinctly dependent on the size, morphology, surrounding medium and the dielectric constant of NPs. The plasmonic excitation can follow a number of cascading relaxation paths such as radiative re-emission, non-radiative Landau damping or chemical interaction with the unoccupied orbitals of adsorbates. Mechanism of plasmonic catalysis can be understood by four possible ways. Some of the relevant explanations are summarized in this section to have a better understanding of the catalytic pathway during the course of reaction.[28] A schematic representation and energy diagram is illustrated in Figure 3 (A) and (B), respectively, to summarize the possible mechanistic pathways.

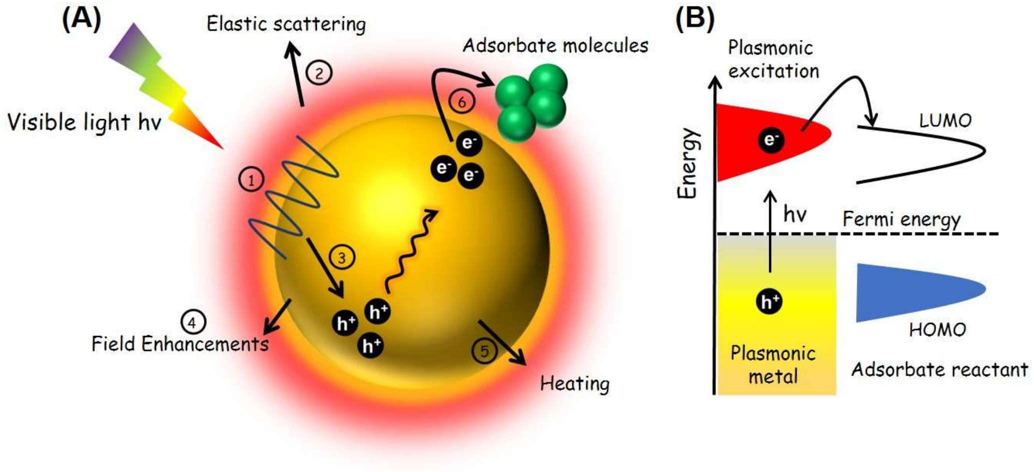

Figure 3. (A) Schematic representation of mechanistic pathways on metal NP upon visible light irradiation (1) surface plasmon (2) relaxation through scattering (3) creation of hot electron and holes (4) field enhancements (5) plasmonic heating and (6) transfer of hot electrons to the adsorbate molecules, (B) Energy diagram showing SPR on pure plasmonic metal NP and electron transfer to the LUMO of adsorbate/reactant molecules.

Generation of charge carriers

In this phenomenon, the energized charge carriers (i.e. electrons and holes) are generated on the surface of metal upon light irradiation. The probability to find the electron excited from the fermi E_f level after absorbing energy hν is E_f + hν. The electrons are transferred to the lowest unoccupied molecular orbitals (LUMO) of reactant molecules, hence forming transient negative ionic species. These species undergo chemical transformations leading to the formation of products via coupling of electronic and vibrational states of reactant and metal atoms. The overall mechanism is known as desorption induced by electronic transition (DIET).[48]

Hot electron transfer

After transferring the external energy in the form of light to the noble metal nanostructures, the excitation process leads to hot electron generation. Hot electrons are high energy species within the range of 1-3 eV and not exist in equilibrium with the metal, whereas the hot holes possess energy levels below the fermi level of metal nanostructures. These charge carriers undergo relaxation within the femtosecond timescales well before the occurrence of electron-phonon dissipations in picoseconds range. The origin of hot electrons in metals can be explained due to the differences in the heat capacities of electrons and lattice (phonons). Electrons get heated up much faster than the phonons in lattice due to electronic scattering within femtoseconds. Many experimental and theoretical studies show that the decay of surface plasmons leads to the generation of hot energy electrons in the noble metal nanostructures, with current efforts in realizing the mechanism of plasmonic excitation and hot electron generation.[49-51]

Plasmonic field enhancement

The plasmonic field enhancements of the electromagnetic dipole created due to electronic oscillations, can be usually studied and calculated by employing theoretical simulations like finite difference time domain (FDTD) or discrete dipole approximations (DDA). Depending on the morphology and size of NP, the effects arising from field enhancements can be gigantic. Usually the NPs with rods, prism or cubic morphology show enhancements by several orders specifically at the apex of the tips due to intense gradient of surface change densities.[52]

Heating

Another possible explanation of plasmonic enhancements is the temperature increment due to heat generation by energy dissipation within the NP. Mathematically, the total amount of heat power (P) absorbed by metal NP can be expressed by the following expression (8) under continuous illumination of light intensity (I) from its absorption cross section values (σ_{abs}).

$$P = I\ \sigma_{abs} \qquad (8)$$

The increase in temperature (δT) can also be calculated for simple spherical systems by relating power absorbed with the radius (R) of NP and thermal conductivity (k) of the medium in the following expression (9).

$$\delta T = P/(4\pi k R) \qquad (9)$$

This can be helpful in analyzing the heating effects for simple systems, however more detailed simulations are required in order to study complex systems of different morphologies.

Non-plasmonic effects

Apart from the plasmonic effects like optical field enhancements, hot electron transfers and plasmonic heating, the effects arising from non-plasmonic activity cannot be ignored while working out on the mechanism of the catalytic reaction. For example, enhancement in the catalytic activity can also be due to adsorption, reducing the activation energy barrier, creation of vacancies and defects. Photothermal effects arising due to heating also contributes to the kinetics of the reaction.[53]

Applications

The field of plasmonics has been explored with tremendous diversification in the recent past two decades. This development is well justified due to the rapid applications in various fields arising from their size and shape dependent properties. In this section, I will give a brief overview of myriad of potential applications shown by plasmonic NPs in different areas including medicine, SERS, identification and killing of cancerous cells, drug delivery and bio-sensing. As per the recent report from the Nature news in 2009, the history of plasmon-based applications was started by Martin Fleischmann at University of Southampton in the early 1970s. Later, Duyne *et al* studied the scattering effects enhanced by several orders of magnitude. It has developed an application as a device called surface-enhanced Raman spectroscopy (SERS) for its application in cancer therapy by selectively killing the cancerous cells. SERS is an electromagnetic field enhancement technique capable of detecting single molecules by plasmonic nanostructures. The levels of electric enhancements reach as high as 10^{10}-10^{11} accomplished by hot spots generation within the metal clusters. Zheng *et al.* reported Ag-Au alloy NPs for the reduction of 4-nitrothiophenol (4-NTP) and reaction kinetics and product detection were monitored by in situ real-time quantitative SERS spectroscopy. Another application in which the localized heat generated by plasmonic nanostructures is used to induce the death of cancerous cells, known as photothermal therapy. Wang and co-workers have synthesized various shapes of Au nanostructures (nanorods, nanocages and nanohexapods) with an LSPR absorption in the near infrared region (NIR) and have successfully demonstrated strong temperature increase and decreased tumor metabolism by 90% in mice.[54]

1.2 Purpose of this Thesis

Recently, much attention has been paid to the energy and environmental issues such as production of effluents, environmental pollution, huge consumption of fossil fuels, global warming and energy shortages. As a potential method to solve these problems, photocatalysis has attracted considerable attention. The design of highly efficient photocatalytic systems which help in the reduction of global atmospheric pollution and generation of alternate energy carrier is one of the most desirable yet challenging goals in the research of environmentally-friendly catalysts.

Harvesting abundant and renewable sunlight in energy production and environmental remediation is an emerging solution to the above stated problems. Recent research on solar-driven heterogeneous photocatalysis based on surface plasmon resonance has seen rapid growth and potentially opens a technologically promising avenue that can benefit the sustainable development of global energy and environment. This thesis was created with a purpose to develop synthetic protocols to synthesize mesoporous silica supported Ag-based plasmonic nanomaterials, including size and color controlled NPs, integration of Ag with catalytic active metals (Pd, Pt, Ru, Ni and Co) and broad spectrum photocatalyst synthesized by the combination of plasmonic Ag with single site Ti-oxide moiety. Mesoporous silica offered various advantages for designing metal NPs within the channels due to its tunable pore size, high surface area and connectivity of pores for easy diffusion of reactant molecules. In the entire thesis, three catalytic reactions have been explored and carried out in dark and under light irradiation conditions viz. hydrogen production from ammonia borane (NH_3BH_3, AB), nitrophenol reduction and Suzuki-Miyaura coupling reaction. I hope the visible light sensitive plasmonic materials designed in the present thesis can help in the understanding and design of more efficient systems to foster clean photocatalytic systems.

1.3 Outline of this Thesis

This Thesis contains eight chapters in total including first introduction and last general conclusion. Chapter I deals with the fundamentals of plasmonics, recent progress in the field of plasmonic catalysis and its applications. A general outline is shown in Figure 4, which shows the plasmonic catalysis of metal NP and the catalytic reactions explored under light irradiation conditions. The schematic illustration of catalytic systems prepared in the present thesis is shown in Figure 5.

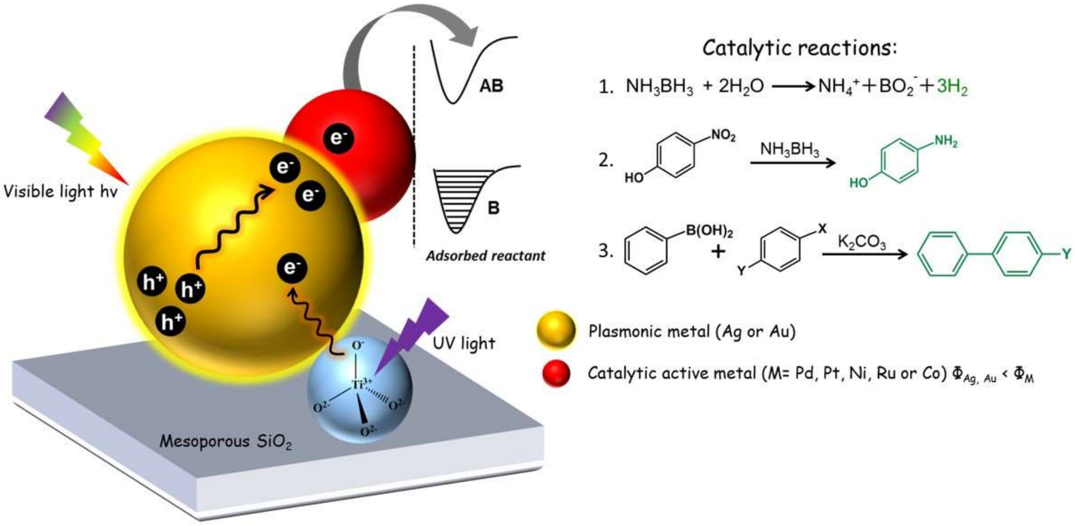

Figure 4. Schematic illustration of plasmonic catalysis by metal NPs supported on mesoporous silica.

Chapter II reports the synthesis of color-controlled spherical Ag NPs and nanorods, with features that originate from their particle sizes and morphologies, within the mesoporous structure of SBA-15 by the rapid and uniform microwave (MW)-assisted alcohol reduction method in the absence or presence of surface-modifying organic ligands. The obtained several Ag catalysts exhibit different catalytic activities in the H_2 production from ammonia borane under dark conditions, and higher catalytic activity is observed by smaller yellow Ag NPs in spherical form. The catalytic activities are specifically enhanced under the light irradiation for all Ag catalysts. In particular, under light irradiation, the blue Ag nanorod shows a maximum enhancement of more than twice that observed in the dark. It should be noted that the order of increasing catalytic performance is in close agreement with the order of absorption intensity owing to the Ag LSPR at irradiation light wavelength. Upon consideration of infrared thermal effect, wavelength dependence on catalytic activity, and effect of radical scavengers, it can be concluded that the dehydrogenation of AB is promoted by change of charge density of the Ag NP surface derived from LSPR. The LSPR-enhanced catalytic activity can be further realized in the tandem reaction consisting of dehydrogenation of AB and hydrogenation of 4-nitrophenol, in which a similar tendency in the enhancement of catalytic activity is observed.

Chapter III describes the synthesis and characterization of uniformly dispersed Pd/Ag bimetallic system supported on mesoporous silica SBA-15, synthesized by a two-step method. Ag/SBA-15 was first synthesized by the microwave-assisted alcohol reduction method, which afforded color-controlled Ag NPs with different particle sizes and morphologies. Further decoration of Ag/SBA-15 with Pd NPs was achieved via LSPR-assisted deposition under visible light irradiation. All Pd/Ag/SBA-15 catalysts showed higher catalytic activities than the inherent Ag/SBA-15 catalysts under both dark and visible-light irradiation conditions, where the Pd/Ag/SBA-15 originated from blue Ag nanorods afforded a maximum enhancement effect. The order of increasing catalytic activity was found to be in accordance with the Ag-LSPR absorption intensity. The LSPR-enhanced photocatalytic activity of the Pd/Ag/SBA-15 was also demonstrated in the Pd-driven Suzuki–Miyaura coupling reaction of aryl halides with boronic acids, where a similar trend in the enhancement of catalytic activity was observed under visible light irradiation.

In Chapter IV, visible light responsive bimetallic Pt/Ag nanocatalyst supported on mesoporous silica was successfully prepared by a two-step method viz. MW assisted alcohol reduction, followed by Pt deposition by the assistance of LSPR effect of Ag NPs. The performance of prepared catalysts was explored in the hydrogen (H_2) production from ammonia borane. A great enhancement for Pt(0.25)/Ag/SBA-15 (0.25 wt % of Pt on 1.0 wt % of Ag) was observed by a factor of 2.8, which is highest among our previously reported results of spherical bimetallic NPs. A plausible photocatalytic and charge separation mechanism has been proposed to envisage the tentative reaction pathway.

Chapter V describes the study of series of bimetallic M/Ag (where M represents Pd, Ru, Ni and Co metallic species) nanorod (NR)-based plasmonic photocatalysts with 0.5 wt % loading of M on Ag (1.0 wt %) synthesized within the mesoporous channels of SBA-15. The photocatalytic activity is assessed by hydrogen production from ammonia borane (AB) and chemical reduction of 4-nitrophenol (NP) to 4-aminophenol (AP) under visible light irradiation. The enhanced catalytic activities under light irradiation in comparison with dark conditions are explained by a plausible photocatalytic and charge separation mechanism to envisage the tentative reaction pathway. The reusability of the catalyst is evaluated up to four consecutive catalytic runs.

In Chapter VI, a systematic comparison of plasmonic properties and catalytic performances has been conducted with Pd deposited bimetallic nanostructures of plasmonic Ag and Au. Mesoporous silica (SBA-15) supported Ag and Au NPs were synthesized using a microwave assisted alcohol reduction system. 1-hexanol and ethylene glycol were employed as reducing agents for Ag and Au precursors, respectively, depending on their reduction ability to obtain metallic NPs. Further decoration with Pd NPs was achieved via localized surface plasmon resonance (LSPR)-assisted deposition under visible light irradiation. The obtained Pd/Au and Pd/Ag NPs exhibited specific photocatalytic activity in the Suzuki coupling reaction and hydrogen production from ammonia borane (AB), respectively.

The Chapter VII deals with Ag-based plasmonic catalyst supported on mesoporous silica with isolated and tetrahedrally coordinated single-site Ti-oxide moieties, namely, Ag/Ti-SBA-15, with the purpose of utilizing the broad spectral range of solar energy. The Ti-SBA-15 support allows the deposition of small Ag NPs with a narrow size distribution. The catalytic activity of Ag/Ti-SBA-15 in hydrogen production from ammonia borane by hydrolysis was significantly enhanced in comparison with Ag/SBA-15 without Ti-oxide moieties and Ag/TiO_2/SBA-15 involving agglomerated TiO_2, both in the dark and under light irradiation. Improved electron transfers under light irradiation caused by the creation of heterojunctions between Ag NPs and Ti oxide moieties explain the results obtained in the present study.

Finally, the overall conclusions are presented in Chapter VIII.

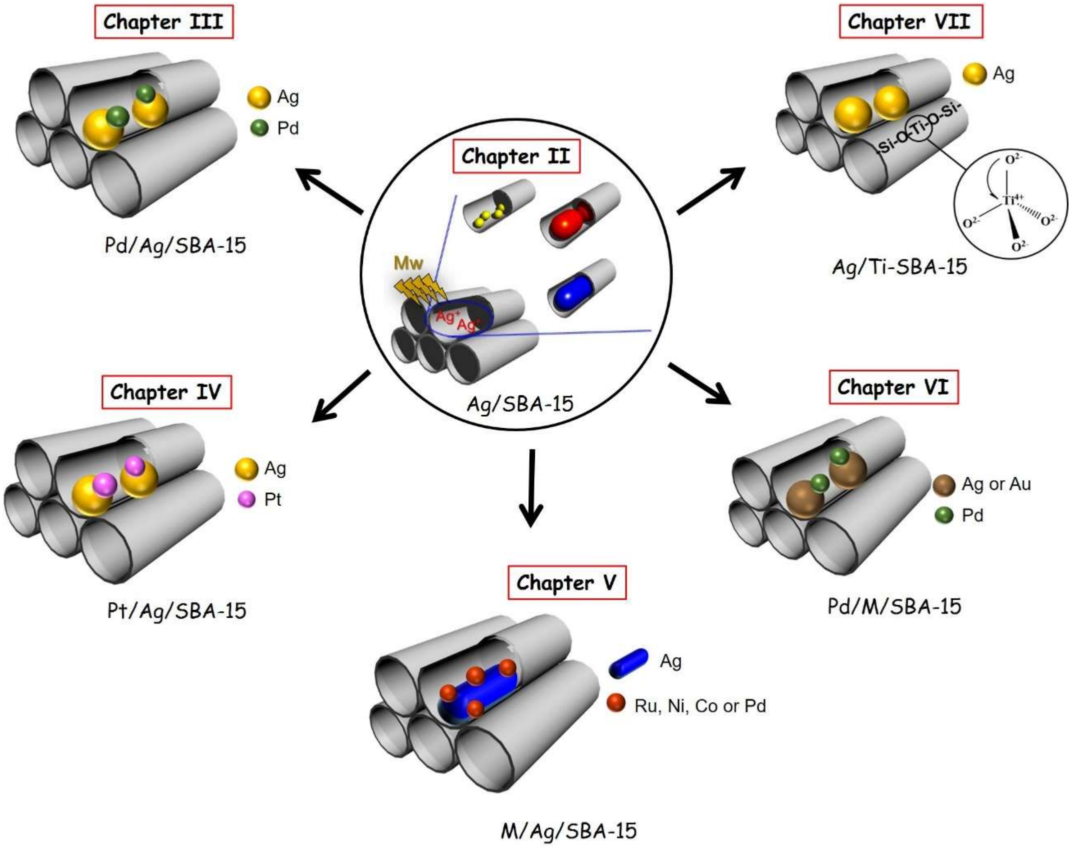

Figure 5. Schematic outline of catalytic systems prepared in the present thesis.

1.4 References

[1] F. P. Perera, *Environ. Health Perspect.,* 2017, **125**, 141.

[2] D. M. Schultz and T. P. Yoon, *Science*, 2014, **343**, 985.

[3] X. Lang, X. Chen and J. Zhao, *Chem. Soc. Rev.*, 2014, **43**, 473.

[4] J. Luo, J-H Im, M.T. Mayer, M. Schreier, M. K. Nazeeruddin, N-G Park, S. D. Tilley, H. J. Fan and M. Grätzel, *Science*, 2014, **345**, 1593.

[5] J. Schneideer, M. Matsuoka, M. Takeuchi, J. Zhang, Y. Horiuchi, M. Anpo and D. W. Bahnemann, *Chem. Rev.*, 2014, **114**, 9919.

[6] Q. Xiang, B. Cheng and J. Yu, *Angew. Chem. Int. Ed.*, 2015, **54**, 11350.

[7] César Clavero, *Nat. Photonics*, 2014, **8**, 95.

[8] X. Liu, J. Locozzia, Y. Wang, X. Cui, Y. Chen, S. Zhao, Z. Li and Z. Lin, *Energy Environ. Sci.*, 2017, **10**, 402.

[9] T. Hisatomi, J. Kubota and K. Domen, *Chem. Soc. Rev.*, 2014, **43**, 7520.

[10] W. Tu, Y. Zhou and Z. Zou, *Adv. Mater.*, 2014, **26**, 4607.

[11] B. Han, W. Wei, L. Chang, P. Cheng and Y. H. Hu, *ACS Catal.*, 2016, **6**, 494.

[12] Günther Knör, *Coord. Chem. Rev.*, 2015, **304**, 102.

[13] D. Pathania, M. Kumari and V. K. Gupta, *Mater. Des.*, 2015, **87**, 1056.

[14] S. Dong, J. Feng, M. Fan, Y. Pi, L. Hu, X. Han, M. Liu, J. Sun and J. Sun, *RSC Adv.*, 2015, **5**, 14610.

[15] C-C. Wang, J-R. Li, X-L. Lv, Y-Q. Zhang and G. Guo, *Energy Environ. Sci.*, 2014, **7**, 2831.

[16] A. Fujishima and K. Honda, *Nature*, 1972, **238**, 37.

[17] A. L. Linsebigler, G. Lu and J. T. Yates, *Chem. Rev.*, 1995, **95**, 735.

[18] X. Zhou, G. Liu, J. Yu and W. Fan, *J. Mater. Chem.*, 2012, **22**, 21337.

[19] X. Zhang, Y. L. Chen, R-S. Liu and D. P. Tsai, *Rep. Prog. Phys.*, 2013, **76**, 46401.

[20] W. Hou and S. B. Cronin, *Adv. Funct. Mater.*, 2013, **23**, 1612.

[21] A. Naldoni, F. Riboni, U. Guler, A. Boltasseva, V. M. Shalaev and A. V. Kildishev, *Nanophotonics*, 2016, **5**, 112.

[22] J. A. Schuller, E. S. Barnard, W. Cai, Y. C. Jun, J. S. White and M. L. Brongersma, *Nat. Mater.*, 2010, **9**, 193.

[23] E. Hutter and J. H. Fendler, *Adv. Mater.*, 2004, **16**, 1685.

[24] I. Freestone, N. Meeks, M. Sax and C. Higgitt, *Gold Bull.*, 2007, **40**, 270.

[25] A. Moores and P. Le Floch, *Biosensing Using Nanomater.*, 2009, **137**. (Book chapter)

[26] D. Maystre, *Plasmonics*, 2012, **167**. (Book chapter)

[27] S. A. Maier, *Plasmonics : Fundamentals and Applications*, 2004, **677**. (Book)

[28] S. Linic, U. Aslam, C. Boerigter and M. Morabito, *Nat. Mater.*, 2015, **14**, 567.

[29] S. Mukherjee, L. Zhou, A. M. Goodman, N. Large, C. Ayala, Y. Zhang, P. Nordlander and N J Halas, *J. Am. Chem. Soc.*, 2014, **136**, 64.

[30] C. Wen, A. Yin and W. L. Dai, *Appl. Catal. B*, 2014, **160**, 730.

[31] P. Verma, Y. Kuwahara, K. Mori and H. Yamashita, *J. Mater. Chem. A*, 2016, **4**, 10142.

[32] C. Chen, M. Chen, C. K. Chen, P. C. Wu, P. T. Chen, M. Basu, S. F. Hu, D. Tsai and R. S. Liu, *Chem Commun.*, 2015, **51**, 549.

[33] T. Jiang, C. Jia, L. Zhang, S. He, Y. Sang, H. Li, Y. Li, X. Xu and H. Liu, *Nanoscale*,

2015, **7**, 209.

[34] X. Chen, H. Y. Zhu, J. C. Zhao, Z. F. Zheng and X. P. Gao, *Angew. Chem., Int. Ed.*, 2008, **47**, 5353.

[35] H. Zhu, H. Zhu, X. Chen, Z. Zheng, X. Ke, E. Jaatinen, J. Zhao, C. Guo, T. Xie and D. Wang, *Chem. Commun.*, 2009, 7524.

[36] L. Gomez, J. L. Hueso, M. C. Ortega-Liebana, J. Santamaria and S. B. Cronin, *Catal. Commun.*, 2014, **56**, 115.

[37] L. Gomez, V. Sebastian, M. Arruebo, J. Santamaria and S. B. Cronin, Phys. *Chem. Chem. Phys.*, 2014, **16**, 15111.

[38] X. Chen, Z. Zheng, X. Ke, E. Jaatinen, T. Xie, D. Wang, C. Guo, J. Zhao and H. Zhu, *Green Chem.*, 2010, **12**, 414.

[39] K. H. Chen, Y. C. Pu, K. D. Chang, Y. F. Liang, C. M. Liu, J. W. Yeh, H. C. Shih and Y. J. Hsu, *J. Phys. Chem. C*, 2012, **116**, 19039.

[40] F. Wang, C. Li, H. Chen, R. Jiang, L. Sun, Q. Li, J. Wang, J. Yu and C. Yan, *J. Am. Chem. Soc.*, 2013, **135**, 5588.

[41] X. Huang, Y. Li, Y. Chen, H. Zhou, X. Duan and Y. Huang, *Angew. Chem. Int. Ed.*, 2013, **125**, 6179.

[42] Y. Sugano, Y. Shiraishi, D. Tsukamoto, S. Ichikawa, S. Tanaka and T. Hirai, *Angew. Chem. Int. Ed.*, 2013, **125**, 5403.

[43] Q. Xiao, S. Sarina, A. Bo, J. Jia, H. Liu, D. Arnold, Y. Huang, H. Wu and H. Zhu, *ACS Catal.*, 2014, **4**, 1725.

[44] Q. Xiao, S. Sarina, E. Jaatinen, J. Jia, D. Arnold, H. Liu and H. Zhu, *Green Chem.*, 2014, **16**, 4272.

[45] H. Zhu, X. Ke, X. Yang, S. Sarina, and H. Liu, *Angew. Chem. Int. Ed.*, 2010, **122**, 9851.

[46] K. Fuku, R. Hayashi, S. Takakura, T. Kamegawa, K. Mori and H. Yamashita, *Angew. Chem. Int. Ed.*, 2013, **52**, 7446.

[47] Y. Zhang, Q. Xiao, Y. Bao, Y. Zhang, S. Bottle, S. Sarina, B. Zhaorigetu and H. Zhu, *J. Phys. Chem. C*, 2014, **118**, 19062.

[48] M. L. Brongersma, N. J. Halas and P. Nordlander, *Nat. Nanotechnol.*, 2015, **10**, 25.

[49] M. Sun and H. Xu, *Small*, 2012, **8**, 2777.

[50] S. M. Kim, S. W. Lee, S. Y. Moon and J. Y. Park, *J. Phys. Condens. Matter*, 2016, **28**,

254002.

[51] D. Tsukamoto, Y. Shiraishi, Y. Sugano, S. Ichikawa, S. Tanaka and T. Hirai, *J. Am. Chem. Soc.*, 2012, **134**, 6309.

[52] S. Linic, U. Aslam, C. Boerigter and M. Morabito, *Nat. Mater.*, 2015, **14**, 744.

[53] G. Baffou and R. Quidant, *Chem. Soc. Rev.*, 2014, **43**, 3898.

[54] Y. Wang, K. C. Black, H. Luehmann, W. Li, Y. Zhang, X. Cai, D. Wan, S. Y. Liu, M. Li, P. Kim, Z. Y. Li, L. V. Wang, Y. Liu and Y. Xia, *ACS Nano*, 2013, **7**, 2068.

Chapter II

Color-Controlled Ag Nanoparticles and Nanorods within Confined Mesopores: Microwave-Assisted Rapid Synthesis and Application in Plasmonic Catalysis under Visible-Light Irradiation

2.1 Introduction

Plasmonic metal nanoparticles (NPs), such as Au, Ag and Cu, have attracted considerable attentions as fascinating photo-responsive materials that can strongly absorb visible and infrared light owing to their localized surface plasmon resonance (LSPR).[1-3] LSPR is described as the collective oscillations of free conduction electrons confined in metal NPs stimulated by the incident light.[4,5] Consequently, the local electromagnetic field in the vicinity of the plasmonic metal NPs is dramatically enhanced, which led to an array of applications in as diverse as surface-enhanced Raman spectroscopy (SERS),[6-8] single-molecule spectroscopy,[9,10] solar cells[11] and biological molecular detection/sensing. The LSPR wavelength and intensity of metallic nanostructures are dependent on the nature of metals, their sizes, or morphologies.[12-14] For example, spherical Ag (38 nm in mean diameter), Au (25 nm) and Cu (133 nm) NPs exhibit LSPR absorption peaks at approximately 420, 520, and 610 nm, respectively,[12] which are attractive for efficient solar light utilization. The increase in size shifts the LSPR wavelength of metal NPs to longer wavelength. The change of morphologies from spheres into wires or cubes alters the LSPR wavelengths of Ag nanostructures, and also increases the number of LSPR peaks because the geometrical symmetry of metallic nanostructures determines their polarization modes.[12] More interestingly, the color of plasmonic NPs can be tuned owing to changes in the LSPR absorption wavelength arising from size- and morphology-control.[15,16]

Such unique characteristic has given rise to a new approach to construct plasmonic metal NPs/semiconductor hybrids, known as plasmonic photocatalysts, to sensitize semiconductors and boost their photocatalytic abilities.[17,18] In the case of Au/TiO_2, the hot electrons from the excited plasmonic Au NPs with energies above the Schottky barrier (~1.0 eV) will be injected into the neighboring TiO_2 conduction band, leading to direct charge separation on the plasmonic NPs. In such a way, interfacial charge transfer can be realized between plasmonic Au metals and semiconductor supports, which further drive chemical reaction.

Plasmonic metal NPs behave not only as the visible light absorber, but also as the catalytically active species that induce the photocatalysis directly.[19] The surface charge density of plasmonic metal NPs is partially localized, and this is increased by charge separation derived from the LSPR effect in the absence of a semiconductor to act as an electron acceptor.[4] Therefore, the free-standing plasmonic metal NPs without supports could be a convincing system to understand their intrinsic catalytic property and rule out the support-effect.[20] Despite the fact that free-standing plasmonic metal NPs exhibit significant photocatalytic activity in organic transformations under visible light irradiation, they are vulnerable to aggregation, and suffer from the low stability. Therefore, plasmonic metal catalysts are sometimes supported on the insulating oxides with band gaps over 5 eV,[21] such as ZrO_2 (~5.8 eV), SiO_2 (~9.0 eV) and Al_2O_3 (~8.7 eV). It is also difficult for the inert insulators to capture the hot electrons induced by the plasmonic metal NPs because of their large potential barrier.[22,23] which exclude the participation of inert insulators in photocatalytic reactions. Triggered by their unexpected plasmonic catalytic properties, supported Au and Ag NPs on inert insulators have been studied in several catalytic reactions, such as the complete decomposition of the volatile organic compounds, selective oxidation reaction, and the synthesis of complicated pharmaceutical molecules.[19,24-27] However, the systematic investigation of plasmonic photocatalysis using size- or morphology-controlled meal NPs have not been pursued so far. In this chapter, I have performed systematic examination of plasmonic catalysis using Ag NPs having different colors based on size- and morphology-control. A new protocol has been developed for the synthesis of plasmonic Ag NPs with different colors by combining a microwave (Mw) heating process and the confined pore structure of SBA-15 mesoporous silica material. It is demonstrated that the localized surface charge of Ag NPs unambiguously enhances catalytic activity under visible light irradiation by the assist of LSPR. It is also expected and herein verified that the enhancement effect was significantly dependent on the Ag NPs used. The development of plasmonic metal NP catalysts with optimum color based on the precise size- and morphology-control enables maximum enhancement under various light environments.

2.2 Experimental

2.2.1 Materials

Tetraethoxysilane (TEOS), hydrochloric acid, 1-hexanol, acetone, silver nitrate and sodium laurate (Lau) were purchased from Nacalai Tesque Inc. Triblock copolymer

P123 and ammonia borane (NH_3BH_3) were purchased from Sigma-Aldrich Co. All chemicals were used as received without further purification.

2.2.2 Preparation of Ag nanoparticles on SBA-15 mesoporous silica

SBA-15 was prepared according to a previous report by the sol-gel method using TEOS as a silica source and triblock copolymer P123 as a template.[28] Typically, a 1-hexanol suspension of SBA-15 powder (0.396 g), an aqueous solution of $AgNO_3$ (0.037 mmol) and Lau (10 mg) as surface-modifying ligand for Ag were irradiated by microwave (500 W, 2.45 GHz) under an Ar atmosphere. After filtration and washing with acetone and distilled water, the resulting powder was dried at 70° C overnight under air. Size control of Ag was achieved by varying the Mw irradiation time (3 or 5 min) and with or without ligands, resulting in the formation of 1 wt % Ag catalysts **1-6** (Table 1).

2.2.3 Characterization

BET surface area measurements were performed using a BEL-SORP max (Bel Japan, Inc.) at -196° C. The samples were degassed in vacuum at 70° C for 24 h prior to analysis. UV-vis diffuse reflectance spectra of powdered samples were collected using a Shimadzu UV-2450 spectrophotometer. The reference was $BaSO_4$, and the absorption spectra were obtained by using the Kubelka-Munk function. Inductively coupled plasma optical emission spectrometry (ICP-OES) measurements were performed using a Nippon Jarrell-Ash ICAP-575 Mark II. The transmission electron microscopy (TEM) images were obtained with a Hitachi Hf-2000 FE-TEM equipped with a Kevex energy-dispersive X-ray detector operated at 200kV. Ag K-edge X-ray absorption fine structure (XAFS) was recorded using a fluorescence-yield collection technique at the beam line 01B1 station with an attached Si (111) monochromator at SPring-8, JASRI, Harima, Japan (prop. No. 2014A1045).

2.2.4 H_2 production from NH_3BH_3

H_2 production from NH_3BH_3 was carried out in an aqueous suspension of various Ag catalyst. The Ag catalyst powder (20 mg) was suspended in distilled water (5 mL) in a test tube. After bubbling of the mixture with Ar, NH_3BH_3 (20 μmol) was injected into the mixture through a rubber septum. The test tube was photoirradiated by a 500 W Xe lamp through a glass filter ($\lambda > 420$ nm), monochromatic light ($\lambda = 400$, 440, 460 and 480 nm) through a band-pass filter, or red LED lamp ($\lambda_{max} = 650$ nm) with magnetic stirring at room temperature (25°C). The amount of H_2 in the gas phase was measured using a Shimadzu GC-8A gas chromatograph equipped with a MS-5A column.

2.2.5 Reduction of 4-nitrophenol by NH_3BH_3

An aqueous solution of 4-NP (45 mM) and AB (90 mM) was freshly prepared, respectively. The Ag catalyst powder (10 mg) and 40 μL of 4-NP solution was added in distilled water (5 mL) in a test tube. After bubbling of the mixture with Ar, 3mL of AB solution was injected into the mixture through a rubber septum with magnetic stirring at room temperature (25°C). The intensity of the absorption peak at 400 nm for 4-NP was recorded on the UV-vis spectroscopy at different time interval.

2.3 Results and discussion

Catalyst Preparation and Characterization

SBA-15 mesoporous silica with a regular one-dimensional and hexagonally ordered pore structure was prepared according to a previously reported procedure via the surfactant self-assembly approach.[28] Low-angle XRD measurement exhibited two peaks at around 1.0–2.0°, corresponding to a hexagonal structure. The N_2 adsorption-desorption measurement showed a high specific surface area (632 $m^2\ g^{-1}$), large mesoporous structure (8.2 nm) and pore volume (1.18 $cm^3\ g^{-1}$).

MW dielectric induction heating has attracted extensive attention as a potential preparation method for monodispersed metal NPs because energy-efficient MW irradiation allows internal, rapid, and uniform heating.[29-31] In order to perform the systematic investigation of plasmonic catalysis using size- and morphology-controlled Ag NPs, several types of Ag NP were prepared within the confined mesopore of SBA-15 by MW-assisted alcohol reduction with varying irradiation time (3 or 5 min) and in the absence or presence of surface-modifying organic ligands (sodium laurate (Lau; $CH_3(CH_2)_{10}COONa$) or sodium stearate (Str; $CH_3(CH_2)_{16}COONa$)). Typically, a 1-hexanol suspension of SBA-15 powder, an aqueous solution of $AgNO_3$ and Lau was irradiated by Mw (500 W, 2.45 GHz) under an Ar atmosphere for 3 min, affording Ag catalyst **1** (Ag: 1 wt%). The sets of synthetic conditions and the denoted names of the obtained Ag catalysts are summarized in Table 1. I selected 1-hexanol as a solvent because of its low water solubility, appropriate dielectric loss factor at 2.45 GHz, and high boiling point (157° C).[32]

Table 1. Characteristics of the Ag/SBA-15 catalysts prepared by the MW-assisted method.

Ag catalyst	**ligand**	**Irradiation time (min)**	**Average size of Ag NP (nm)**	**Sample color**
1	sodium laurate (Lau) $CH_3(CH_2)_{10}COONa$	3	$d = 3.9$	light green-yellow
2		5	$d = 4.8$	light green-yellow
3	sodium stearate (Str) $CH_3(CH_2)_{16}COONa$	3	$d = 5.9$	yellow- bright orange
4		5	$d = 6.6$	yellow- bright orange
5	–	3	13 (*l*) × 8.2 (*w*) (aspect ratio = 2.8)	red
6		5	48 (*l*) × 7.9 (*w*) (aspect ratio = 6.1)	blue

The N_2 adsorption-desorption measurement showed high BET surface areas and pore volumes even after deposition of the Ag. The diffraction peaks due to the hexagonally packed mesoporous structure were almost at the same locations after deposition, suggesting that the long-range order was retained. The TEM images of the Ag catalysts are shown in Figure 1. Nanosized Ag particles were successfully deposited within the well-ordered mesoporous channel structure of SBA-15. Spherical Ag NPs with a mean diameter of 3.9 nm and a narrow size distribution were observed in the case of Ag catalyst **1**, which was subjected to MW irradiation for 3 min in the presence of Lau. The increase of irradiation time to 5 min (Ag catalyst **2**) slightly increased average diameter of Ag NPs without significant changes in their color and morphology. Similar tendency was observed in the presence of Str as a surface-modifying organic ligands (Ag catalyst **3** and **4**), but the average diameter of Ag NPs slightly increased compared with those obtained in the presence of Lau. This is probably because the permeation of Str with longer alkyl-chain into the mesoporous channel is limited, which allows the agglomeration of Ag NPs.

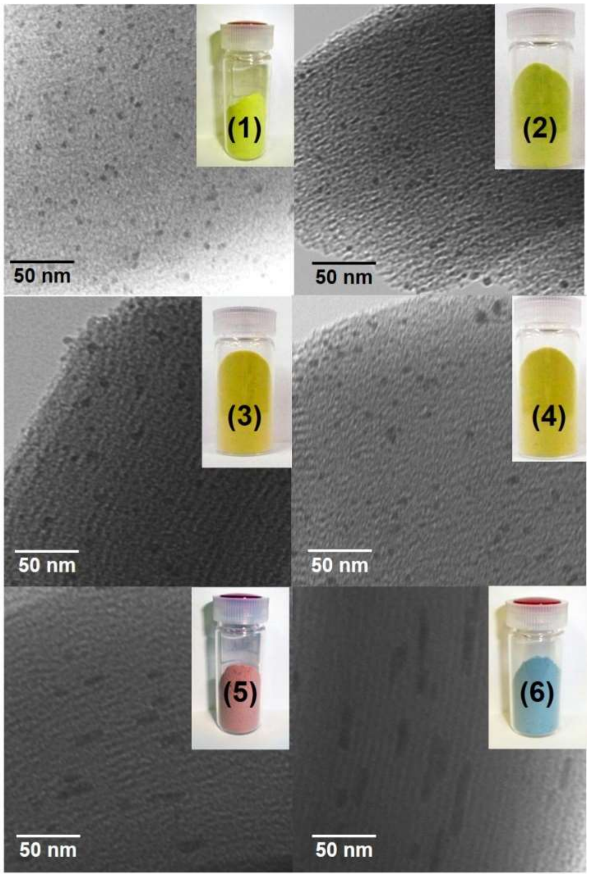

Figure 1. TEM images and sample photographs (inset) of Ag catalysts 1-6.

On the contrary, in the case of Ag catalyst **5** and **6**, which were prepared in the absence of surface-modifying ligands, Ag nanorods were observed parallel to the SBA-15 mesopores. The aspect ratio of the Ag nanorods increased markedly with increasing Mw irradiation time from 3 to 5 min. The average size that is perpendicular to these Ag nanorods was ca. 8 nm, which was in close agreement with the pore size of SBA-15. In the preliminary experiment, further increases of the Mw irradiation time do not change the final rod size and sample color.

It is interesting to investigate the optical properties of the obtained Ag catalysts since these samples possess characteristic colors due to the LSPR of Ag nanostructures; Ag catalyst **1** and **2** (light green-yellow), **3** and **4** (yellow- bright orange), **5** (red), and **6** (blue), as summarized in Table 1. The intensity and wavelength of LSPR absorption depended on the size, morphology, and aspect ratio of the Ag nanostructures which reflects the UV-vis spectra (Figure 2). No absorption is observed from the ultraviolet to visible region in the original SBA-15. Ag catalysts **1-4** exhibited intense absorption band at around 410 nm owing to the LSPR absorption of spherical Ag NPs. Slight red shift of the LSPR absorption was observed in the case of Ag catalyst **3** and **4**, which were prepared in the presence of Str, accompanied with the decrease of intensity indicates the increase of Ag NPs size. In contrast, Ag catalysts **5** and **6** exhibit two absorption peaks in the visible and infrared regions corresponding to the transverse mode perpendicular to the Ag nanorods and longitudinal mode along the long axis of the Ag nanorods, respectively.[33] More significant longitudinal surface plasmon resonances were observed in the Ag catalyst **6** at around 1200 nm, which clearly suggests the increase of mean aspect ratio of Ag nanorods.

In the entire thesis, for the study of optical properties of plasmonic catalysts by UV-vis spectra, a theoretical function called as Kubelka Munk (KM) function is used. It is a widely used theoretical model of reflectance which supposes that some light passing through a homogeneous sample is scattered and absorbed so that the light is attenuated in both directions. The Kubelka-Munk (KM) model has a particularly simple solution in the case of semi-infinite samples. All the geometric peculiarities of the inhomogeneous sample are condensed into a single parameter, the scattering coefficients. The diffuse reflectance R_∞ is defined as:

$$R_\infty = 1 + \frac{k}{s} - \sqrt{\frac{k}{s}\left(2 + \frac{k}{s}\right)}$$

Where k represents absorption coefficient for the sample, k = $4\pi{}^{k}/_{\lambda}$; where λ is the wavelength. The simple and more familiar KM expression can be represented as;

$$\frac{k}{s} = \frac{(1 - R_\infty)^2}{2R_\infty}$$

This KM function used as y-axis in all the UV-vis spectra is approximately proportional to the absorption coefficient of the sample.

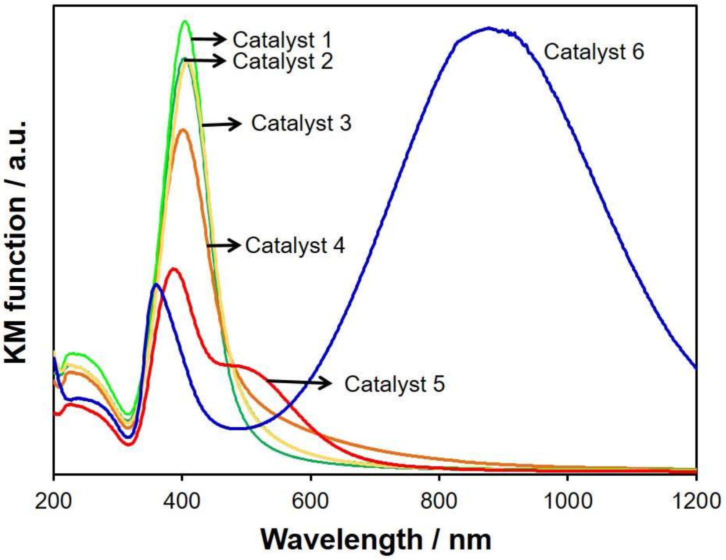

Figure 2. UV-Vis spectra of Ag catalysts 1-6.

Plasmonic catalysis in H_2 production from ammonia borane

In an effort to investigate the potential catalytic activities of the color-controlled Ag NPs, I first conducted H_2 production from NH_3-BH_3 as a valuable model reaction. Efficient and convenient storage of hydrogen is one of the key issues to realize the future hydrogen economy.[34] AB has attracted much research interest as a leading molecular candidate for hydrogen storage materials because of its low molecular weight (30.87 $g \cdot mol^{-1}$), high theoretical hydrogen gravimetric capacity (19.6 wt %), and high stability in solid form at room temperature. The stored hydrogen in AB can be released *via* hydrolysis routes, in which H_2 is stoichiometrically produced in a 3/1 (H_2/AB) molar ratio according to Equation (1).[35-37] Noble metal catalysts with superior catalytic activity under mild conditions are particularly desirable as they are expected to have widespread application.

$$NH_3BH_3 + 2H_2O \rightarrow NH_4^+ + BO_2^- + 3H_2 \qquad (1)$$

All Ag catalysts exhibited H_2 production activity from aqueous AB under an Ar atmosphere at room temperature (25°C) in the dark conditions (Figure 3A). Induction period was not observed, and H_2 was stoichiometrically produced in a 3:1 (H_2/NH_3BH_3) molar ratio during the course of the reaction for all samples, indicating the occurrence of complete dehydrogenation. No catalytic activity was observed in the blank test (without catalyst). The catalytic activity depends on the particle size of Ag NPs: the smallest Ag catalyst **1** with yellow color was the most active among investigated, in which H_2 production reaction was completed within a short reaction time. The catalytic activity decreased in the order of Ag catalyst **1** > **2** > **3** > **4** > **5** > **6**. This order corresponds with the increase of Ag NP size. These results suggest that catalytic H_2 production from AB in dark conditions occurred on the exposed surface Ag atoms of the NPs, in accordance with the fact that the smaller Ag NPs possess the larger number of surface atoms as well as more low-coordinated metal sites *i.e.* vertices and edges.

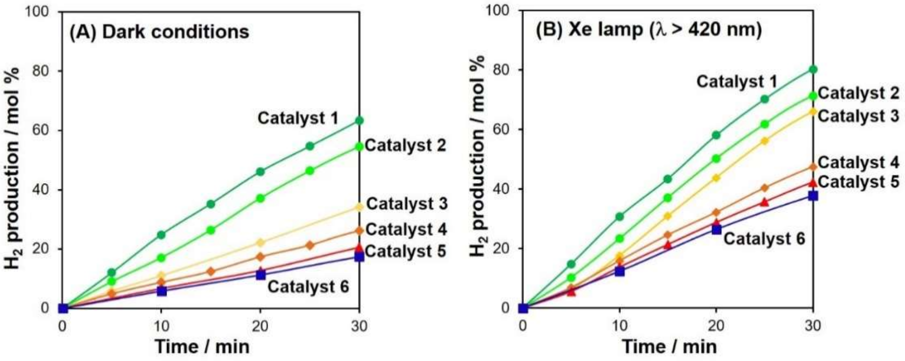

Figure 3. Time course of H_2 production from ammonia borane in the presence of Ag catalysts under dark (A) and light irradiation conditions (B).

In order to attain maximum efficiency of the Ag catalysts, the effect of Ag-LSPR on H_2 production activity was investigated under light irradiation ($\lambda > 420$ nm, 320 mW cm^{-2}) using Xe lamp. It is notable that the catalytic performances of all Ag NPs were enhanced under light irradiation (Figure 3B). Interestingly, the rate of increase in catalytic activity was significantly dependent on the color of the Ag catalysts, and increased in the following order: **1** (1.24) < **2** (1.25) < **3** (1.60) < **4** (1.89) < **5** (2.12) < **6** (2.48), as summarized in Figure 4 (the values in parenthesis are the rate of increase). This tendency matched well with the Ag-LSPR absorption intensity at wavelengths of more than 420 nm. The on/off effect of this light irradiation was also confirmed using the Ag catalyst **6**. In comparison with the reaction under dark conditions (light off), the catalytic activity was significantly enhanced by light irradiation with quick response (light on) (Figure 5A). It should be noted that the slope of activity after light irradiation (15 min) was almost the same as that of activity under light irradiation from 0 min.

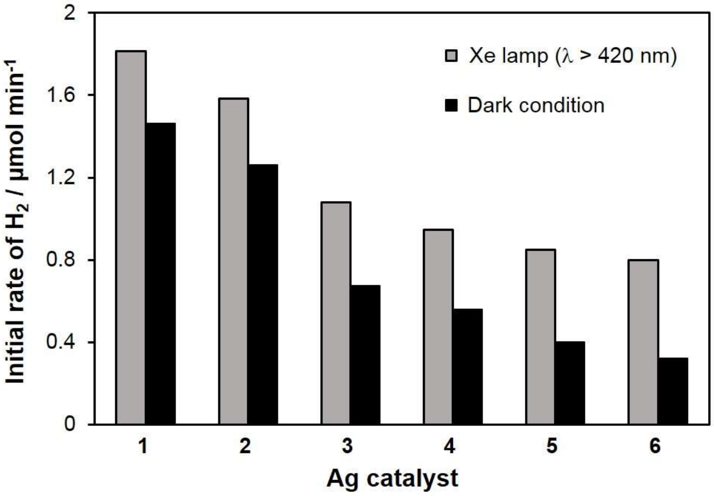

Figure 4. Comparison of initial H_2 production rate from AB in the presence of Ag catalysts under dark and light irradiation conditions.

Because light irradiation using a Xe lamp at λ > 420 nm contains not only visible light but also infrared light, it is suspected that the above enhancement of catalytic activity under light irradiation is simply originated from the thermal effect by the infrared light. In fact, it was confirmed that the temperature of the reaction solution using Ag catalyst **6** slightly increased (about 5°C) under light irradiation, because the Ag nanorods especially show wide LSPR absorption over the infrared region owing to the longitudinal mode along the long axis of the rods. In order to rule out the thermal effect of infrared light, the thermal reaction at 30°C was conducted under dark conditions using Ag catalyst **6**. The initial H_2 production activity under dark conditions at 30°C was 0.46 µmol min^{-1}, which was slightly higher than 0.32 µmol min^{-1} under dark conditions at room temperature (25°C), but was significantly lower than 0.80 µmol min^{-1} under light irradiation (Figure 5B). The rate of enhancement of catalytic performance depended significantly on the colors of Ag catalysts and increased in the order Ag catalyst **1** < **4** < **6**, which is same tendency that observed under Xe lamp irradiation.

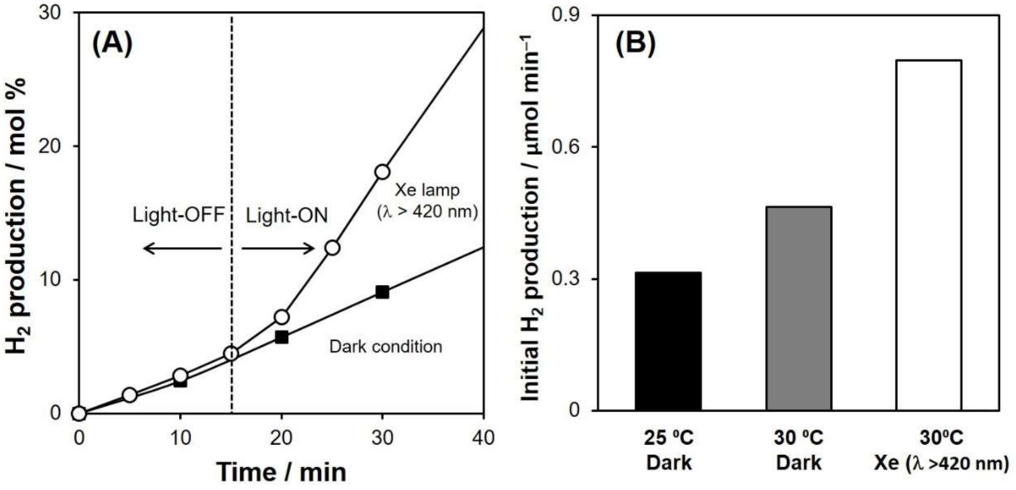

Figure 5. Effect of light irradiation and temperature. (A) On/Off effect on the dehydrogenation of AB in the presence of Ag catalyst 6. (B) Initial H_2 production rate under dark and light irradiation conditions.

Moreover, the plasmonic heating effect of Ag NPs derived from plasma oscillation by LSPR, as previously reported by Christopher et al., can be calculated as shown in Equation (2).[38]

$$T = T_\infty + \frac{I_0 K_{abs} r_0}{6k_\infty} \qquad (2)$$

This equation can be employed as a function of light intensity (I_0), absorption efficiency (K_{abs}), the diameter of metallic NP (r_0), the thermal conductivity of the surrounding medium (k_∞) and heating temperature (T_∞). By adopting the experimental values I_0 = 320 mW cm^{-2}, r_0 = 4–50 nm, T_∞ = 298 K, and the values calculated by Christopher *et al.* (K_{abs}= 3, k_∞= 40 mW m^{-1} K^{-1}), the increase in temperature owing to the plasmonic heating effect in the present catalytic system was determined to be less than 0.002 K. Upon consideration of the above results, it can be concluded that the enhanced catalytic performance originated largely from the Ag-LSPR effect under irradiation, and the contribution of the thermal effect was negligible.

Figure 6 summarized the relationship between the increasing rates of catalytic performance per light intensities and Kubelka-Munk (KM) function intensity derived from Ag-LSPR calculated by UV-vis measurement at irradiation wavelength. The obtained linear relationship clearly suggests that the increases in catalytic performance under light irradiation were exclusively dependent on the particle color derived from Ag-LSPR. This result also indicates that maximum catalytic efficiency can be realized by using appropriate Ag catalysts under the light irradiation whose wavelength corresponds to their colors.

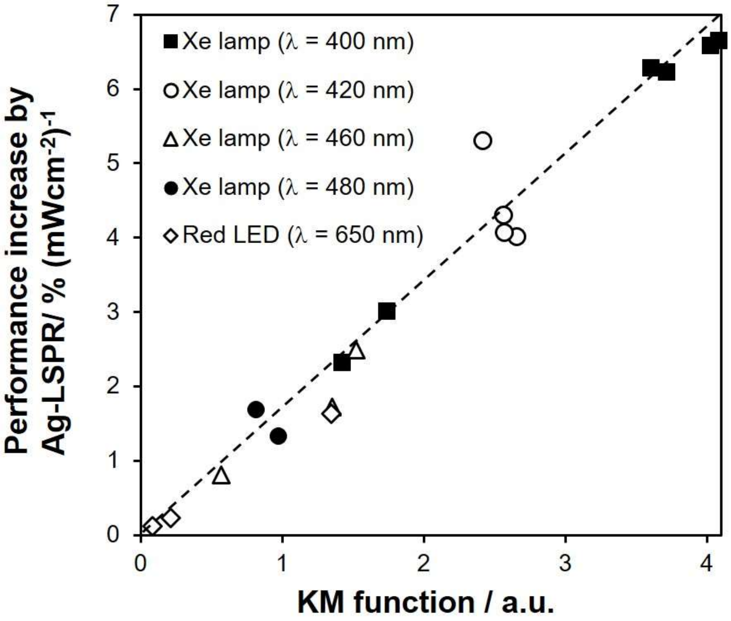

Figure 6. The relationship between the increasing rates of catalytic performance in the dehydrogenation of AB per light intensities and Kubelka-Munk (KM) function intensity derived from Ag-LSPR calculated by UV-vis measurement at irradiation wavelength.

Mechanistic investigation in H_2 production from ammonia borane

AB contains both three hydridic hydrogens and three protonic hydrogens owing to the difference between the electron negativities of B and N atoms; H atoms, which are bonded to the N atoms, carry a positive charge, while those bonded to the B atoms carry a negative charge ($NH_3^{\delta+}$–$BH_3^{\delta-}$).[39] Based on the experimental and theoretical studies, a plausible catalytic mechanism for AB dehydrogenation under dark conditions involves adsorption of AB onto the metallic NPs to form an activated complex species, followed by B–N bond cleavage by the attack of H_2O molecule to produce H_2.[40,41] On the other hand, H_2 production activity can be accelerated by the addition of a Lewis acid such as Co^{2+} ions, which can be simply explained by cooperative activation of NH_3BH_3 with the assistance of the electron-deficient Lewis acid sites through electron-rich NH_3 moiety.[41] Thus, I envisaged that the enhancement of catalytic activity by the Ag-LSPR effect is due to the change of local charge density of the Ag NP surface derived from the charge separation effect under light irradiation.

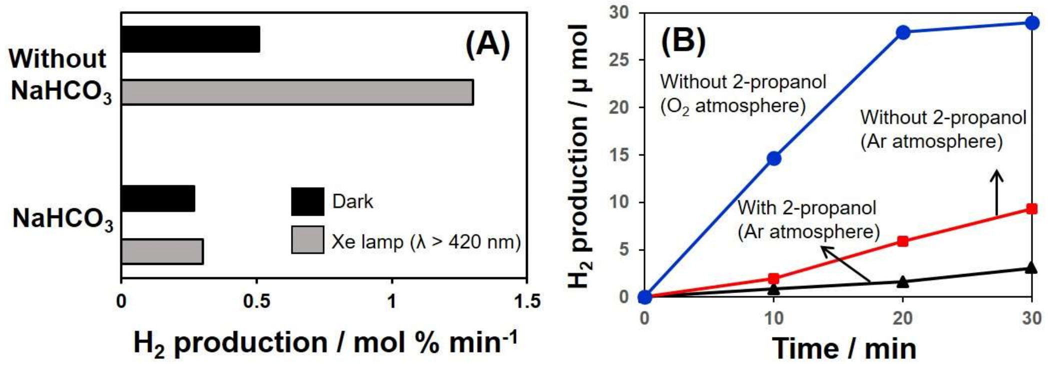

Figure 7. (A) Effect of addition of $NaHCO_3$ and (B) Effect of addition of 2-propanol and atmosphere.

The preliminary observations described below provide some insights into the reaction pathway. The addition of $NaHCO_3$ (100 μmol), a positive charge scavenger, to a suspension of Ag catalyst **6** significantly retarded the catalytic reaction under light irradiation by Xe lamp (λ > 420 nm) (Figure 7A), since HCO_3^- can interact with the generated h^+ (positive charge) on the Ag NPs.[42] The inhibition of catalytic activity by the $NaHCO_3$ is negligible under dark condition. These results indicate that the dehydrogenation of NH_3BH_3 is activated by the transitory deficient site of electron population of Ag NPs, which is produced by the cyclical charge separation derived from the Ag-LSPR plasma oscillation. After the dissociation of the B–N bonds, the generated positive $NH_3^{\delta+}$ might react with photoelectrons ($NH_3^{\delta+} + e^- + H_2O \rightarrow NH_4OH$), while the hydrolysis of the negative $BH_3^{\delta-}$ may spontaneously occur on the h^+ site ($BH_3^{\delta-} + h^+ + 2H_2 \rightarrow HBO_2 + 3H_2$). Moreover, the photogenerated superoxide anion radical (O_2^{-*}) and hydroxyl radical (•OH) may be also responsible for enhancing the catalytic activity.[43] The reaction upon purging with O_2 instead of Ar significantly increased the initial catalytic activity (Figure 7B). It can be suspected that the generated photo-electrons are continuously react with O_2 to form the O_2^{-*} ($O_2 + e^- \rightarrow O_2^{-*}$). The addition of the •OH radical scavenger 2-propanol significantly decreased catalytic activity (Figure 7B), which suggests that the efficient consumption of the excited electrons simultaneously promote the generation of holes (h^+) to produce •OH radical ($H_2O + h^+ \rightarrow$ •OH). Such highly active oxygen species under light irradiation may also attack the AB to dissociate the B–N bonds, which finally increase the initial reaction rate.

Plasmonic catalysis in reduction of 4-nitrophenol by AB

The reduction of aromatic nitro compounds by a facile and well-controlled way is important in organic synthesis chemistry because the obtained aromatic amines are valuable intermediates for the production of pharmaceutical, dye, polymer, and natural products.[44] Here, chemical reduction of 4-nitrophenol (4-NP) into 4-aminophenol was performed by a tandem reaction in which Ag serves a dual role to catalyse the dehydrogenation of AB and hydrogenation of 4-NP. Here, AB was employed as a convenient H_2 source instead of conventional $NaBH_4$ because of high stability and nontoxic property of AB.[31,45,46]

In the UV-vis spectra, 4-NP shows a strong absorption peak at 317 nm in neutral aqueous solution without Ag catalysts and AB. Upon addition of AB into the solution, a new absorption peak at 400 nm appears, which is caused by the formation of 4-NP anions by H^+ dissociation from 4-NP in basic AB solution. In the presence of Ag catalyst, the absorption peak intensity of 4-NP anions at 400 nm gradually decreases, accompanying the appearance of a new peak at 296 nm assigned to the 4-aminophenol.

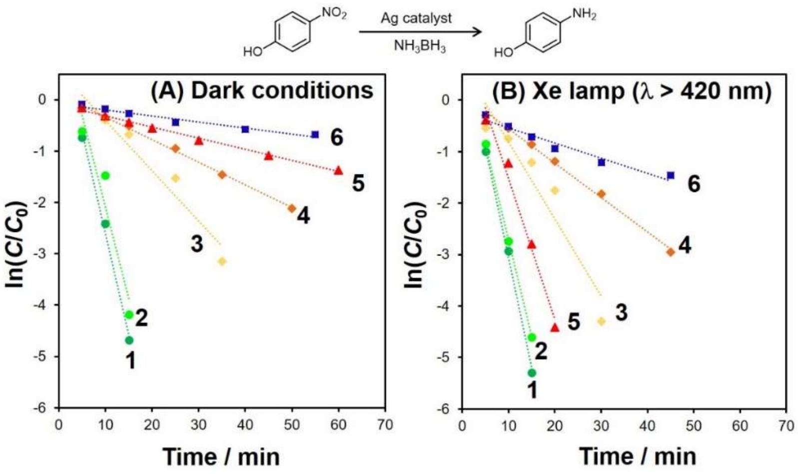

Figure 8. Plot of time versus ln(C/C_0) for 4-nitrophenol in the presence of Ag catalysts (A) under dark and (B) light irradiation conditions.

Figure 8A shows the time dependence of ln(*C*/*C*$_0$), in which *C* and *C*$_0$ denote the 4-NP concentration at time *t* and *t*$_0$, respectively. A rapid and linear evolution is observed without the induction period for all Ag catalysts, indicating a typical first-order reaction. In the presence of sufficient AB (H_2 source), apparent rate constants under dark conditions (k_{dark}) follow the order of Ag catalyst **1** > **2** > **3** > **4** > **5** > **6**. This order corresponds with the increase of Ag NP size. These results also suggest that both dehydrogenation of AB and the reduction of 4-NP occur on the surface Ag atoms of the NPs.

As expected, the catalytic performances of all Ag NPs were enhanced under light irradiation using Xe lamp (λ > 420 nm, 320 mW cm^{-2}). The apparent rate constants under light irradiation (k_{light}) follow the order of Ag catalyst **1** > **2** > **3** > **5** > **4** > **6 (**Figure 8B). The rate of increase in catalytic activity was dependent on the color of the Ag catalysts, and increased in the following order: **1** (1.20) < **2** (1.23) < **3** (1.58) < **4** (1.64) < **5** (2.09) < **6** (2.48), as shown in Figure 9. The values in parenthesis is a rate of increase. This tendency matched with the Ag-LSPR absorption intensity at wavelengths of more than 420 nm and well collaborated with the results obtained in the dehydrogenation of AB. Figure 10 summarized the relationship between the increasing rates of catalytic performance per light intensities and Kubelka-Munk (KM) function intensity derived from Ag-LSPR calculated by UV-vis measurement at irradiation wavelength using monochromatic light (λ = 400, 440, 460, 480, and 650 nm).

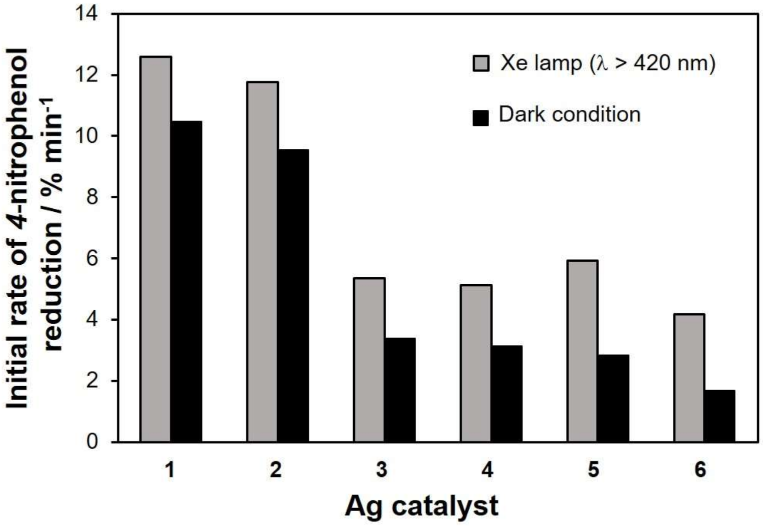

Figure 9. Comparison of initial rate of 4-nitrophenol reduction using AB in the presence of Ag catalysts under dark and light irradiation conditions.

The attained linear relationship is consistent with that obtained in the dehydrogenation of AB, and undoubtedly suggests that the particle color derived from Ag-LSPR plays an crucial role in increasing catalytic activity under light irradiation.

The Ag-catalysed tandem reaction of 4-NP reduction in the presence of AB spontaneously includes catalytic dehydrogenation of AB and reduction of 4-NP. Based on the catalytic results, the reaction under dark condition is particle size dependent, while the different activity order under light irradiation should be attributed to the Ag-LSPR effect. The rate of increase in catalytic activity in the reduction of 4-NP is almost consistent with those in the dehydrogenation of AB (Figure 4 vs. 9), thus indicating the dehydrogenation of AB may be the rate-determining step in the tandem reaction.

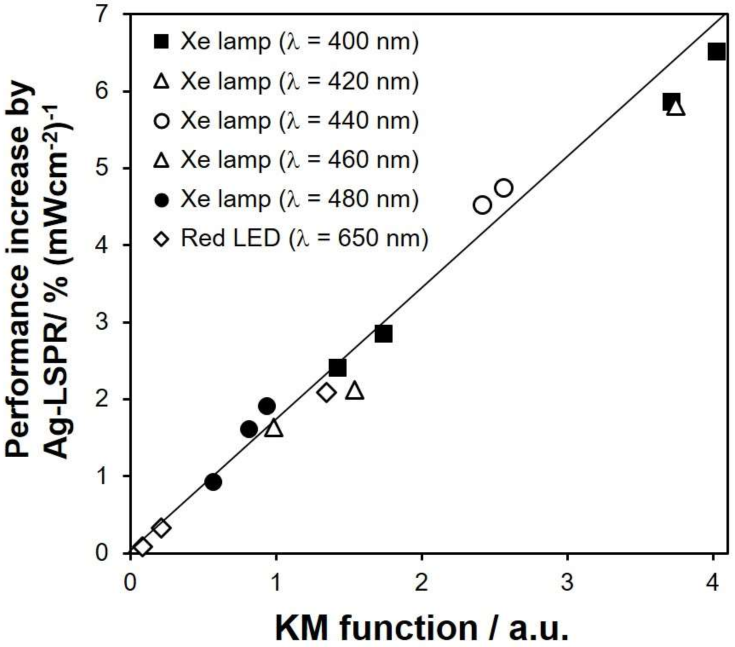

Figure 10. The relationship between the increasing rates of catalytic performance in the 4-nitrophenol reduction using AB per light intensities and Kubelka-Munk (KM) function intensity derived from Ag-LSPR calculated by UV-vis measurement at irradiation wavelength.

2.4 Conclusions

A facile MW-assisted deposition for the synthesis of size- and color-controlled Ag NPs has been developed in the absence or presence of surface-modifying ligands possessing different carbon chain length by combining with SBA-15 possessing confined mesoporous structure as a promising catalyst support. The smaller Ag NPs with yellow color exhibited higher catalytic activities in the dehydrogenation of AB under dark conditions, while catalytic performance under light irradiation increased with increasing the size of Ag NPs, especially blue Ag nanorod shows maximum enhancement. The order of increasing catalytic performance is in close agreement with the order of absorption intensity owing to the Ag-LSPR at irradiation light wavelength. A similar tendency in the LSPR-enhanced catalytic activity was observed in the tandem reaction consisting of dehydrogenation of AB and hydrogenation of 4-nitrophenol. The change of charge density of the Ag NP surface caused by charge separation derived from LSPR plays a crucial role in enhancing catalytic activity. The work developed in this chapter provides a novel strategy for the design of photocatalysts enabling efficient catalytic reactions under various light environments.

2.5 References

[1] K. Mori, M. Kawashima, M. Che and H. Yamashita, *Angew. Chem. Int. Ed.*, 2010, **49**, 8598.

[2] J. L. Duan, T. W. Cornelius, J. Liu, S. Karim, H. J. Yao, O. Picht, M. Rauber, S. Müller and R. Neumann, *J. Phys. Chem. C*, 2009, **113**, 13583.

[3] H. Cheng, K. Fuku, Y. Kuwahara, K. Mori and H. Yamashita, *J. Mater. Chem. A*, 2015, **3**, 5244.

[4] M. A. Noginov, G. Zhu, A. M. Belgrave, R. Bakker, V. M. Shalaev, E. E. Narimanov, S. Stout, E. Herz, T. Suteewong and U. Wiesner, *Nature*, 2009, **460**, 1110.

[5] J. N. Anker, W. P. Hall, O. Lyandres, N. C. Shah, J. Zhao and R. P. Van Duyne, *Nat. Mater.*, 2008, **7**, 442.

[6] S. Nie and S. R. Emory, *Science*, 1997, **275**, 1102.

[7] E. M. van Schrojenstein Lantman, T. Deckert-Gaudig, A. J. G. Mank, V. Deckert and B. M. Weckhuysen, *Nat. Nano.*, 2012, **7**, 583.

[8] S. Lal, N. K. Grady, J. Kundu, C. S. Levin, J. B. Lassiter and N. J. Halas, *Chem. Soc. Rev.*, 2008, **37**, 898.

[9] M. E. Stewart, C. R. Anderton, L. B. Thompson, J. Maria, S. K. Gray, J. A. Rogers and R. G. Nuzzo, *Chem. Rev.*, 2008, **108**, 494.

[10] D.-K. Lim, K.-S. Jeon, H. M. Kim, J.-M. Nam and Y. D. Suh, *Nat. Mater.*, 2010, **9**, 60.

[11] V. E. Ferry, L. A. Sweatlock, D. Pacifici and H. A. Atwater, *Nano Lett.*, 2008, **8**, 4391.

[12] S. Linic, P. Christopher and D. B. Ingram, *Nat. Mater.*, 2011, **10**, 911.

[13] K. L. Kelly, E. Coronado, L. L. Zhao and G. C. Schatz, *J. Phys. Chem. B*, 2003, **107**, 668.

[14] M. A. Mahmoud, M. Chamanzar, A. Adibi and M. A. El-Sayed, *J. Am. Chem. Soc.*, 2012, **134**, 6434.

[15] Y. Xie, S. Quinlivan and T. Asefa, *J. Phys. Chem. C*, 2008, **112**, 9996.

[16] A. Moores and F. Goettmann, *New J. Chem.*, 2006, **30**, 1121.

[17] S. K. Cushing, J. Li, F. Meng, T. R. Senty, S. Suri, M. Zhi, M. Li, A. D. Bristow and N. Wu, *J. Am. Chem. Soc.*, 2012, **134**, 15033.

[18] A. Tanaka, S. Sakaguchi, K. Hashimoto and H. Kominami, *Catal. Sci. Tech.*, 2012, 2, 907-909.

[19] X. Chen, H.-Y. Zhu, J.-C. Zhao, Z.-F. Zheng and X.-P. Gao, *Angew. Chem. Int. Ed.*, 2008, **47**, 5353.

[20] T. Fujita, P. Guan, K. McKenna, X. Lang, A. Hirata, L. Zhang, T. Tokunaga, S. Arai, Y. Yamamoto, N. Tanaka, Y. Ishikawa, N. Asao, Y. Yamamoto, J. Erlebacher and M. Chen, *Nat. Mater.*, 2012, **11**, 775.

[21] J. Robertson, *J. Vac. Sci. Techol. B*, 2000, **18**, 1785.

[22] A. Furube, L. Du, K. Hara, R. Katoh and M. Tachiya, *J. Am. Chem. Soc.*, 2007, 129, 14852.

[23] M. W. Knight, H. Sobhani, P. Nordlander and N. J. Halas, *Science*, 2011, **332**, 702.

[24] H. Zhu, X. Ke, X. Yang, S. Sarina and H. Liu, *Angew. Chem. Int. Ed.*, 2010, **49**, 9657.

[25] H. Zhu, X. Chen, Z. Zheng, X. Ke, E. Jaatinen, J. Zhao, C. Guo, T. Xie and D. Wang, *Chem. Commun.*, 2009, **48**, 7524.

[26] L. Gomez, V. Sebastian, M. Arruebo, J. Santamaria and S. B. Cronin, *Phys. Chem. Chem. Phys.*, 2014, **16**, 15111.

[27] X. Ke, X. Zhang, J. Zhao, S. Sarina, J. Barry and H. Zhu, *Green Chem.*, 2013, **15**, 236.

[28] K. Mori, K. Watanabe, M. Kawashima, M. Che and H. Yamashita, *J. Phys. Chem. C*, 2011, **115**, 1044.

[29] J. A. Gerbec, D. Magana, A. Washington and G. F. Strouse, *J. Am. Chem. Soc.*, 2005, **127**, 15791.

[30] K. Fuku, T. Kamegawa, K. Mori and H. Yamashita, *Chem. Asian J.*, 2012, **7**, 1366.

[31] X. Qian, Y. Kuwahara, K. Mori and H. Yamashita, *Chem. Eur. J.*, 2014, **20**, 15746.

[32] T. Yamamoto, Y. Wada, T. Sakata, H. Mori, M. Goto, S. Hibino and S. Yanagida, *Chem. Lett.*, 2004, **33**, 158.

[33] S. Link, M. B. Mohamed and M. A. El-Sayed, *J. Phys. Chem. B*, 1999, **103**, 3073.

[34] B. C. H. Steele and A. Heinzel, *Nature*, 2001, **414**, 345.

[35] H.-L. Jiang , S. K. Singh , J.-M. Yan , X.-B. Zhang and Q. Xu, *ChemSusChem*, 2010, **3**, 541.

[36] T. B. Marder, *Angew. Chem. Int. Ed.*, 2007, **46**, 8116.

[37] A. Staubitz, A. P. M. Robertson and I. Manners, *Chem. Rev.*, 2010, **110**, 4079.

[38] P. Christopher, H. Xin and S. Linic, *Nat. Chem.*, 2011, **3**, 467.

[39] D. West, S. Limpijumnong and S. B. Zhang, *Phys. Rev. B*, 2009, **80**, 064109.

[40] Q. Xu and M. Chandra, *J. Power Sources*, 2006, **163**, 364.

[41] R. Chiriac, F. Toche, U. B. Demirci, O. Krol and P. Miele, *Int. J. Hydrogen Energy*, 2011, **36**, 12955.

[42] C. Gomes Silva, R. Juárez, T. Marino, R. Molinari and H. García, *J. Am. Chem. Soc.*, 2011, **133**, 595.

[43] B. Pant, H. R. Pant, M. Park, Y. Liu, J.-W. Choi, N. A. M. Barakat and H.-Y. Kim, *Catal. Commun.*, 2014, **50**, 63.

[44] A. M. Tafesh and J. Weiguny, *Chem. Rev.*, 1996, **96**, 2035.

[45] X. Wang, D. Liu, S. Song and H. Zhang, *J. Am. Chem. Soc.*, 2013, **135**, 15864.

[46] H. Göksu, S. F. Ho, Ö. Metin, K. Korkmaz, A. Mendoza Garcia, M. S. Gültekin and S. Sun, *ACS Catal.*, 2014, **4**, 1777.

Chapter III

Synthesis and Characterization of a Pd/Ag Bimetallic Nanocatalyst on SBA-15 Mesoporous Silica as a Plasmonic Catalyst

3.1 Introduction

The proliferation of greenhouse gas emissions and climatic changes creates an urgency to replace fossil fuels with clean and renewable energy sources. An abundant and reliable source of solar energy is receiving immense interest to solve the problem of increasing energy demands and environmental concerns. The ultimate aim to solve the above issue is to carry out visible light driven photocatalytic reactions. In the past few decades, it has been observed that plasmonic nanostructures of noble metals (Ag, Au or Cu) can exhibit unique photocatalysis under visible light irradiation, which expands the prospect of various environmental and energy-related applications.[1-5] Plasmonic metal nanostructures are capable of transforming abundant solar energy into chemical energy by the localized surface plasmon resonance (LSPR).[6] LSPR can be described as the collective oscillation of valence electrons on establishing a resonance between the photons and surface electrons of nanoparticles (NPs), driven by the electromagnetic field of incident light.[7,8]

The integration of metal NPs over insulating nanoporous materials can be entitled as one of the most captivating technologies, among rapidly growing areas.[9-11] Unlike the metal NPs supported on semiconductor photocatalyst, the metal NPs over insulating solids encounter many advantages in terms of light harvesting and energy of the electrons.[12] Upon light irradiation, the photo-excited electrons of NP gain energy and accumulate on the surface, thereby assisting the activation of molecules for chemical reactions. A higher photon efficiency can be obtained since the light harvesting and reaction take place on a single site.[13] Among insulating solid supports, hexagonal mesoporous silica SBA-15 acts as a promising platform for metal NPs to efficiently couple the incident light energy on the surface of plasmonic metal NPs because of its good optical transparency in the visible light region.

Recently, the NPs consisting of more than two metallic components have stimulated much attention, owing to their unique catalytic, optical, electric and magnetic properties.[14] Noble metals incorporating bimetallic nanostructures are capturing more attention in diverse areas, due to their better catalytic activities than monometallic nanostructures. Many bimetallic structures such as Pt-based[15-18] and Pd-based[19-22] have been synthesized in order to enhance their catalytic activity. A detailed study indicates the significance of relative concentration and shape of metallic components, as they can tune activity of the reaction.

In the previous chapter, I studied the synthesis of size- and color-controlled Ag NPs by combining the use of SBA-15 support and a facile microwave-assisted deposition. The smaller Ag NPs with yellow color exhibited higher catalytic activities in the dehydrogenation of ammonia borane (NH_3-BH_3, AB) under dark conditions, while catalytic performance under light irradiation increased with increasing the size of Ag NPs, especially blue Ag nanorods showed a maximum enhancement. Herein I report the Pd/Ag bimetallic nanostructures supported on mesoporous silica SBA-15, in which Pd NPs were synthesized by a facile LSPR-assisted deposition on the highly dispersed Ag NPs with different sizes and morphologies under visible light irradiation. Pd NPs integrated with plasmonic Ag NPs or Ag nanorods create an efficient light harvesting system to achieve unique photocatalytic reactions. Pd is considered as one of the most active metals for a variety of catalytic reactions, but its inability to show plasmonic absorption inhibits the utilization of visible light energy, while Ag nanorods present an extensive light harvesting ability because of their size-dependent plasmonic absorption.[24] I envisaged and herein demonstrated that the coupling of plasmonic metal (Ag) with catalytically active component (Pd) can create a heterostructure exhibiting efficient catalytic activity in AB dehydrogenation and Pd-driven Suzuki-Miyaura coupling reaction.

3.2 Experimental

3.2.1 Materials

Tetraethyl orthosilicate ($(C_2H_5O)_4Si$)), hydrochloric acid (HCl), 1-hexanol ($C_6H_{13}OH$), acetone, silver nitrate ($AgNO_3$), sodium laurate, iodobenzene (C_6H_5I), palladium (II) acetate ($Pd(OAc)_2$), polyvinylpyrrolidone (PVP), potassium carbonate (K_2CO_3) and ethanol were purchased from Nacalai Tesque Inc. Triblock Pluronic P123® (Mw = 5800, $PEO_{20}PPO_{70}PEO_{20}$) and ammonia borane (NH_3BH_3) were obtained from Sigma-Aldrich Co. Phenylboronic acid was bought from Tokyo Chemical Industries Co. Ltd. All chemicals were used as received without any further purification.

3.2.2 Preparation of SBA-15

SBA-15 was synthesized according to the method reported in literature, using Pluronic P123® as a structure directing agent and tetraethyl orthosilicate as a silica source under acidic conditions (pH < 1).[26] In a typical procedure, P123 was dissolved in water and HCl with continuous stirring at 40 ˚C for 3 h at 400 rpm. TEOS was slowly added to the reaction mixture under vigorous stirring at 40° C for 24 h. The suspension was transferred to the Teflon bottle and aged at 80° C for 24 h. The obtained slurry was then filtered, washed with copious amount of deionized water and dried at 80° C overnight. The obtained white solid was finally calcined in air at 550° C for 5 h in order to remove the organic template.

3.2.3 Preparation of Ag/SBA-15

1 wt % of Ag NPs was incorporated within the mesoporous channels of SBA-15.[23,46] In a typical procedure, SBA-15 (0.396 g) was dispersed in 1-hexanol (40 mL) and ultrasonicated till it becomes a clear solution. An aqueous solution of $AgNO_3$ (0.037 mmol) and sodium laurate (10 mg) as a surface modifying ligand was added to the above solution under an Ar atmosphere. The solution was then irradiated by microwave (500 W, 2450±30 MHz) for different periods of time (3 or 5 min), with or without surface modifying agent. The resultant solution was filtered and washed with distilled water and acetone, followed by drying at 80 ˚C in air overnight. Three different-colored Ag/SBA-15 with different morphologies were synthesized by varying the microwave irradiation time. The obtained yellow, red, and blue Ag catalysts were denoted as Ag/SBA (Y), Ag/SBA-15 (R), and Ag/SBA-15 (B), respectively.

3.2.4 Preparation of Pd/Ag/SBA-15

0.1 wt% of Pd was deposited onto Ag/SBA-15 by plasmon-mediated deposition method under visible light irradiation. 0.1 g of Ag/SBA-15 was suspended and ultrasonicated in water (20 mL) until it becomes a clear solution. It was followed by bubbling Ar gas for a period of 30 min to ensure complete inert atmosphere. Subsequently, 0.482 mL of $Pd(OAc)_2$ solution (1.93 mM) was injected into the reaction mixture and irradiated with a Xe lamp (500 W; San-Ei Electric Co. Ltd. XEF-501S) with continuous stirring for 2 h. The resultant mixture was filtered, washed with distilled water and dried at 80˚C in air overnight. The obtained catalysts were denoted as Pd/Ag/SBA (Y), Pd/Ag/SBA-15 (R) and Pd/Ag/SBA-15 (B), respectively.

3.2.5 Characterization

The structural characteristics of Ag and Pd/Ag supported on SBA-15 silica were substantiated by UV-Vis, N_2 physisorption, X-ray diffraction (XRD), transmission electron microscopy (TEM), extended X-ray absorption fine structure (EXAFS), high angle annular dark field (HAADF) STEM Tomography and energy dispersive X-ray spectroscopy (EDS) mapping. The reflectance UV-Vis spectra of powdered samples were obtained by using Shimadzu UV-2450 spectrophotometer. BaSO4 was used as a reference and the absorption spectra were collected by using the Kubelka-Munk function. Nitrogen adsorption studies were performed by using BEL-SORP max system (BEL Japan, Inc.) at -196° C. In order to remove the adsorbed impurities, the samples were degassed in vacuum at 200° C for 3 h prior to analysis. TEM micrographs were obtained by using Hitachi Hf-2000 field emission-transmission electron microscope (FE-TEM) equipped with Kevex energy-dispersive X-ray detector operated at 200 kV. Ag K-edge and Pd K-edge X-ray absorption fine structure (XAFS) spectra were recorded by fluorescence-yield collection technique at beam line 01B1 station with an attached Si (111) monochromator at SPring-8, JASRI, Harima, Japan (Prop. No. 2015A1149). HAADF-STEM Tomography and EDS mapping results were performed by Sumika Chemical Analysis Service Ltd. using TITAN80-300 [FEI] of 80 kV. Powder X-ray diffraction (XRD) measurements were conducted by using a Rigaku RINT2500 Ultima IV X-ray diffractometer with Cu Kα radiation ($\lambda = 1.5406$ Å).

3.2.6 Hydrogen production from ammonia borane

Ammonia borane dehydrogenation reaction was carried out in order to examine the catalytic activity of the prepared catalysts. The Pd/Ag/SBA-15 (20 mg) catalyst was mixed with 5 mL of distilled water in a Pyrex vessel (30 mL), sealed with a rubber septum. The solution was then stirred and ultrasonicated to ensure the complete dispersion of the catalyst. Afterward, the system was purged with Ar gas for 30 min in order to maintain inert atmosphere. Subsequently, NH_3BH_3 (20 μmol) solution was injected through the rubber septum and stirred continuously under either dark conditions or photoirradiation at $\lambda > 420$ nm (320 mW cm^{-2}) using glass filter. An external fan was fitted in the reaction system in order to maintain the temperature of reaction vessel during the course of the reaction. Hydrogen evolution during the catalytic reaction was monitored by using Shimadzu GC-8A gas chromatograph.

3.2.7 Suzuki-Miyaura coupling reaction

The prepared catalyst, Pd/Ag/SBA-15 (100 mg) was mixed with 36.6 mg of phenylboronic acid (0.3 mmol) and 41.5 mg of anhydrous potassium carbonate (0.3 mmol) in 5.5

mL of ethyl alcohol solution in a Pyrex vessel (30 cm^3). It was then sealed with a rubber septum and bubbled Ar gas for about 30 min to maintain inert atmosphere. Afterwards, 0.022 mL of iodobenzene (0.3 mmol) was injected to the reaction mixture and irradiated with light using Xe lamp (500 W; San-Ei Electric Co. Ltd. XEF-501S) through a glass filter of $\lambda > 420$ nm with magnetic stirring at ambient temperature. An external fan was fitted in the reaction system in order to maintain the temperature of reaction vessel during the course of the reaction. The product formation was monitored by using Shimadzu GC-14B gas chromatograph.

3.3 Results and discussion

Synthesis and characterization of Ag/SBA-15 and Pd/Ag/SBA-15

According to previously established procedure,[23,46] color-controlled spherical Ag nanoparticles and nanorods, which are originated from their particle sizes and morphologies, can be synthesized within the mesoporous structure of SBA-15 by the rapid and uniform microwave (MW)-assisted alcohol reduction method in the absence or presence of surface-modifying organic ligands. The obtained Ag catalysts with different colors (yellow, red and blue) were denoted as Ag/SBA (Y), Ag/SBA-15 (R), and Ag/SBA-15 (B), respectively. Spherical nanosized Ag particles with a mean diameter of ca. 4 nm and a narrow size distribution were observed within the mesoporous channels of SBA-15 in Ag/SBA (Y) (Figure 1a), which was subjected to Mw irradiation for 3 min in the presence of Lau. In contrast, in Ag/SBA-15 (R) (Figure 1b) and Ag/SBA-15 (B) (Figure 1c), which were prepared without the use of surface-modifying ligands under Mw irradiation for 3 or 5 min, Ag nanorods grown parallel to the SBA-15 mesopores were observed. The aspect ratio of the Ag nanorods increased markedly with increasing Mw irradiation time. The average diameter of these Ag nanorods was ca. 10 nm, which was in close agreement with the pore size of SBA-15.

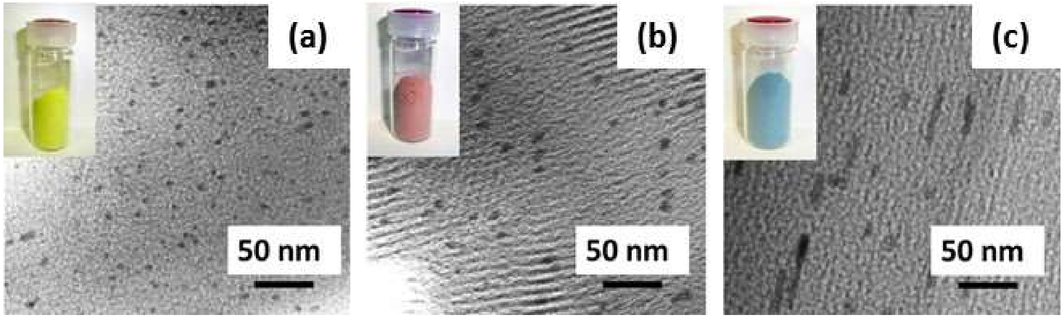

Figure 1. TEM images and sample photographs (inset) of (a) Ag/SBA-15 (Y), (b) Ag/SBA-15 (R) and (c) Ag/SBA-15 (B).

Figure 2 shows the UV-Vis spectra of color-controlled yellow, red and blue Ag nanocatalyst represented as Ag/SBA-15(Y), Ag/SBA-15(R) and Ag/SBA-15(B). A strong photo-absorption at around 420 nm is the characteristic LSPR absorption by Ag NPs. The geometrical symmetry of metal NPs influences the wavelength and intensity of LSPR peak in the spectrum. Different polarization modes arising from different shapes of metal nanostructures, can lead to number of LSPR peaks. For example; varying shapes of sphere, wire and cubes increases the LSPR peaks from one, two and three respectively.[6,30] Ag/SBA-15(Y), Ag/SBA-15(R) and Ag/SBA-15(B) were found to be associated with shapes of spherical, rods of short aspect ratio and rods of longer aspect ratio respectively. The aspect ratio of the Ag nanorods was found to increase with increasing Mw irradiation time. The two absorption peaks for Ag/SBA-15(R) and Ag/SBA-15(B) in the visible and infrared region can be attributed to the transverse (perpendicular) and longitudinal (parallel) mode of Ag nanorods.[33] The peak corresponding to longitudinal localized surface plasmon resonance of Ag/SBA-15(B) at λ =1200 nm accounts for longer aspect ratio of Ag nanorods. This broad peak can account for maximum light harvesting and hence developing an efficient catalyst for carrying out visible light driven reactions.

Pd/Ag bimetallic catalyst was prepared by LSPR-mediated deposition of Pd onto Ag under visible light irradiation. An efficient and uniform deposition of Pd can only be attained under photoirradiation by Xe lamp to activate the plasmonic Ag NPs. The optimization of suitable light source was also performed in order to acquire maximum catalytic activity, as discussed later. The possible galvanic reaction between Pd^{2+} ions and Ag NPs cannot be ignored, since the Pd NPs are forming on the surface of Ag without any reducing agent as shown in equation (1).

$$\mathrm{Ag\ (s)} + \mathrm{Pd}^{2+} \longrightarrow \mathrm{Ag}^{+} + \mathrm{Pd\ (s)}; \qquad E_0 = +\,0.12\ \mathrm{V} \qquad (1)$$

The net positive electrode potential implies the feasibility of the reaction, which can be further corroborated by its high value of equilibrium constant (K = 1.30×10^4).[27,28]

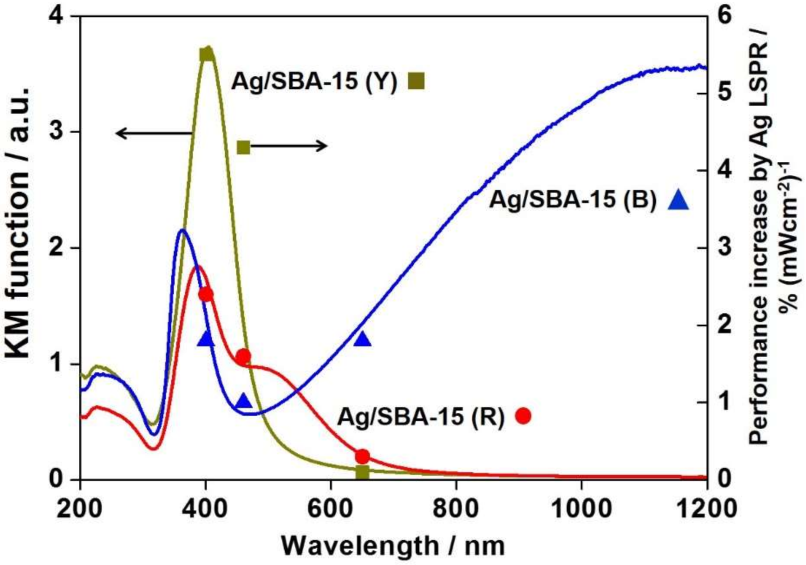

Figure 2. UV-vis spectra and wavelength dependence of the enhancement of catalytic activity of Ag/SBA-15 (Y), (R) and (B) under light irradiation of monochromatic light (λ = 400, 460) and red LED (λ_{max}=650 nm).

The N_2 adsorption-desorption isotherms of the prepared catalyst show type IV isotherm with hysteresis loop, which is characteristic for mesoporous materials. The pore volume and surface area calculated by Barrett-Joyner-Halenda (BJH) method and Brunauer-Emmett-Teller (BET) method are summarized in Table 1. Ag incorporation and the subsequent Pd deposition lead to a decrease in the pore volumes and surface area of the samples, supporting that the internal cavities of SBA-15 silica are being occupied by the Ag and Pd NPs. The minor decrease in the pore volume after Pd deposition may be attributed to its low weight percentage loading. However, the isotherm of all samples reveal the preservation of ordered mesoporous structure of SBA-15 even after the deposition of NPs.

Table 1. Textural properties of prepared catalysts.

Catalyst	**Pore volume (cm^{3}g^{-1})**	**BET surface area (m^{2}g^{-1})**
SBA-15	0.65	735
Ag(1.0)/SBA-15	0.58	679
Pd(0.1)/Ag(1.0)/SBA-15	0.56	606

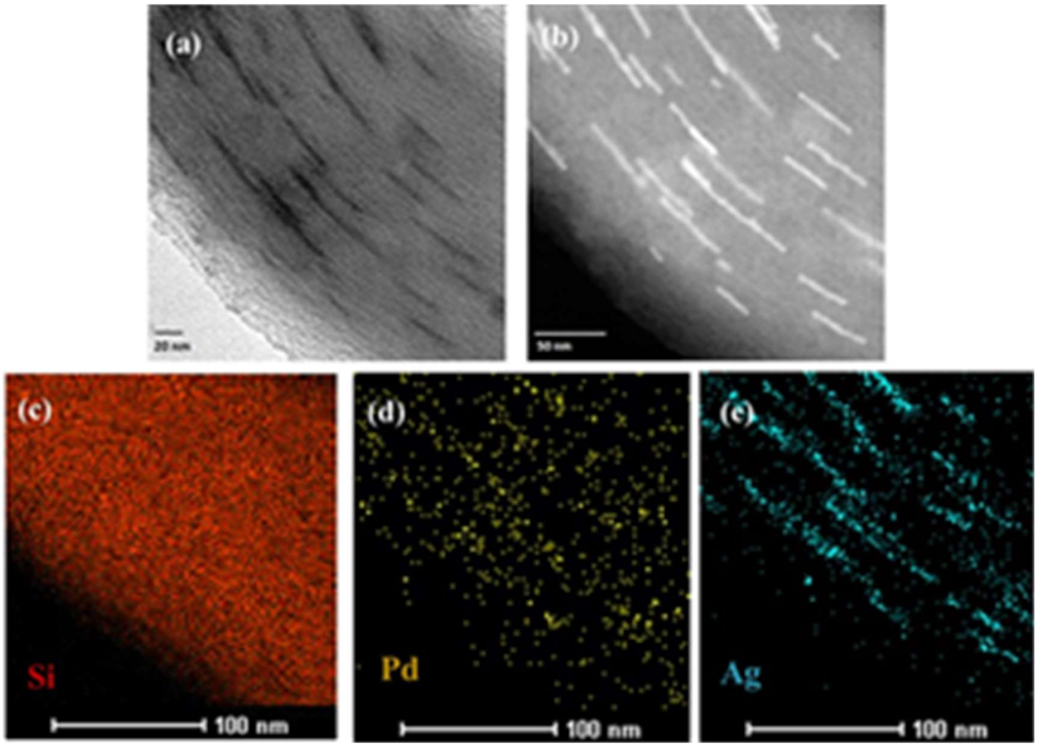

Figure 3. (a) TEM image of Pd/Ag/SBA-15, (b) HAADF-STEM image showing Pd/Ag/SBA-15, exclusively the nanorods, (c-e) Elemental analysis showing the relative composition of silicon, palladium and silver present in Pd/Ag/SBA-15.

The TEM image of Pd/Ag/SBA-15 (B) is shown in Figure 3a. It can be clearly seen that the elongated Ag nanorods were successfully loaded within the mesoporous channels of SBA-15. There was no significant change in the aspect ratio of Ag nanorods after deposition of Pd NPs. High Angle Annular Dark Field (HAADF) STEM image also revealed the long Ag nanorods grown parallel to the mesoporous channels of SBA-15 with an average aspect ratio of ca. 11 (Figure 3b). The EDS mapping unveiled the uniform dispersion of very small Pd NPs onto Ag nanorods within the surface of SBA-15, where Pd NPs being represented as yellow with Ag nanorods shown in blue color Figure 3 (c-e). The very low weight percentage of Pd NPs (0.1wt %)

via LSPR-assisted deposition over Ag nanorods (1.0 wt %) proves to be a simple and facile approach to synthesize highly dispersed bimetallic NPs. Pd deposition did not alter the morphology of any of the Ag NPs.

Figure 4 shows the UV-vis spectra of Pd/Ag/SBA-15 catalysts. Pd/Ag/SBA-15 (Y) showed one distinct peak at λ = 400 nm, which is similar to the original Ag/SBA-15. On the other hand, Pd/Ag/SBA-15 (R) and Pd/Ag/SBA-15 (B) showed two peaks attributable to transverse (λ=400 nm) and longitudinal (λ= 800-1200 nm) SPR of Ag nanorods. It can be concluded that the shapes of Ag NPs are retained even after the deposition of Pd.

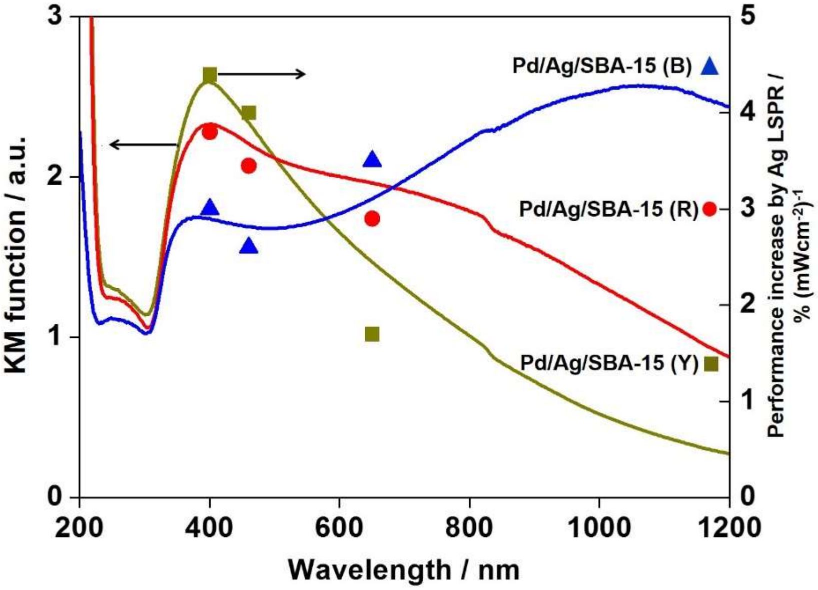

Figure 4. UV-vis spectra and wavelength dependence of the enhancement of catalytic activity of 0.1 wt % Pd deposited, Pd/Ag/SBA-15 (Y), (R) and (B) under light irradiation by monochromatic light (λ = 400, 460) and red LED (λ_{max}=650 nm).

It should be noted that the intensity of the plasmon peak decreased for all Pd/Ag/SBA-15 compared to the original Ag/SBA-15. The intensity and wavelength of LSPR absorption depends on size, morphology, and aspect ratio of Ag nanostructures. Thus, the broadening of the peaks may be attributed to the absorption interference by neighboring Pd NPs. It can be expected that this Ag-based plasmonic hybrid catalyst can harvest solar energy owing to its strong LSPR absorption in the visible region, which efficiently influence on the closely located Pd NPs via Pd/Ag interface owing to the charge heterogeneity originated from LSPR.

In order to investigate the electronic structure and chemical environment of Ag and Pd/Ag bimetallic NPs, extended X-ray absorption measurements were carried out. The Fourier transformation (FT) of k_3-weighted extended X-ray absorption fine structure (EXAFS) of all samples is shown in Figure 5A. A single peak at approximately 2.7 Å is assigned to the contiguous Ag–Ag bond in the metallic form. On the other hand, no peak due to Ag-O bond, detectable in that of AgO at around 1.7 Å, were observed. Pd K-edge XAFS results are also shown in Figure 5B. In the FT-EXAFS spectra, Pd/Ag/SBA-15 displays similar peak to that of Pd foil, confirming the metallic state of Pd NPs. The Pd–Pd distance in Pd/Ag/SBA-15 (B) sample, however, is found to be shorter than those of the pure Pd foil, suggesting the presence of Pd-Ag heteroatomic bonding.

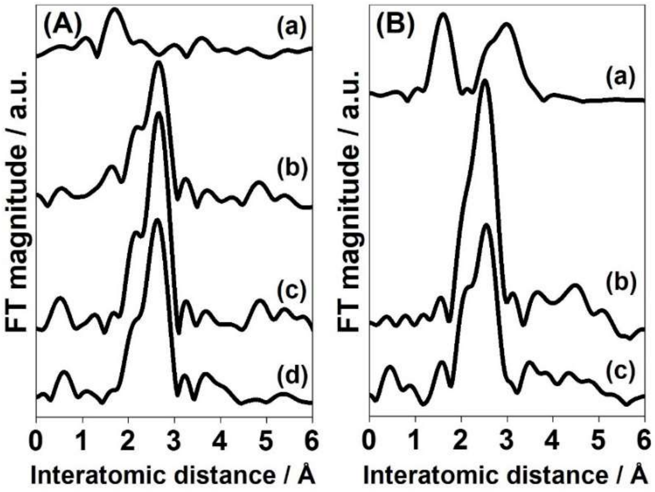

Figure 5. FT-EXAFS spectra of (A) Ag K-edge for (a) AgO, (b) Ag foil, (c) Ag/SBA-15 (B), (d) Pd/Ag/SBA-15 (B) and (B) Pd K-edge (a) PdO, (b) Pd foil, (c) Pd/Ag/SBA-15 (B).

Plasmonic Catalysis in H_2 production from ammonia borane

Ammonia borane has emerged as an attractive candidate for hydrogen storage applications because of its high hydrogen content (19.6 wt %).[25] The dehydrogenation of ammonia borane by thermal decomposition have already been extensively investigated.[35-38] An efficient catalyst can release 3 mol of H_2 / 1 mol of AB under ambient conditions as shown in Equation 2.

$$NH_3BH_3 + 2H_2O \longrightarrow NH_4^+ + BO_2^- + 3H_2 \qquad (2)$$

Recently, variety of metal nanostructures, such as Ru, Pt, Au and Pd, has been reported to exhibit high catalytic activity for hydrogen production from ammonia borane at ambient conditions.[39-41] Noble metals, possessing superior catalytic activities, are particularly desirable to develop highly efficient hydrogen generation systems.

Figure 6 displays the H_2 evolution from AB in dark conditions at room temperature (25 °C) for Ag/SBA-15 and Pd/Ag/SBA-15. No H_2 release was observed in the absence of catalyst, showing the inherent stability of NH_3BH_3 in water. In the case of Ag/SBA-15, Ag/SBA-15 (Y) with the smallest Ag particle size was a more efficient catalyst than Ag/SBA-15 (R) and (B) with bigger Ag particle sizes under dark condition. This result suggests that catalytic H_2 production from AB in dark conditions occurred on the exposed surface Ag atoms of Ag NPs. Upon deposition of Pd, the catalytic activity increased and the reactions completed within the first 30-40 min for all samples; the highest reaction rate of 3.22 mol % min^{-1} was attained by Pd/Ag/SBA-15 (Y), which is more than three times higher than that of Ag/SBA-15(Y) (0.94 mol % min^{-1}). The catalytic activity decreased in the order of Pd/Ag SBA-15(Y) > (R) > (B).

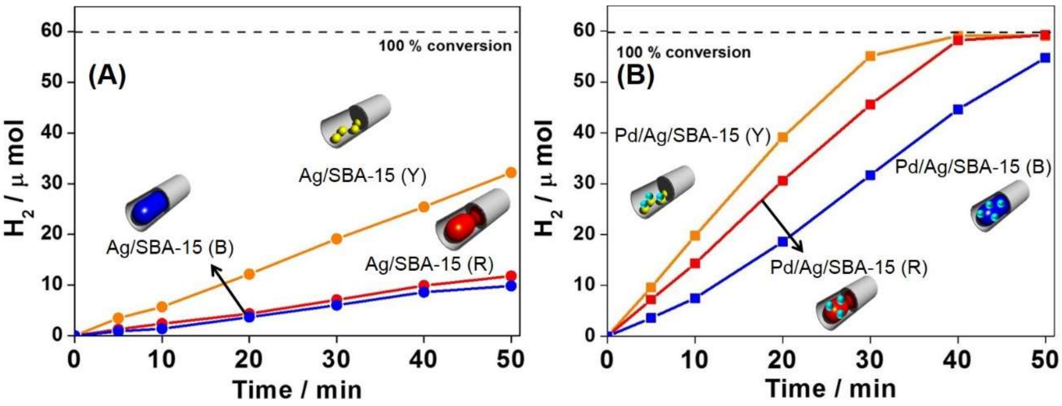

Figure 6. Time course of H_2 evolution from NH_3BH_3 aqueous solutions at room temperature using (A) Ag/SBA-15 and (B) Pd/Ag/SBA-15 catalysts under dark conditions.

Under visible light irradiation, the catalytic activities are specifically enhanced for all Ag/SBA-15 catalysts owing to the Ag-LSPR effect. Especially, the Ag/SBA-15 (B) showed a maximum enhancement more than five times as high as that observed under dark condition, while the enhancement effect of Ag/SBA-15 (Y) was relatively low in spite of its high activity under dark condition. Figure 7 summarizes the reaction rate enhancements for Ag/SBA-15 and Pd/Ag/SBA-15 catalysts under visible light irradiation conditions (λ > 420 nm). The tendency matches with the Ag-LSPR absorption intensity at wavelengths of more than 420 nm. Interestingly, the catalytic performance was further enhanced in the case of all Pd/Ag/SBA-15. The rate of catalytic activity enhancement was significantly dependent on the color of the Ag/SBA-15, and increased in the following order: Pd/Ag/SBA-15 (B) (2.56) > (R) (1.68) > (Y) (1.42) (the values in parenthesis are rates of activity increase upon visible light irradiation). This result well collaborated with the result obtained in the case of Ag/SBA-15 catalysts.

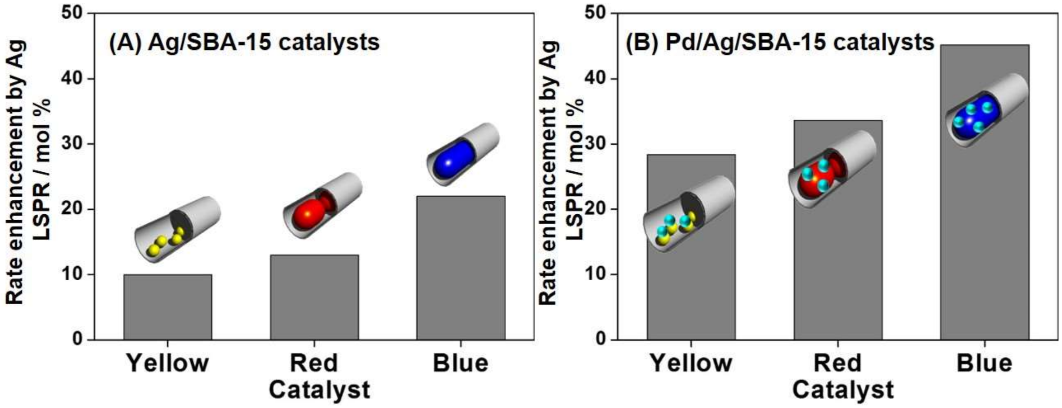

Figure 7. Rate enhancements for (A) Ag/SBA-15 and (B) Pd/Ag/SBA-15 catalysts under visible light irradiation conditions ($\lambda > 420$ nm, I = 320 mWcm^{-2}).

Figure 2 and 4 also show the performance increase by the wavelength dependence of catalytic performance over Ag/SBA-15 and Pd/Ag/SBA-15 using monochromatic light ($\lambda = 400$, 460, and 650 nm). In simple terms performance increase by Ag LSPR / % mW cm^{-2} can be explained as the percentage (%) of rate enhancement by using monochromatic light per unit intensity of the light used (mW cm^{-2}). The increasing rates of catalytic performance per light intensities were highly consistent with the LSPR absorption of these Ag NPs. These results undoubtedly suggest that the particle color derived from Ag-LSPR plays a crucial role in increasing catalytic activity under light irradiation.

The on/off effect of light irradiation was examined using the Pd/Ag/SBA-15 (B) catalyst as shown in Figure 8 (A), where light irradiation was initiated after the catalyst being left under the dark condition for 10 min. A significant enhancement was observed under light irradiation. Moreover, the slope of the activity after light irradiation was found to be same as that of activity under light irradiation from 0 min (reaction rate of 3.80 mol % min^{-1}). The spent catalyst could be recovered after dehydrogenation reaction and was found to exhibit its original activity both under dark and visible light irradiation. This fact indicates the reaction occurs on Pd/Ag NPs, not on the detached metal NPs.

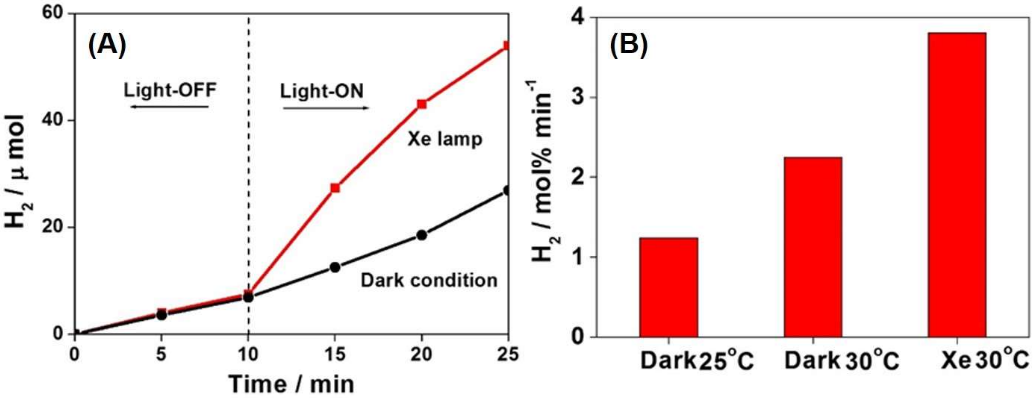

Figure 8. (A) Off-On effect of light irradiation for AB dehydrogenation using Pd/Ag/SBA-15 (B). (B) Effect of temperature for AB dehydrogenation under dark and light irradiation using Pd/Ag/SBA-15 (B).

The light originating from the Xe lamp at λ > 420 nm contains not only visible light but also a part of infrared light. It might be predicted that the enhancement of catalytic activity can be due to the thermal effect arising from infrared light. In fact the temperature of the reaction solution of Pd/Ag/SBA-15 (B) was found to increase by about 5°C under visible light irradiation. In order to elucidate the effect of infrared thermal heating, the reaction was carried out at 30°C under dark conditions using Pd/Ag/SBA-15 (B). The reaction rate of thermal reaction was found to be 2.25 mol % min^{-1}, which was higher than under dark conditions (1.24 mol % min^{-1}) at room temperature (25°C) but significantly lower than that attained under light irradiation (3.8 mol % min^{-1}) as shown in Figure 8 (B). Upon consideration of the above result, it can be concluded that the enhanced catalytic performance is originated essentially from the Ag-LSPR effect under visible light irradiation, and the contribution of the infrared thermal effect is insignificant. This can be well evidenced by the following equation (3) as previously reported by Christopher et al:

$$T = T_\infty + \frac{I_0 K_{abs}\, r_0}{6k_\infty} \tag{3}$$

The above equation can be used as a function of light intensity (I_0), absorption efficiency (K_{abs}), the diameter of metallic NP (r_0), the thermal conductivity of the surrounding medium (k_∞), and the heating temperature (T_∞). Including the experimental values I_0 = 320 mWcm^{-2}, r_0 = 4 – 50 nm, T_∞ = 298 K, and the values calculated by Christopher et al. (K_{abs} = 3, k_∞ = 40 mWm^{-1}K^{-1}), the temperature increase due to plasmonic heating effect in the present catalytic system was found to be less than 0.002 K. Upon consideration of the above result, it can be concluded that the enhanced catalytic performance originated largely from the Ag-LSPR effect under irradiation, and the contribution of the thermal effect was negligible.[42]

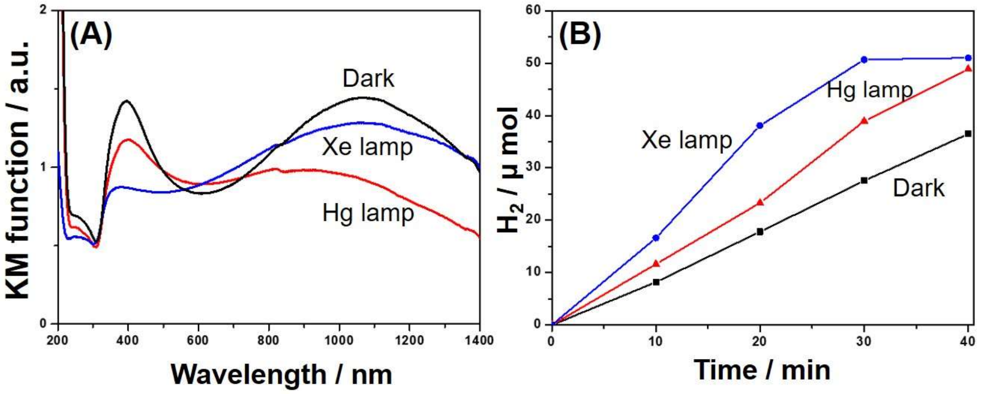

Figure 9. (A) UV-Vis of Pd/Ag/SBA-15 (B) under different light sources (Xe lamp, Hg lamp and dark conditions) and (B) Time course of hydrogen production in the AB dehydrogenation reaction over the Pd/Ag/SBA-15 (B) catalysts prepared using different light sources (Xe lamp, Hg lamp and dark conditions).

Ag-LSPR also plays an important role in the synthetic procedure of Pd deposition on Ag NPs and nanorods. For fabricating Pd/Ag/SBA-15 catalytic system with a maximized catalytic activity, the effect of light sources (Hg lamp, Xe lamp and dark conditions) during the Pd deposition was investigated using Pd/Ag/SBA-15 (B). In the UV-vis spectra, the intensity of plasmon peak at λ=400 nm decreased by changing the light source from dark conditions to Hg and Xe lamps (Figure 9A). Significant decrease under Xe lamp irradiation suggests the effective deposition of Pd NPs on the surface of Ag NP. This assumption was well evidenced in the investigation of catalytic activity (Figure 9B). The catalytic efficiency was found to be maximized when Xe lamp was used during the Pd deposition, which might be responsible for effectively activating the plasmonic Ag nanorods. Pd deposition under dark condition, in which Pd species were deposited by the galvanic reaction between Pd^{2+} ions and Ag NPs as mentioned earlier, resulted in the least active material, emphasizing the importance of light source for photo-assisted deposition.

The enhancement of catalytic activity in the H_2 production from ammonia borane under light irradiation can be explained by the charge heterogeneity arising from the Ag LSPR effect. Usually, in heterogeneous catalysis, the catalytic pathway of H_2 production from NH_3BH_3 is explained by an activated-complex theory, which involves adsorption of NH_3BH_3 onto metal NPs to form an activated complex. Next step involves the attack of activated complex by a water molecule to release H_2. In the case of Ag/SAB-15, Lewis acidic sites, which are generated on the surface of Ag NPs by the increasing surface charge density derived from the charge separation under light irradiation, enables the activation of Lewis basic NH_3BH_3, and thus effectively release H_2 molecules.[29] Similarly, superior performance of Pd/Ag system can be explained by the effective charge separation in the bimetallic system under visible light irradiation. Upon light irradiation, the plasmonic electrons (or so called hot electrons) generated in the Ag NPs stay in the *hot* state for a period of 0.5-1 ps.[44,45] Charge heterogeneity allows electron transfer from Ag to Pd to keep the chemical potential balances at the interface. Finally, this leads to accumulation of electrons on the surface of Pd, enabling better catalytic activity than Ag alone.

Plasmonic catalysis in Suzuki-Miyaura coupling reaction

Pd-catalyzed Suzuki-Miyaura coupling reaction, between aryl halides and nucleophiles, is one of the most utilized for carbon-carbon bond formation due to its mild reaction conditions and commercial availability of organoboron reagents.[31,32] Moreover, managing boron byproducts is relatively easier in large scale synthesis than other conventional coupling reactions (e.g. Kharash coupling, Negishi coupling and Stille coupling). Here, plasmonic Pd/Ag bimetallic catalysts were used in the Suzuki-Miyaura coupling reaction of iodobenzene and phenylboronic acid in the presence of potassium carbonate as a base, employing ethanol as a solvent for 6 h. I observed almost no catalytic activity (yield $< 1\%$) under dark conditions at room temperature (25°C) for 3 catalysts; Pd/Ag/SBA-15 (Y), Pd/Ag/SBA-15 (R) and Pd/Ag/SBA-15 (B) derived from yellow, red and blue color controlled Ag/SBA-15 respectively. This may be attributed to the absence of Ag-LSPR effect and very low weight percentage loading of Pd NPs. As expected, all

Pd/Ag bimetallic catalysts were found to be active for the coupling reaction under visible light irradiation corresponding to λ > 420 nm.

The increased yield of biphenyl was dependent on the color of the Ag catalysts, and increased in the following order: Pd/Ag/SBA-15 (Y) (2.16) < Pd/Ag/SBA-15 (R) (3.00) < Pd/Ag/SBA-15 (B) (3.33), as shown in Figure 10. The values in parenthesis are rates of catalytic activity enhancement. This tendency matches with the results obtained in the dehydrogenation of AB. It can be argued that the occurrence of reaction under visible light irradiation can be due to heating effect of infrared component of light irradiation. It was also found that temperature of reaction mixture increased by 10 °C, to eliminate this effect, the reaction was carried out at 35 °C ("Thermal" condition) and the contribution of conversion efficiency under light irradiation was evaluated. As summarized in Figure 10, superior performances were observed under light irradiation, followed by thermal condition and then reaction in dark; Pd/Ag/SBA-15 (B) exhibited 34 % yield under thermal condition (35˚C) and 53 % yield under visible light irradiation. These observations demonstrate clearly that the enhanced activity in the Suzuki-Miyaura coupling reaction under visible light irradiation might be attributed to the synergistic effect between Pd NPs and Ag NPs adjacently existing with each other by the assist of LSPR effect.

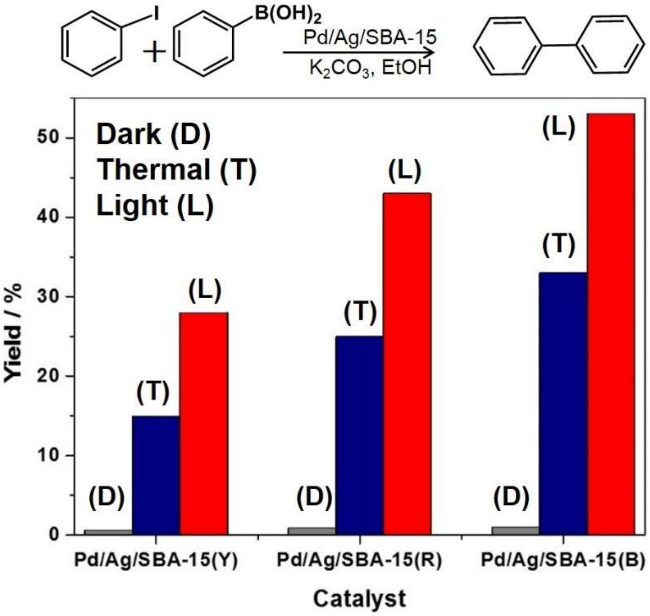

Figure 10. Suzuki-Miyaura coupling reaction for Pd/Ag/SBA-15 catalysts under dark, thermal (35 °C) and light irradiation conditions.

Upon irradiation of visible light, the energetic electrons generated on the Ag NPs transfers into the Pd NPs due to the charge heterogeneity existed in the abrupt atomic interface between Ag and Pd. This can be well supported with the argument that the work function of Pd metal is 5.00 eV from vacuum, which is larger than the work function of Ag metal equivalent to 4.30 eV from vacuum. The amount of energy required to eject the electron (work function) decides the position of the fermi level, suggests that the position of fermi level of Pd lies lower to that of Ag, making the electron transfer process feasible.[47,48] The oxidative addition step, which is the rate-determining step in Suzuki-Miyaura coupling reaction, may be accelerated by the activated Pd species, leading to the enhancement of intrinsic catalytic activity of Pd-catalyzed reaction. On the other hand, the energetic electrons release the energy to the surrounding environment, leading to the increase of temperature, which also contribute to the enhancement of catalytic activity.[43]

3.4 Conclusions

In summary, size- and color- controlled plasmonic Ag NPs were used to deposit Pd NPs to form Pd/Ag bimetallic plasmonic system. A straightforward and highly efficient method has been developed to produce uniformly dispersed bimetallic NPs within the channels of SBA-15. Among the color-controlled Ag NPs, the smaller Ag NPs with yellow color exhibited higher catalytic activities in the dehydrogenation of ammonia borane (NH_3-BH_3, AB) under dark conditions, while catalytic performance under light irradiation increased with increasing the size of Ag NPs, especially blue Ag nanorods showed a maximum enhancement. A similar trend in the catalytic activity and enhancement under visible light irradiation was found in the Pd deposited Ag NPs. Owing to its strong LSPR in the visible and near-infrared region, an enhanced catalytic activity by 40.8 mol % was observed for hydrogen production from AB with a reaction rate of 3.80 mol % min^{-1} under visible light irradiation. Pd/Ag bimetallic plasmonic catalyst was also found to display an activity in the Suzuki-Miyaura coupling reaction and an enhanced catalytic activity under visible light irradiation was observed. The work in this chapter demonstrates the efficient catalysis by Pd/Ag bimetallic nanostructures and provides novel approach for the functionalization of highly dispersed plasmonic materials. Therefore, such bimetallic Pd/Ag catalyst can form the basis of designing composites of plasmonic material-metal nanoparticle hybrid catalyst for visible-light-driven chemical reactions.

3.5 References

[1] S. Kumbhar, M. K. Kinnan and G. Chumanov, *J. Am. Chem. Soc.*, 2005, **127**, 12444.

[2] H. Chen, L. Shao, Q. Li and J. Wang, *Chem. Soc. Rev.*, 2013, **42**, 2679.

[3] G. H. Chan, J. Zhao, E. M. Hicks, G. C. Schatz and R. P. Van Duyne, *Nano Lett.*, 2007, **7**, 1947.

[4] P. Wang, B. Huang, Y. Dai and M.-H. Whangbo, *Phys. Chem. Chem. Phys.*, 2012, **14**, 9813.

[5] H. Cheng, K. Fuku, Y. Kuwahara, K. Mori and H. Yamashita, *J. Mater. Chem. A*, 2015, **3**, 5244.

[6] S. Linic, P. Christopher and D. B. Ingram, *Nat. Mater.*, 2011, **10**, 911.

[7] K. M. Mayer, J. H. Hafner and A. À. Antigen, *Chem. Rev.*, 2011, **111**, 3828.

[8] H. Cheng, T. Kamegawa, K. Mori and H. Yamashita, *Angew. Chem. Int. Ed.*, 2014, **53**, 2910.

[9] T. Kamegawa, D. Yamahana, H. Seto and H. Yamashita, *J. Mater. Chem. A*, 2013, 891.

[10] S. Okada, K. Mori, T. Kamegawa, M. Che and H. Yamashita, *Chem. Eur. J.*, 2011, **17**, 9047.

[11] R. J. White, R. Luque, V. L. Budarin, J. H. Clark and D. J. Macquarrie, *Chem. Soc. Rev.*, 2009, **38**, 481.

[12] P. Christopher, H. Xin, A. Marimuthu and S. Linic, *Nat. Mater.*, 2012, **11**, 1044.

[13] S. Sarina, S. Bai, Y. Huang, C. Chen, J. Jia, E. Jaatinen, G. a. Ayoko, Z. Bao and H. Zhu, *Green Chem.*, 2014, **16**, 331.

[14] Q. Li, R. Jiang, T. Ming, C. Fang and J. Wang, *Nanoscale*, 2012, **4**, 7070.

[15] J. Hong, S. Kang, B. Choi, D. Kim, S. Lee and S. Han, *ACS Nano*, 2012, **6**, 2410.

[16] J. Wu and H. Yang, *Nano Res.*, 2011, **4**, 72.

[17] Z. Zheng, T. Tachikawa and T. Majima, *J. Am. Chem. Soc.*, 2014, **136**, 6870.

[18] A. Tanaka, K. Hashimoto and H. Kominami, *J. Am. Chem. Soc.*, 2014, **136**, 586.

[19] H. Rong, S. Cai, Z. Niu and Y. Li, *ACS Catal.*, 2013, **3**, 1560.

[20] J. Xu, A. R. Wilson, A. R. Rathmell, J. Howe, M. Chi and B. J. Wiley, *ACS Nano*, 2011, **5**, 6119.

[21] K. Fuku, T. Sakano, T. Kamegawa, K. Mori and H. Yamashita, *J. Mater. Chem.*, 2012, **22**, 16243.

[22] H. Jing and H. Wang, *Chem. Mater.*, 2015, **27**, 2172.

[23] K. Fuku, R. Hayashi, S. Takakura, T. Kamegawa, K. Mori and H. Yamashita, *Angew. Chem. Int. Ed.*, 2013, **52**, 7446.

[24] G. Li, Y. Wang and L. Mao, *RSC Adv.*, 2014, **4**, 53649.

[25] Q. Xu and M. Chandra, *J. Power Sources*, 2006, **163**, 364.

[26] K. Mori, K. Watanabe, M. Kawashima, M. Che and H. Yamashita, *J. Phys. Chem. C*, 2011, **115**, 1044.

[27] C. L. Lee, C. M. Tseng, R. B. Wu, C. C. Wu and S. C. Syu, *Electrochim. Acta*, 2009, **54**, 5544.

[28] M. Navlani-García, M. Martis, D. Lozano-Castelló, D. Cazorla-Amorós, K. Mori and H. Yamashita, *Catal. Sci. Technol.*, 2015, **5**, 364.

[29] R. Chiriac, F. Toche, U. B. Demirci, O. Krol and P. Miele, *Int. J. Hydrogen Energy*, 2011, **36**, 12955.

[30] K. L. Kelly, K. L. Kelly, E. Coronado, L. Zhao, E. Coronado, G. C. Schatz, L. L. Zhao and G. C. Schatz, *J. Phys. Chem. B*, 2003, **107**, 668.

[31] N. Miyaura and A. Suzuki, *Chem. Rev.*, 1995, **95**, 2457.

[32] K. Mori, M. Kawashima and H. Yamashita, *Chem. Commun.*, 2014, **50**, 1.

[33] S. Link, M. B. Mohamed and M. a El-Sayed, *J. Phys. Chem. B*, 1999, **103**, 3073.

[34] M. A. Majeed Khan, S. Kumar, M. Ahamed, S. a Alrokayan and M. S. Alsalhi, *Nanoscale Res. Lett.*, 2011, **6**, 434.

[35] G. Wolf, J. Baumann, F. Baitalow and F. . Hoffmann, *Thermochim. Acta*, 2000, **343**, 19.

[36] J. Baumann, F. Baitalow and G. Wolf, *Thermochim. Acta*, 2005, **430**, 9.

[37] A. Gutowska, L. Li, Y. Shin, C. M. Wang, X. S. Li, J. C. Linehan, R. S. Smith, B. D. Kay, B. Schmid, W. Shaw, M. Gutowski and T. Autrey, *Angew. Chem. Int. Ed.*, 2005, **44**, 3578.

[38] S. De Benedetto, M. Carewska, C. Cento, P. Gislon, M. Pasquali, S. Scaccia and P. P. Prosini, *Thermochim. Acta*, 2006, **441**, 184.

[39] J. Yan, X. Zhang, T. Akita, M. Haruta and Q. Xu, *J. Am. Chem. Soc.*, 2010, **132**, 5326.

[40] M. Yadav and Q. Xu, *Energy Environ. Sci.*, 2012, **5**, 9698.

[41] M. Chandra and Q. Xu, *J. Power Sources*, 2007, **168**, 135.

[42] P. Christopher, H. Xin and S. Linic, *Nat. Chem.*, 2011, **3**, 467.

[43] F. Wang, C. Li, H. Chen, R. Jiang, D. Sun, Q. Li, J. Wang, J. C. Yu, C. Yan and L. Sun, *J. Am. Chem. Soc.,* 2013, **135**, 5588.

[44] C. Wang and D. Astruc, *Chem. Soc. Rev.*, 2014, **43**, 7188.

[45] X. Zhang, Y. L. Chen, R.-S. Liu and D. P. Tsai, *Rep. Prog. Phys.*, 2013, **76**, 046401.

[46] K. Mori, P. Verma, R. Hayashi, K. Fuku and H. Yamashita, *Chem. Eur. J.*, 2015, **21**, 11885.

[47] A. Tanaka, K. Fuku, T. Nishi, K. Hashimoto and H. Kominami, *J. Phys. Chem. C*, 2013, **117**, 16983.

[48] A. Tanaka, K. Nakanishi, R. Hamada, K. Hashimoto and H. Kominami, *ACS Catal*., 2013, **3**, 1886.

Chapter IV

Enhancement of Plasmonic Activity by Pt/Ag Bimetallic Nanocatalyst Supported on Mesoporous Silica in the Hydrogen Production from Hydrogen Storage Material

4.1 Introduction

The perpetual advancements in nanofabrication and nanoparticle (NP) synthesis technologies are leading to the birth of innumerable applications of plasmonics in many different research fields and hence making it as one of the most dynamic and fascinating branch of Nanophotonics.[1-3] In the past two decades, the surface plasmons of noble metals have fueled immense research activities and its applications in surface-enhanced spectroscopies,[4] bio sensing,[5] lasers,[6] photovoltaics[7] and photocatalysis.[8] The tremendous efforts and recent advancements have already witnessed a new insight to the fundamentals of plasmonic systems. [9] Recently, it has been identified as a powerful tool to combine optics with nanoscience and nanotechnology, enabling control of hot charge carriers by manipulating light absorption within femtoseconds at nanoscale regimes.[9,10] The direct photocatalytic reactions are driven by noble metal NPs due to the presence of accessible active sites and generation of hot electrons by localized surface plasmon resonance (LSPR) effect.[11,12] A myriad of preparative methods have been developed till now to synthesize metal NPs of different size and morphology viz. sphere,[13] rods,[14] cubes[15] and prisms.[16] The synthesis of Au-Ag alloyed nanoboxes (hollow interior) and nanocages (porous walls) reported recently is one of the example to demonstrate the composition control of NPs.[17] As per recent report from Yuan Li group, the theoretical calculations depict the presence of a special plasmonic resonance (SPR) mode at the interphase of bimetallic core shell structure, in addition to the ordinary mode at surface.[18]

Bimetallic nanostructures have attracted significant attention due to their unique optical, catalytic, electronic, magnetic properties in comparison to monometallic and bulk metal alloys.[19] The enhanced performance of bimetallic NPs can be rationalized by electronic (charge transfer), geometric and synergistic effects.[20] Variety of approaches has been reported till date to synthesize bimetallic NPs viz. polyol process,[21] wet chemical,[22] galvanic,[23] electrochemical,[24] photochemical[19] or LSPR-assisted deposition.[13] The development of highly dispersed bimetallic NPs supported on mesoporous materials provides an opportunity to design catalytically-active advanced functional materials. In continuation of my previous studies on bimetallic plasmonic systems,[13,14,25] herein, I report the synthesis of Pt/Ag NPs supported on silica. The quest of developing more and more active and visible light efficient catalytic systems motivated me to study the combination of most active metals of transition series. Significant efforts have already been made to study the combination of Pt/Au NPs, but Pt/Ag combination is still not so well known in exploration of plasmonic effect of Ag in combination with Pt.[26]

The growing threat of energy exhaustion and global warming makes the development of sustainable and clean energy production extremely urgent. Hydrogen (H_2) has been regarded as one of the most qualified candidates in terms of its clean burning and high energy density.[27] However, the difficulty in storage and transportation limits its widespread application.[28,29] Recently, ammonia borane (NH_3-BH_3, AB) has received immense attention as a hydrogen storage material owing to its high hydrogen content (19.6 wt %), low molecular weight (30.87 g mol^{-1}), non-toxicity and high stability at room temperature.[30] Therefore, H_2 production from AB was employed a model reaction to compare the catalytic activities of the prepared catalysts under dark and visible light irradiation.

4.2 Experimental

4.2.1 Materials

Tetraethyl orthosilicate ($((C_2H_5O)_4Si)$), hydrochloric acid (HCl), 1-hexanol ($C_6H_{13}OH$), acetone, silver nitrate ($AgNO_3$), Chloroplatinic acid (H_2PtCl_6), sodium laurate, and ethanol were purchased from Nacalai Tesque Inc. Triblock pluronic P123® (Mw = 5800, $PEO_{20}PPO_{70}PEO_{20}$) and ammonia borane (NH_3BH_3) were obtained from Sigma-Aldrich Co. All chemicals were used as received without any further purification.

4.2.2 Synthesis of SBA-15

Mesoporous silica SBA-15 was synthesized according to the method reported in literature utilizing Pluronic P123® as a structure directing agent and tetraethyl orthosilicate (TEOS) as a silica source under acidic conditions ($pH < 1$).[31]

4.2.3 Synthesis of Ag/SBA-15

The incorporation of Ag (1 wt %) onto SBA-15 (0.396 g) was carried out by microwave assisted alcohol reduction method. At first, the silica support was ultrasonicated well with 1-hexanol (40 mL) for 30 min. Further, sodium laurate (surface directing agent, 10 mg) and precursor $AgNO_3$ aqueous solution (100 mmol, 0.4 mL) was injected into the solution followed by Ar bubbling for 15 min. The resultant mixture was then exposed to microwave irradiation (500

W) for a period of 3 min. The solution was then filtered and dried in air at 80 ˚C. The obtained catalyst was named as Ag/SBA-15.

4.2.4 Synthesis of Pt/Ag/SBA-15

Four different weight percentages of Pt (0.1, 0.25, 0.5 and 1.0 wt %) were deposited onto Ag/SBA-15 by plasmon-mediated deposition method under visible light irradiation. 0.1 g of Ag/SBA-15 was suspended and ultrasonicated in water (20 mL) until it becomes a clear solution. It was followed by bubbling Ar gas for a period of 30 min to ensure complete inert atmosphere. Subsequently, varying amounts of H_2PtCl_6 solution (1.5 mM) was injected into the reaction mixture and irradiated with a Xe lamp (500 W; San-Ei Electric Co. Ltd. XEF-501S) with continuous stirring for 2 h. The Pt ions were further reduced by employing hydrazine (N_2H_4) as a reducing agent. The resultant mixture was centrifuged, washed with distilled water and acetone and dried in vacuum overnight at room temperature. The obtained catalysts were denoted as Pt(x)/Ag/SBA, where x represents the weight percentage amount of Pt on Ag.

4.2.5 Characterization

The overall characterization of the prepared support and catalysts was established by UV-vis, N_2 physisorption, transmission electron microscopy (TEM), and X-ray photoelectron spectroscopic (XPS) analysis. Shimadzu UV-2450 spectrophotometer was used to collect the reflectance UV-vis spectra of powdered samples. $BaSO_4$ was used as a reference solid and the spectra were collected by employing Kubelka-Munk function. Brunauer–Emmett–Teller (BET) surface area measurements were performed by using a BEL-SORP max system (MicrotracBEL) at -196° C. Degassing of the samples was done in vacuum at 200° C for 3 h in order to remove the adsorbed impurities. TEM micrographs were obtained with a Hitachi Hf-2000 FE-TEM equipped with Kevex energy-dispersive X-ray detector operated at 200 kV. ESCA-3400 electron spectrometer was used to characterize samples for X-ray photoelectron spectroscopy. Ag K-edge XAFS spectra were recorded in fluorescence-yield collection technique mode at the beam line 01B1 station with an attached Si (111) monochromator (2016A1095). XAFS data were examined using the REX2000 program (Rigaku).

4.2.6 Catalytic reaction

The catalytic reaction of dehydrogenation of AB was carried out in an aqueous suspension of catalysts. Briefly, 20 mg of catalyst was dispersed in distilled water (5 mL) in a Pyrex vessel (32 mL), sealed with a rubber septum. After bubbling Ar gas for 30 min, AB (20 μmol) was injected through the rubber septum and stirred continuously under either dark conditions or photo irradiation (320 mW cm^{-2}). A 500 W Xenon lamp (San-Ei Electric Co. Ltd. XEF-501S) was used to carry out reactions under visible light irradiation. The amount of hydrogen in the gas phase was measured by using Shimadzu GC-14B gas chromatograph equipped with a TCD detector.

4.3 Results and discussion

Figure 1 shows the TEM micrographs along with their pertinent histograms and diagrammatic illustration for Ag and Pt/Ag NPs supported on mesoporous silica (SBA-15). SBA-15 displayed well-ordered mesoporous structure (as seen in TEM), which was further confirmed by low-angle X-ray diffraction (XRD) and N_2 physisorption measurement studies as discussed later. The mean diameter of NPs was found to be approximately 3.18 and 4.15 nm for Ag and Pt/Ag NPs respectively, with a narrow size distribution. MW assisted process for the synthesis of Ag NPs was found to be very efficient in growing NPs within the hexagonal channels of mesoporous silica. After Pt deposition, there observed no specific change in the morphology of Ag NPs, however slight size increment was observed for PtAg bimetallic NPs.

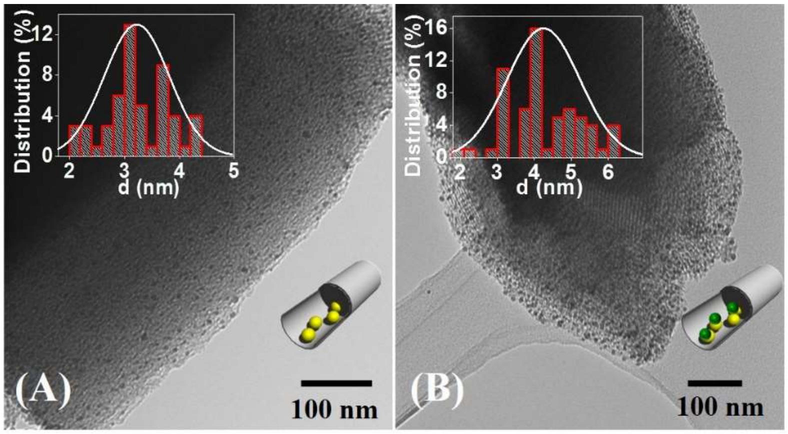

Figure 1. TEM micrographs along with pertinent histograms for (A) Ag/SBA-15 and (B) Pt(0.25)/Ag/SBA-15.

To design plasmonic nanostructures with efficient visible light sensitivity, it is essential to display distinct absorption along with high catalytic performance. Till date, synthesizing NPs with uniform shape and narrow size distribution, exhibiting intense absorption in the visible region is still a great challenge. In order to characterize the prepared catalysts, surface plasmon resonance (SPR) property was investigated by diffuse reflectance UV-vis absorption spectroscopy. The morphological shape and size of NPs can affect the intensity and wavelength of LSPR peak in the spectrum. Also, the number of LSPR peaks is dependent on the different polarization modes arising from different shapes of metal NPs. For example spheres, rods and cubes gives rise to one, two and three peaks in the UV-vis spectrum respectively. Figure 2 shows the UV-vis spectra of prepared catalysts including SBA-15 (mesoporous silica), Ag/SBA-15 and Pt(x)/Ag/SBA-15 (where x = 0.1, 0.25. 0.5, 1.0 represents the weight percentage ratio of Pt deposited on Ag). All catalysts exhibited one intense plasmonic peak at wavelength range of 420 nm, also indicating the spherical shape NPs. The presence of the plasmonic peak even after the incorporation of second metal (Pt) confirmed the retention of plasmonic behavior in all prepared catalysts. The continuous decrease in the intensity of Ag plasmonic peak on increasing the Pt weight % ratio, confirms the surface coverage of Ag by Pt. The Ag and Pt/Ag samples were found to be yellow colored, evidently explaining the strong absorption in the visible region.

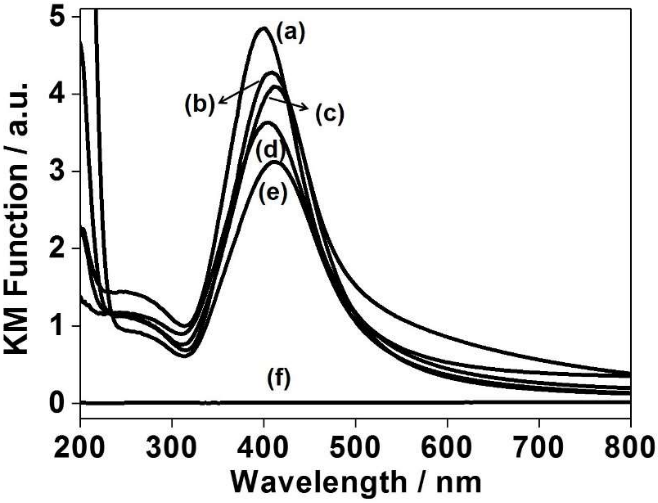

Figure 2. UV-vis spectra of prepared catalysts (a) Ag/SBA-15, (b) Pt(0.1)/Ag/SBA-15, (c) Pt(0.25)/Ag/SBA-15, (d) Pt(0.5)/Ag/SBA-15, (e) Pt(1.0)/Ag/SBA-15 and (f) SBA-15.

To further characterize the mesoporous structure of the materials, N_2-physisorption measurement studies were carried out. All catalysts exhibited typical H1-type hysteresis loop with a sharp inflexion at pressure range of 0.7 in their isotherms as shown in Figure 3 (A). The pore size distribution has also been represented in Figure 3 (B). The detailed textural properties including surface area, pore size and pore volume has been summarized in Table 1. The surface area and mesoporous volume of SBA-15 decreased from 671 to 571 m^2 g^{-1} and 1.1 to 0.98 cm^3 g^{-1} respectively for Ag/SBA-15, while 671 to 490 m^2 g^{-1} and 1.1 to 0.79 cm^3 g^{-1} respectively for Pt(0.25)/Ag/SBA-15. The successive decrease observed on increasing the Pt weight percentage, in the pore volume and surface area indicates the occupancy of void spaces by NPs.

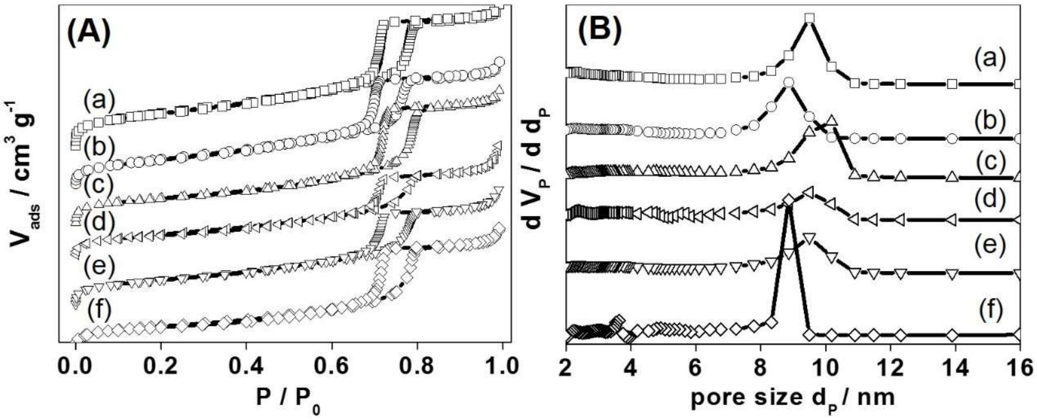

Figure 3. (A) N_2 physisorption isotherms and (B) Pore size distribution for (a) SBA-15, (b) Ag/SBA-15, (c) Pt(0.1)/Ag/SBA-15, (d) Pt(0.25)/Ag/SBA-15, (e) Pt(0.5)/Ag/SBA-15 and (f) Pt(1.0)/Ag/SBA-15.

Table 1. Textural properties determined by N_2-physisorption measurements

Materials	**Surface area (m^2g^{-1})**	**Pore size (nm)**	**Pore volume (cm^3g^{-1})**
SBA-15	671	9.49	1.1
Ag/SBA-15	571	8.86	0.98
Pt(0.1)/Ag/SBA-15	508	10.18	1.02
Pt(0.25)/Ag/SBA-15	490	9.49	0.79
Pt(0.5)/Ag/SBA-15	527	9.49	0.87
Pt(1.0)/Ag/SBA-15	466	8.86	0.91

The Ag K-edge X-ray absorption near-edge structure (XANES) spectra of Ag/SBA-15, Pt/Ag/SBA-15, Ag foil and AgO is represented in Figure 4 (A). The observable two peaks and edge position of Ag foil resemble to Ag/SBA-15 and Pt/Ag/SBA-15, but differ from the peak spectra of AgO. Hence, the prepared catalysts possess similar electronic properties and Ag in zero oxidation state. Also, the white line, which is the characteristic small peak for Ag after the edge jump was observed. The slight decrease in the intensity after the deposition of Pt is suggestive of the interaction between Pt and Ag.[32,33]

Extended X-ray absorption fine structure (EXAFS) measurement studies were carried out to elucidate the local structure of NPs supported on mesoporous silica. Figure 4 (B) shows the Ag K-edge Fourier transforms (FT) EXAFS spectra for Ag/SBA-15 and Pt/Ag bimetallic catalyst along with standard samples including Ag foil and Ag oxide (AgO). All samples exhibited an intense peak at 2.7 Å attributed to the contiguous Ag-Ag metallic bonding, similar to that of Ag foil. This confirms the presence of Ag^0 species in Ag and bimetallic Pt/Ag samples. The recognizable different peak at approximately 1.9 Å for AgO represents Ag-O-Ag bonding.

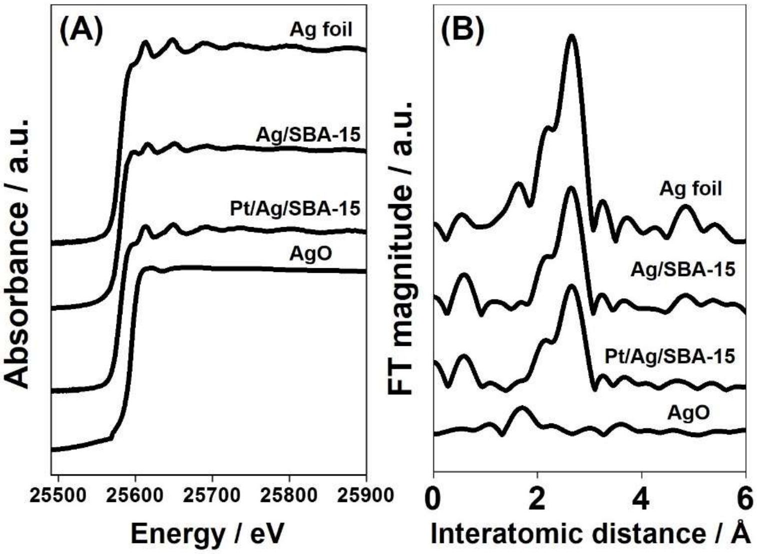

Figure 4. (A) Ag K-edge XANES spectra and (B) FT-EXAFS for Ag/SBA-15, Pt/Ag/SBA-15, Ag foil and AgO.

The X-ray photoelectron spectroscopy (XPS) measurement spectra for Ag/SBA-15 and Pt(x)/Ag/SBA-15, to characterize the surface composition and chemical state of prepared samples has been summarized in Figure 5. The Ag 3d core level spectrum representing two strong peaks due to the splitting of 3d doublet by 6.0 eV confirms the metallic nature of Ag. The peaks observed at binding energies of 376.1 eV and 370.1 eV are ascribed to $3d_{3/2}$ and $3d_{5/2}$ core levels of Ag in Ag/SBA-15 respectively. I observed a successive shift by 0.1 eV for Pt (0.25), Pt (0.5) and Pt(1.0)/Ag/SBA-15 samples towards higher binding energies. The shift in the binding energy of Pt/Ag towards higher values in comparison to the monometallic Ag NPs implies the oxidation of Ag, owing to the net charge transfer from Ag to Pt. This transfer from Ag atoms and making electron rich Pt species, occur due to the net difference in their electronegativity values (Ag: 1.93 and Pt: 2.28). Thus, XPS provides an advantage to display the existence of heterojunction via electron transfer mechanisms situated adjacent to each other.

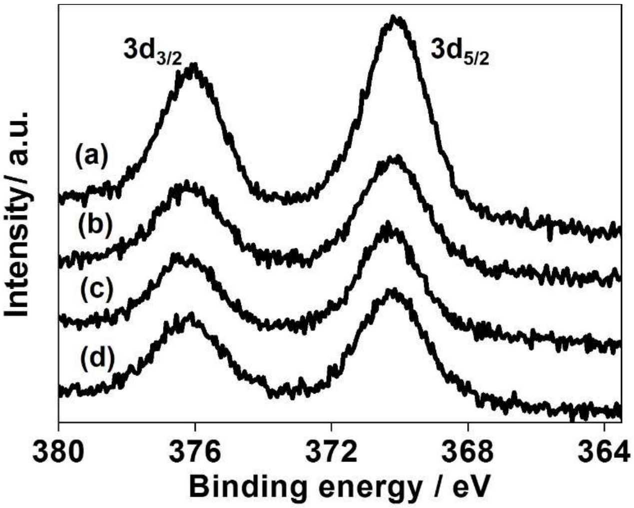

Figure 5. XPS Ag 3d spectra for (a) Ag/SBA-15, (b) Pt(0.25)/Ag/SBA-15, (c) Pt(0.5)/Ag/SBA-15 and (d) Pt(1.0)/Ag/SBA-15.

The hydrogen production from AB can take place via two processes viz. pyrolysis and hydrolysis. Pyrolysis takes place at considerably higher temperatures and produces only 1 equivalent of hydrogen (6.5 wt %), whereas hydrolysis in the presence of suitable catalyst yields 3 equivalents (19.6 wt %) of hydrogen as per equation 1.[34]

$$NH_3BH_3 + 2H_2O \longrightarrow NH_4^+ + BO_2^- + 3H_2 \qquad (1)$$

Among various investigated cases of AB hydrolysis in homogenous and heterogeneous systems, various different catalysts have been well explored and reported. Apart from monometallic catalysts like Ag, Au, Ru, Rh and Pt, various bimetallic and trimetallic combinations have also been explored, for example, Pd/Ag, Pd/Au, RuNi, PtRh, RuCo, PtNiAu have been reported in the literature.[35-37]

Figure 6 summarizes the results obtained in the present study utilizing Pt(x)/Ag/SBA-15 bimetallic catalyst with varying ratio of Pt deposited on Ag. It was found out that on increasing the Pt wt % on Ag, the catalytic activity was also increased, attaining saturation at 1:1 (Pt: Ag) wt % ratio with a reaction rate of 1.16 μmol min^{-1}. The highest reaction rate of 1.26 μmol min^{-1} was shown by Pt(0.5)/Ag/SBA-15 while a decreased rate for Pt(1.0)/Ag/SBA-15 (1.16 μmol min^{-1}) was observed under dark conditions. All catalysts showed an enhanced rate under visible light irradiation with highest rate of 1.69 μmol min^{-1} shown by Pt(1.0)/Ag/SBA-15. However, the enhancement extent was found to be maximum for 0.25 wt % of Pt on Ag. Enhancement factor (R_L/R_D) was calculated to study the differences in the rate of the reaction in dark and light condition by the simple division of reaction rate under light (R_L) and dark (R_D) conditions.

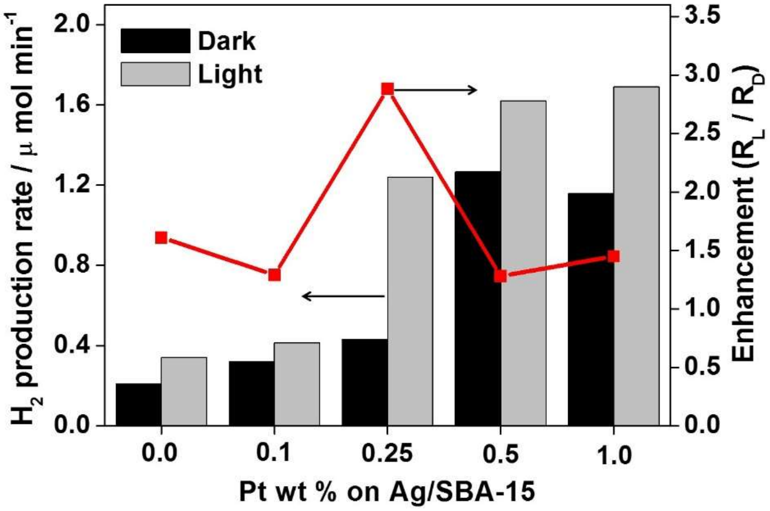

Figure 6. Catalytic activity and corresponding enhancements for Ag/SBA-15 and Pt(x)/Ag/SBA-15 where x = 0.1, 0.25, 0.5 and 1.0.

The enhancement factor for Pt(0.25)/Ag/SBA-15 was found to be 2.88. This observed enhancement is also the highest ever from my previously reported results of monometallic and bimetallic spherical NPs.[13,14,25] This enhancement can be attributed to the synergistic catalysis and optimum ratio of Pt (0.25) on Ag (1.0), giving rise to unique catalytic activity under light irradiation conditions for hydrogen production reaction.

The on/off effect of light irradiation was studied utilising Pt(0.25)/Ag/SBA-15 catalyst for AB dehydrogenation as summarized in Figure 7 (A). In the beginning, the catalytic activity was monitored for initial 30 min under dark conditions, followed by light irradiation for the next 60 min. A sudden increase in the reaction rate under visible light irradiation on switching from light off to on condition was observed. Also, the slope of the activity curve was found to be the same as that of activity monitored under light irradiation from 0 min. A significant enhancement after light irradiation validates the plasmonic effect of prepared catalyst.

Light originating from Xe lamp contains portions of visible and infrared light. It can be argued that the enhancements might be occurring due to the thermal effects arising from infrared light. Therefore, thermal reaction was carried out to study the effect of heating by infrared light. As shown in Figure 7 (B), the reaction rate of thermal reaction was found to be 0.65 μmol min^{-1}, which is higher than in dark conditions (0.43 μmol min^{-1}) but significantly lower than that of light irradiation conditions (1.24 μmol min^{-1}). Hence, it can be concluded that the enhanced reaction rate essentially arises from the LSPR effect of Ag NPs. This has already been evidenced by the equation 2 reported by Christopher et al.

$$T = T_{\infty} + \frac{I_0 K_{abs}\ r_0}{6k_{\infty}} \qquad (2)$$

Where I_0 is the light intensity, K_{abs} is the absorption efficiency, r_0 is the diameter of metallic NP, k_{∞} is the thermal conductivity of the surrounding medium and T_{∞} is the heating temperature. As per the above equation, the temperature increase due to plasmonic heating effect in present catalytic system was found to be less than 0.002 K upon inserting experimental values $I_0 = 320$ $mWcm^{-2}$, $r_0 = 4 – 50$ nm, $T_{\infty} = 298$ K and the values calculated by Christopher et al. ($K_{abs} = 3$, k_{∞} =40 $mWm^{-1}K^{-1}$).[38]

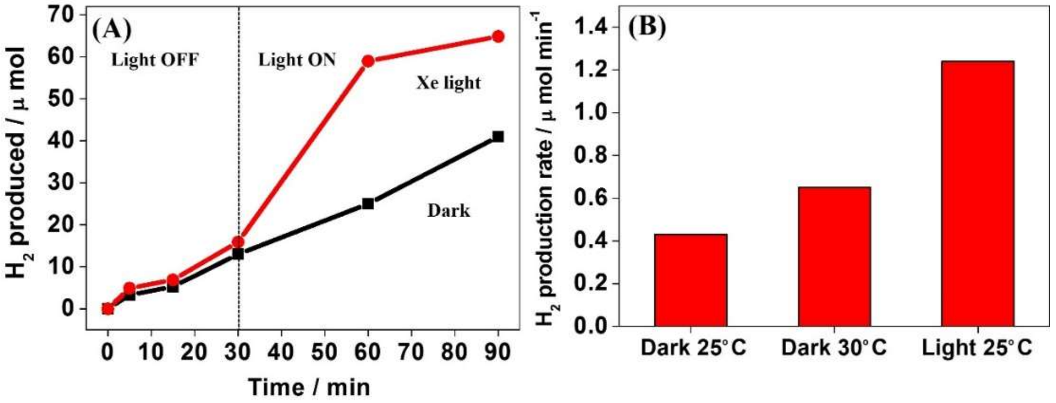

Figure 7. (A) Off-on effect of light irradiation and (B) Effect of temperature under dark and light irradiation for AB dehydrogenation using Pt(0.25)/Ag/SBA-15.

Stability and recycling ability play an important role in order to design an active and efficient catalyst. The stability of Pt(0.25)/Ag/SBA-15 was investigated by carrying out recycling experiments under dark and visible light irradiation. In every successive cycle, AB was injected again and catalytic activity was monitored by using GC. As shown in Figure 8, the reaction rate of 1.24 μmol min^{-1} was found to be consistent enough under light irradiation conditions. The catalytic activity still remained high even after the 3rd run, indicating the stability of the prepared catalyst.

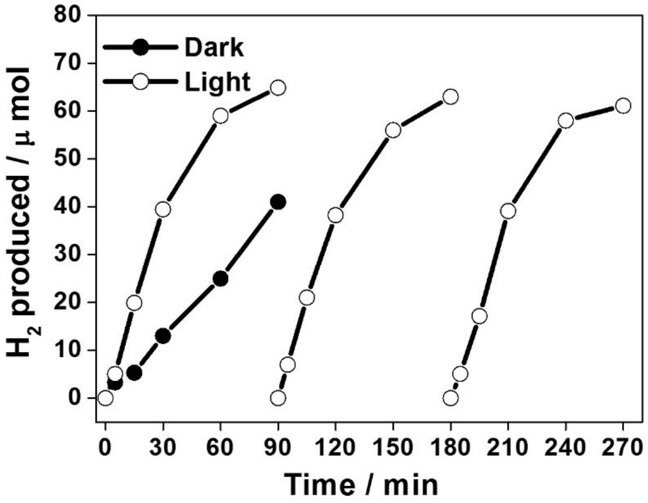

Figure 8. Stability test for AB dehydrogenation over Pt(0.25)/Ag/SBA-15 catalyst under dark and visible light irradiation up to 3 consecutive runs.

A plausible mechanism involving the tentative reaction pathway has been proposed to understand the enhanced reaction rate under visible light irradiation. Upon light irradiation, the electron hole pairs are generated as per non-radiative Landau damping phenomenon for metal NPs of diameter equal to or less than 30 nm.[39] The plasmonic or the hot electrons generated due to resonant excitation undergoes possible relaxation within 0.5-1 ps.[40] The positioning of the fermi level of Pt lower to that of Ag leads to the net electron transfer from Ag to Pt as illustrated in Scheme 1. This process occurs due to substantial lower work function values of Ag (4.3 eV) than Pt (5.4 eV) from vacuum.[41] The hot electrons further injected to the lowest unoccupied molecular orbital (LUMO) of the reactant molecules to generate ionic species leading to their bond elongation.[42] The electrons tentatively further return back to plasmonic NPs via highest occupied molecular orbital (HOMO). Many theoretical and calculative studies have also proved and reported the similar pathway followed by plasmonic metal NPs.

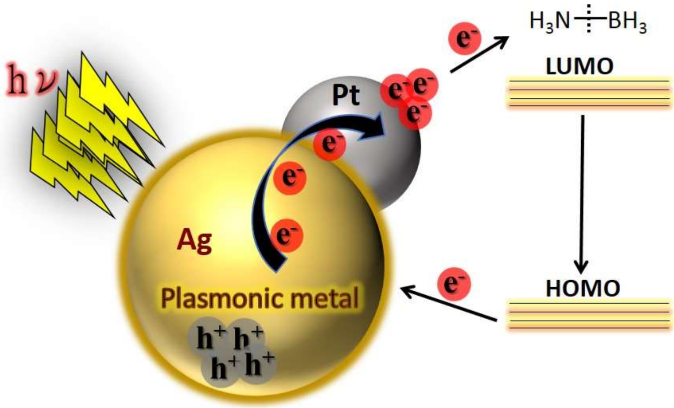

Scheme 1. Illustration of the Pt/Ag system and possible electron transfer pathway for AB dehydrogenation under visible light irradiation

4.4 Conclusions

In summary, I have developed a Pt/Ag bimetallic plasmonic nanocatalyst supported within the channels of mesoporous silica. By varying the ratio of Pt on Ag, 0.25 wt % of Pt on Ag (1.0 wt %) was found to exhibit maximum enhancement (2.88) and superior catalytic activity with a reaction rate of 1.24 µmol min^{-1}. The enhanced reaction rate under visible light irradiation has been demonstrated by proposing a tentative electron pathway for the AB dehydrogenation reaction. The effects of temperature and light were also carefully studied and explained, in order to elucidate the effect of thermal infrared heating. I hope that such development and advancements of LSPR-assisted catalysis will surely impact large scale energy and environmental aspects in the upcoming years.

4.5 References

[1] J.N. Anker, W.P. Hall, O. Lyandres, N.C. Shah, J. Zhao and R.P. Van Duyne, *Nat. Mater.*, 2008, **7**, 442.

[2] P.R. West, S. Ishii, G. V. Naik, N.K. Emani, V.M. Shalaev and A. Boltasseva, *Laser Photonics Rev.*, 2010, **4**, 795.

[3] (a) H. Cheng, M. Wen, X. Ma, Y. Kuwahara, K. Mori, Y. Dai, B. Huang and H. Yamashita, *J. Am. Chem. Soc.*, 2016, **138**, 9316; (b) H. Cheng, X. Qian, Y. Kuwahara, K. Mori, H. Yamashita, *J. Mater. Chem. A.*, 2015, **27**, 4616; (c) X. Meng, L. Liu, S. Ouyang, H. Xu, D. Wang, N. Zhao, J. Ye, *Adv. Mater.*, 2016, **28**, 6781.

[4] S. Gwo, C.-Y. Wang, H.-Y. Chen, M.-H. Lin, L. Sun, X. Li, W.-L. Chen, Y.-M. Chang and H. Ahn, *ACS Photonics*, 2016, **3**, 1371.

[5] M.E. Stewart, C.R. Anderton, L.B. Thompson, J. Maria, S.K. Gray, J.A. Rogers and R.G. Nuzzo, *Chem. Rev.*, 2008, **108**, 494.

[6] V.K. Valev, D. Denkova, X. Zheng, A.I. Kuznetsov, C. Reinhardt, B.N. Chichkov, G. Tsutsumanova, E.J. Osley, V. Petkov, B. De Clercq, A. V. Silhanek, Y. Jeyaram, V. Volskiy, P.A. Warburton, G.A.E. Vandenbosch, S. Russev, O.A. Aktsipetrov, M. Ameloot, V. V. Moshchalkov and T. Verbiest, *Adv. Mater.*, 2012, **24**, 29.

[7] (a) C.H. Chou and F.C. Chen, *Nanoscale*, 2014, **6**, 8444. (b) H.A. Atwater and A. Polman, *Nat. Mater.*, 2010, **9**, 865.

[8] X. Zheng and L. Zhang, *Energy Environ. Sci.*, 2016, **9**, 2511.

[9] C. Ropers, D.J. Park, G. Stibenz, G. Steinmeyer, J. Kim, D.S. Kim and C. Lienau, *Phys. Rev. Lett.*, 2005, **94**, 113901. (b) P.K. Jain, X. Huang, I.H. El-Sayed and M.A. El-Sayed, *Plasmonics*, 2007, **2**, 107.

[10] S. Linic, P. Christopher and D.B. Ingram, *Nat. Mater.*, 2011, **10**, 911.

[11] M.L. Brongersma, N.J. Halas and P. Nordlander, *Nat. Nanotechnol.*, 2015, **10**, 25.

[12] (a) S. Mukherjee, F. Libisch, N. Large, O. Neumann, L. V Brown, J. Cheng, J.B. Lassiter, E. a Carter, P. Nordlander and N.J. Halas, *Nano Lett.*, 2013, 13, 240. (b) M. Sun and H. Xu, *Small*, 2012, **8**, 2777.

[13] P. Verma, Y. Kuwahara, K. Mori and H. Yamashita, *J. Mater. Chem. A.*, 2016, **4**, 10142.

[14] K. Fuku, R. Hayashi, S. Takakura, T. Kamegawa, K. Mori and H. Yamashita, *Angew. Chem. Int. Ed.*, 2013, **52**, 7446.

[15] M. Zhu, P. Chen, W. Ma, B. Lei and M. Liu, *ACS Appl. Mater. Interfaces.*, 2012, **4**, 6386.

[16] R. Jin, Y.C. Cao, E. Hao, G.S. Métraux, G.C. Schatz and C. A. Mirkin, Nature, 2003, **425**, 487.

[17] (a) X. Lu, L. Au, J. McLellan, Z.Y. Li, M. Marquez and Y. Xia, *Nano Lett.*, 2007, **7** 1764. (b) J. Zeng, Q. Zhang, J. Chen and Y. Xia, *Nano Lett.*, 2010, **10**, 30.

[18] C. Zhang, B.-Q. Chen, Z.-Y. Li, Y. Xia and Y.-G. Chen, *J. Phys. Chem. C.*, 2015, **119**, 16836.

[19] (a) K.J. Major, C. De and S.O. Obare, *Plasmonics*, 2009, **4**, 61. (b) M. Zienkiewicz-Strzałka, A. Deryło-Marczewska and S. Pikus, *Microporous Mesoporous Mater.*, 2016, **227**, 228–241.

[20] D. Manchon, J. Lermé, T. Zhang, A. Mosset, C. Jamois, C. Bonnet, J.-M. Rye, A. Belarouci, M. Broyer, M. Pellarin and E. Cottancin, *Nanoscale*, 2015, **7**, 1181.

[21] K. Baranowska, J. Okal and W. Tylus, *Appl. Catal. A Gen.*, 2016, **511**, 117.

[22] S. Guo, D. Wen, Y. Zhai, S. Dong and E. Wang, *ACS Nano.*, 2010, **4**, 3959.

[23] P. Verma, Y. Kuwahara, K. Mori and H. Yamashita, *J. Mater. Chem. A.*, 2015, **3**, 18889.

[24] S.-S. Chang, C.-L. Lee and C.R.C. Wang, *J. Phys. Chem. B.*, 1997, **101**, 6661.

[25] K. Mori, P. Verma, R. Hayashi, K. Fuku and H. Yamashita, *Chem. Eur. J.*, 2015, **21**, 11885.

[26] H. Lang, S. Maldonado, K.J. Stevenson and B.D. Chandler, *J. Am. Chem. Soc.*, 2004, **126**, 12949.

[27] U. Eberle, M. Felderhoff and F. Schuth, *Angew. Chem. Int. Ed.*, 2009, **48**, 6608.

[28] A.W.C. van den Berg and C.O. Areán, *Chem. Commun.*, 2008, 668.

[29] J. Yang, A. Sudik, C. Wolverton, D.J. Siegel, *Chem. Soc. Rev.*, 2010, **39**, 656.

[30] E.K. Abo-Hamed, T. Pennycook, Y. Vaynzof, C. Toprakcioglu, A. Koutsioubas and O.A. Scherman, *Small*, 2014, **10**, 3145.

[31] D. Zhao, Q. Huo, J. Feng, B.F. Chmelka and G.D. Stucky, *J. Am. Chem. Soc.*, 1998, **120**, 6024.

[32] K. Mori, Y. Miura, S. Shironita and H. Yamashita, *Langmuir*, 2009, **25**, 11180.

[33] F. Liu, D. Wechsler and P. Zhang, *Chem. Phys. Lett.*, 2008, **461**, 254.

[34] K. Mori, K. Miyawaki, H. Yamashita, *ACS Catal.*, 2016, **6**, 3128.

[35] (a) J. Kang, T. Chen, D. Zhang and L. Guo, *Nano Energy*, 2016, **23**, 145. (b) M. Navlani-García, K. Mori, A. Nozaki, Y. Kuwahara and H. Yamashita, *Appl. Catal. A Gen.*, 2016, **527**, 45.

[36] W. Zhan, Q.-L. Zhu and Q. Xu, *ACS Catal.*, 2016, **6**, 6892.

[37] Q. Wang, Z. Liu, W. Wang, D. Liu, W. Shi, J. He, P. Shao, R. Shi and F. Cui, *Int. J. Hydrogen Energy*, 2016, **41**, 8470.

[38] P. Christopher, H. Xin and S. Linic, *Nat. Chem.*, 2011, **3**, 467.

[39] C. Burda, X. Chen, R. Narayanan and M. A. El-Sayed, *Chem. Rev.*, 2005, **105**, 1025.

[40] D.D. Evanoff and G. Chumanov, *ChemPhysChem*, 2005, 6, 1221.

[41] S. Trasatti, *Electroanal. Chem. Interfacial Electrochem.*, 1971, **33**, 351.

[42] Q. Xiao, S. Sarina, E. Jaatinen, J. Jia, D.P. Arnold, H. Liu and H. Zhu, *Green Chem.*, 2014, **16**, 4272.

Chapter V

Synthesis of Mesoporous Silica Supported Ag Nanorods-based Bimetallic Catalysts and Investigation of Their Plasmonic Activity under Visible Light Irradiation

5.1 Introduction

Nanophotonics has proven to be a powerful tool to proficiently convert solar power to chemical energy by manipulating and concentrating light at the nanoscale.[1-4] The metal dielectrics which can preserve surface and volume charge oscillations are called as surface plasmons.[5,6] They tend to exist in different forms i.e. surface plasmon polaritons and localized plasmons by propagating along flat interphases and within metal nanoparticles (NPs), respectively. The strong plasmonic field generated by these plasmons, decays by enhanced absorption (non-radiative), scattering (radiative) and localized heating, which has found its applications in enhanced Raman scattering,[7] photochemical reactions,[8] and photothermal therapy[9] processes, respectively. The non-radiative decay of plasmons through Landau damping[10] leads to the generation of hot electrons and hole pairs. These hot carriers play a very important role in the plasmonic photocatalysis by creating an oscillating dipole, which leads to electric field enhancements ($|E|^2$) of the order of 10^2 - 10^3, considering the case of isolated plasmonic nanostructures.[11] The hot spots are generated when metal nanostructures are in close proximity exhibiting an electric field enhancement of 10^6.[11,12]

Employing plasmonic metal nanostructures, which can emerge in a variety of forms depending on their size, shape, geometry and surrounding mediums, can lead to the improvement of the yield and selectivity of various heterogeneous catalytic reactions. It can be well documented by citing the examples of successful conversions in the commercial chemical production reactions. A 4-fold enhancement in the ethylene epoxidation reaction than the conventional process using Ag nanocubes[12] and an improvement in the selectivity of the propylene oxide by 20 % on utilizing plasmonic resonance effect of Cu are the few examples to demonstrate the importance of designing materials with visible light sensitivity.[13] An interesting study reported by El-Sayed *et al.* outlines the wavelength selective plasmonic activity of inner Au NPs in the azo dimer formation in comparison to the outer AuPt nanorattles.[14]

The pursuance of more practical artificial photosynthesis can be partially fulfilled by designing asymmetric NPs like rods,[15] cubes[16] or prisms[17] instead of symmetric shapes. A concentrated plasmonic field intensity and more than one plasmonic mode enable the greatest amount of light absorption in order to enhance the efficiency of solar spectrum utilization. Among the types of direct and indirect driven plasmon photocatalysis, our research group focuses mainly on the direct photocatalysis, where plasmonic metal nanostructures simultaneously act as the light harvesting and the catalytic component.

In continuation of my previous research studies on monometallic[18] or bimetallic plasmonic systems,[19] this chapter aims to study the research carried out with plasmonic Ag nanorods (NRs) in combination with other catalytic active metal NPs like Ru, Ni, Co and Pd supported on mesoporous silica. Mesoporous silica acts as a solid support with uniform hexagonal channels for designing the metal NPs with higher stability, conversion, yield and selectivity.[20] The quest of developing more and more active and visible light efficient catalytic systems motivated me to study the combination of various active metals of transition series. Significant efforts have already been made to study the plasmonic activities of Ag,[21] Au[22] and Cu[23] NPs, but the rare combination of Ni, Pd, Co and Ru with specially grown long Ag NRs has not been studied till now. Further, exploration of the plasmonic effect of Ag in combination with these active metals makes it an interesting study. Hydrogen production from ammonia borane (AB) was employed to compare the catalytic activities under dark and visible light irradiation. The reduction of 4-nitrophenol (NP) to 4-aminophenol (AP) utilizing AB as a mild reducing agent was also explored utilizing series of bimetallic catalysts.

5.2 Experimental

5.2.1 Materials

Tetraethyl orthosilicate ($(C_2H_5O)_4Si$)), hydrochloric acid (HCl), 1-hexanol ($C_6H_{13}OH$), acetone, silver nitrate ($AgNO_3$), $PdCl_2$, $NiCl_2$, $RuCl_3$ and $CoCl_3$, ethanol and p-Nitrophenol ($NO_2C_6H_4OH$) were purchased from Nacalai Tesque Inc. Triblock Pluronic P123® (Mw = 5800, $PEO_{20}PPO_{70}PEO_{20}$) and ammonia borane (NH_3BH_3) were obtained from Sigma-Aldrich Co. All chemicals were used as received without any further purification.

5.2.2 Synthesis of SBA-15

Mesoporous silica SBA-15 was synthesized according to the method reported in literature utilizing Pluronic P123® as a structure directing agent and tetraethyl orthosilicate (TEOS) as a silica source under acidic conditions (pH < 1).[24]

5.2.3 Synthesis of Ag/SBA-15 NR

The growth of Ag nanorods (1 wt %) within SBA-15 (0.396 g) was carried out by microwave-assisted alcohol reduction method.[18] At first, the silica support was ultrasonicated well with 1-hexanol (40 mL) for 30 min. Further, precursor $AgNO_3$ aqueous solution (100 mmol, 0.4 mL) was injected into the solution followed by Ar bubbling for 15 min. The resultant mixture was then exposed to microwave irradiation (500 W) for a period of 5 min. The solution was then filtered and dried in air at 80 ˚C. The obtained blue colored Ag nanorods (NR) catalyst was named as Ag/SBA-15 NR.

5.2.4 Synthesis of M/Ag/SBA-15

0.5 wt % of M on Ag/SBA-15 (M= Pd, Ni, Co, Ru) was synthesized by plasmon-mediated deposition[19] of second metal on Ag NRs under visible light irradiation. 0.1 g of Ag/SBA-15 NR was suspended and ultrasonicated in water (20 mL) until it becomes a clear solution. It was followed by bubbling Ar gas for a period of 30 min to ensure complete inert atmosphere. Subsequently, metal precursor solution viz. $PdCl_2$, $NiCl_2$, $RuCl_3$ and $CoCl_3$ aqueous solution was injected into the reaction mixture and irradiated with a Xe lamp (500 W; San-Ei Electric Co. Ltd. XEF-501S) with continuous stirring for 2 h. The M^{n+} ions were further reduced by employing 2 mL of 13.3 mM sodium borohydride ($NaBH_4$) aqueous solution as a reducing agent. The resultant mixture was centrifuged, washed with distilled water and dried at 80° C in vacuum overnight. The obtained catalysts was denoted as M/Ag/SBA-15 where M = Pd, Ni, Co and Ru.

5.2.5 Characterization

The overall characterization of the prepared support and catalysts was established by UV-vis, N_2 physisorption, transmission electron microscopy (TEM), and X-ray photoelectron spectroscopic (XPS) and extended X-ray absorption fine structure (EXAFS) analysis. Shimadzu UV-2450 spectrophotometer was used to collect the reflectance UV-vis spectra of powdered samples. $BaSO_4$ was used as a reference solid and the spectra were collected by employing Kubelka-Munk function. Brunauer–Emmett–Teller (BET) surface area measurement was performed by using a BEL-SORP max system (MicrotracBEL) at -196° C. Degassing of the samples was done in a vacuum at 200° C for 3 h in order to remove the adsorbed impurities. TEM micrographs were obtained with a Hitachi Hf-2000 FE-TEM equipped with Kevex energy-dispersive X-ray detector operated at 200 kV. ESCA-3400 electron spectrometer was used to characterize samples for X-ray photoelectron spectroscopy. Ag K-edge XAFS spectra were recorded by using a fluorescence-yield collection technique at the beam line 01B1 station with an attached Si (111) monochromator at SPring-8, JASRI, Harima, Japan (prop. No. 2014A1045, 2015A1149, 2016A1095 and 2016A1057).

5.2.6 AB dehydrogenation

The catalytic reaction of dehydrogenation of AB was carried out in an aqueous suspension of catalysts. Briefly, 20 mg of catalyst was dispersed in distilled water (5 mL) in a Pyrex vessel (32 mL), sealed with a rubber septum. After bubbling Ar gas for 30 min, AB (20 μmol) was injected through the rubber septum and stirred continuously under either dark conditions or photoirradiation (320 mW cm^{-2}). A 500 W Xenon lamp (San-Ei Electric Co. Ltd. XEF-501S) was used to carry out reactions under visible light irradiation. The amount of hydrogen in the gas phase was measured by using Shimadzu GC-14B gas chromatograph equipped with a TCD detector.

5.2.7 4-Nitrophenol (NP) reduction

The prepared catalysts were also investigated for the plasmonic activity in the reduction of 4-nitrophenol to 4-aminophenol. 5 mg of catalyst was suspended in 20 mL of 4-NP (0.4 mM) in a Pyrex glass tube. The solution was bubbled with Ar gas for 30 min, followed by addition of freshly prepared 0.5 mL of AB (0.05 M) through a rubber septum using a syringe. Reaction monitoring was done by extracting 3 mL of the suspension from the reaction mixture and measuring the intensity of the absorption band at 400 nm for 4-NP. The reaction was carried out in dark and under visible light irradiation and monitored by UV-vis spectrophotometer at given intervals of time.

5.3 Results and discussion

Designing elongated plasmonic nanostructures with uniform shape and narrow size distribution, exhibiting intense absorption in the visible region is still a great challenge. The ability to increase the absorption at higher wave numbers is the best way to increase the light harvesting efficiency. Since the absorption of NRs can be varied by changing their orientation under an applied electric field, they find their wide application in therapeutics,[25] plasmonic tunability,[26] thermal sensitivity,[27] light emitting devices,[28] chemical sensing[29] and so on. In order to characterize the absorption of prepared catalysts, surface plasmon resonance (SPR) property was investigated by diffuse reflectance UV-vis and NIR absorption spectroscopy. The optical response of as-prepared Ag/SBA-15 NR and 0.5 wt % of M (Ru, Pd, Co and Ni) on Ag/SBA-15 NRs are presented in Figure 1 (A). The two absorption peaks for Ag/SBA-15 NRs centered at visible (~ 370 nm) and infrared regions (~ 980 nm) are the optical signatures for the formation of nanorods. The transverse (T) and longitudinal (L) plasmonic resonance wavelengths of the mesoporous silica supported Ag NRs and bimetallic Ru/Ag, Pd/Ag, Co/Ag and Ni/Ag are (370, 980), (370, 990), (360, 1020), (372, 842) and (373, 994) nm, respectively, also mentioned in Table 1.

Table 1. Textural properties, length of NRs and LSPR absorption for prepared catalysts.

Catalyst	**Surface area (m^2/g)**	**Total pore volume (cm^3/g)**	**Pore size (nm)**	**LSPR λ of NRs (T, L) (nm)**
SBA-15	698	0.76	5.7	N/A
Ag/SBA-15 NR	539	0.63	5.8	(370, 980)
Pd/Ag/SBA-15	433	0.63	6.1	(360, 1020)
Ru/Ag/SBA-15	391	0.62	6.8	(370, 990)
Ni/Ag/SBA-15	425	0.66	6.8	(373, 994)
Co/Ag/SBA-15	440	0.59	7.2	(372, 842)

Taking into account the fact that the SPR absorption is sensitive to particle size, shape, distribution and the surrounding medium, the slight shift towards high and low wavenumbers can be attributed to the increased and decreased aspect ratio of NRs, respectively. The intensity corresponding to the transverse mode decreased slightly giving us the evidence of surface coverage by the introduction of a second metal on Ag NRs. However, the significant variations in the longitudinal mode absorption following the order of Pd/Ag > Ag > Ru/Ag > Co/Ag > Ni/Ag, correlate with the enhancements observed under visible light irradiation in the catalytic reactions, as explained in later section. The simple illustration for the preparation of bimetallic NRs by LSPR-mediated process followed by $NaBH_4$ reduction, is shown in Figure 1 (B).

Figure 2 (A) represents the high-resolution TEM image of Ag NRs grown within the channels of SBA-15, Fig. 2 (B) shows the high angle annular dark field (HAADF)-STEM image showing contrast image of the NRs. Figure 2C and 2D summarize the mapping results of the Ag deposited on the silica surface. The estimated length of Ag NR from TEM micrographs was found out to be 30 nm. The bimetallic M/Ag NRs TEM images are shown in Figure 3.

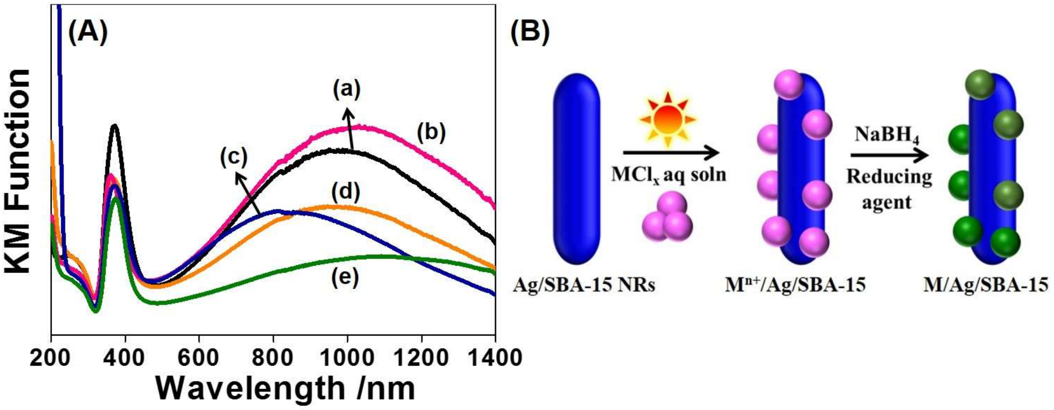

Figure 1. (A) UV-vis spectra of (a) Ag/SBA-15 NR, (b) Pd/Ag/SBA-15, (c) Co/Ag/SBA-15, (d)Ru/Ag/SBA-15 and (e) Ni/Ag/SBA-15 (B) Schematic illustration of M/Ag/SBA-15 synthesis by LSPR assisted method followed by chemical reduction.

It can be seen that after incorporation of a second metal NPs, the rod-like morphology of Ag remains intact. The NRs became a little longer with an average estimated length for Ru/Ag/SBA-15, Pd/Ag/SBA-15, Co/Ag/SBA-15 and Ni/Ag/SBA-15 of 40, 30, 48 and 43 nm, respectively. Also, from the micrographs in Figure 2 and 3, it can be observed that the growth of NRs occurred within the hexagonal channels of SBA-15 mesoporous silica showing narrow size distribution, which was further confirmed by the BJH mesoporous volume analysis, as discussed later. A HR-TEM image of Ru/Ag/SBA-15 is also shown in Figure 4 along with the mapping of Ru and Ag. From the micrographs, I concluded that the second metal is distributed over the entire surface of silica in the form of metallic clusters. The effective ones are those in the vicinity of Ag NRs for efficient plasmonic catalysis under visible light irradiation.

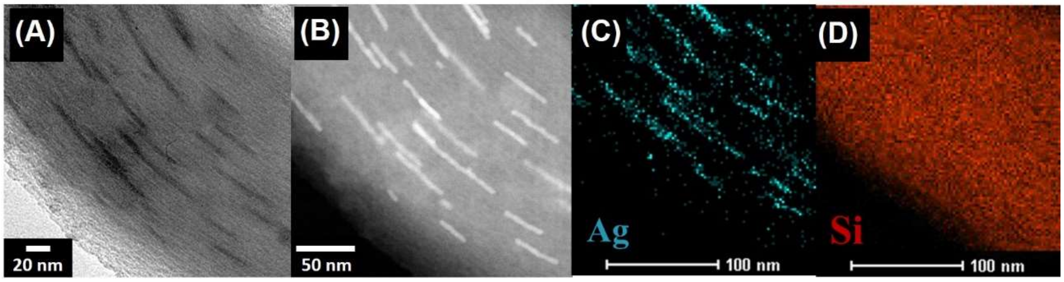

Figure 2. (A) HR-TEM (B) HAADF-STEM images of Ag/SBA-15 NR and (C, D) elemental mapping representing silver and silicon in Ag/SBA-15 NRs, respectively.

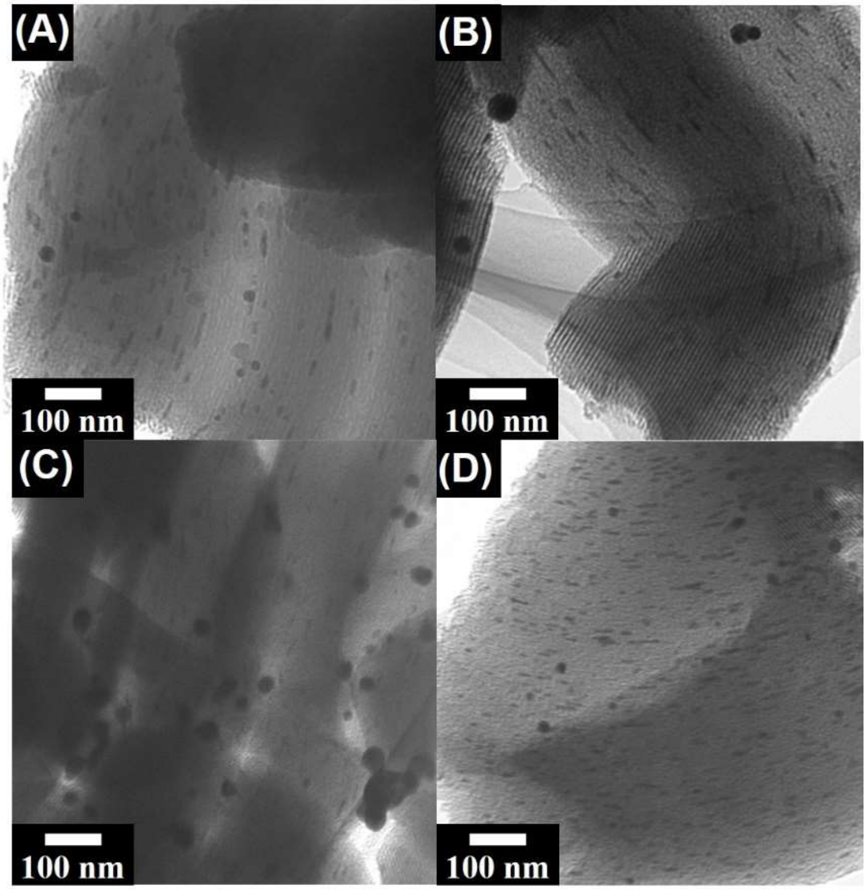

Figure 3. TEM images of the bimetallic Ag NRs (A) Pd/Ag/SBA-15 (B) Ru/Ag/SBA-15 (C) Ni/Ag/SBA-15 and (D) Co/Ag/SBA-15.

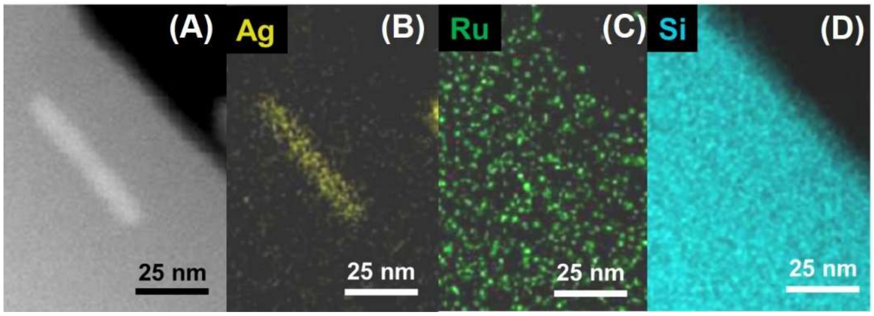

Figure 4. (A) HR-STEM image for Ru/Ag/SBA-15 and Elemental mapping of (B) Ag (C) Ru and (D) Si.

The N_2 adsorption-desorption measurements were carried out to determine specific surface area, pore volume and pore size of prepared catalysts as summarized in Table 1 and Figure 5. A typical type IV isotherm with an H1-type hysteresis loop showing sharp inflection at a relative pressure range of 0.7 confirms the preservation of mesoporous structure and existence of hexagonal cylindrical channels in all catalysts. The BET surface area of Ag NRs deposited on SBA-15 was found to be 539 m^2/g with pore size and pore volume of 5.84 nm and 0.63 cm^3/g, respectively.

The decrease in the surface area was observed with second metal incorporation (Pd, Ru, Ni and Co) on the surface of Ag NRs. The pore volume showed almost constant values for all the catalysts whereas, in the case of pore size distribution, an increment was observed from 5.7 (SBA-15) to 7.2 nm in Co/Ag/SBA-15. This can be explained due to the excessive particle growth of second metal on Ag by two possible mechanisms viz. particle migration and Ostwald ripening. The growth of NPs leads to the wall deformation and hence overall increment in the pore size values. A major distortion can also be observed in the hysteresis curve of Co/Ag/SBA-15 isotherm. All Catalysts sustained the high surface area and type-IV isotherms, hence showing the high dispersity of NRs within the mesopores of SBA-15.

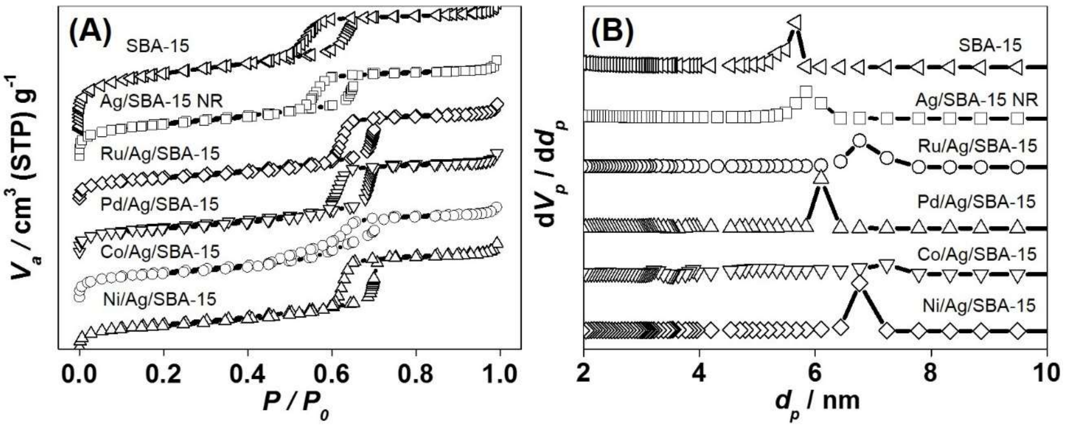

Figure 5. (A) N_2 adsorption-desorption isotherms and (B) pore size distribution for prepared catalysts.

Extended X-ray absorption fine structure (EXAFS) measurement studies were carried out to elucidate the local structure of NPs supported on mesoporous silica. Figure 6 (A) shows the Ag K-edge Fourier transforms (FT) EXAFS spectra for Ag NRs and M/Ag bimetallic catalysts along with standard samples including Ag foil and Ag oxide (AgO). All samples exhibited an intense peak at 2.7 Å attributed to the contiguous Ag-Ag metallic bonding, similar to that of Ag foil. This confirms the presence of Ag^0 species in Ag NRs and bimetallic M/Ag samples. The recognizable different peak at approximately 1.9 Å for AgO represents Ag-O-Ag bonding. Figure 6 (B) summarizes the X-ray photoelectron spectroscopy (XPS) measurement spectra for Ag/SBA-15 NR, Co/Ag/SBA-15, Pd/Ag/SBA-15, Ru/Ag/SBA-15 and Ni/Ag/SBA-15, to characterize the surface composition and chemical state of prepared samples. The Ag 3d core level spectrum representing two strong peaks due to the splitting of 3d doublet by 6.0 eV confirms the metallic nature of Ag in all samples. The peaks observed at binding energies of 374.7 eV and 368.7 eV are ascribed to $3d_{3/2}$ and $3d_{5/2}$ core levels of Ag in Ag/SBA-15 NR, respectively. The shift in the binding energy of Ni/Ag and Co/Ag towards lower values and Ru/Ag and Pd/Ag towards higher values was observed in comparison to the monometallic Ag NRs. The integration of Ag with Ru and Pd induces the charge transfer from Ag atoms owing to the net difference in electronegativity (Ag: 1.93 and Ru, Pd: 2.20), while opposite charge transfer occurs towards Ag because of larger electronegativity of Ag than Ni (1.91) and Co (1.88). Thus XPS proves to be a strong evidence to display the existence of bimetallic interaction via electron transfer mechanisms situated adjacent to each other.

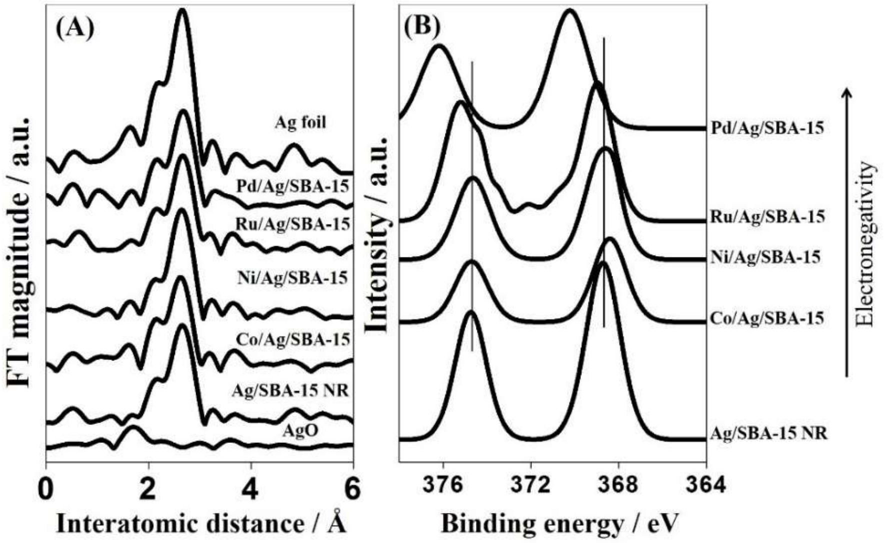

Figure 6. (A) FT-EXAFS of Ag k-edge and (B) XPS Ag 3d spectra for prepared catalysts.

Plasmonic catalysis in AB dehydrogenation

Ammonia borane (NH_3BH_3, AB) is considered to be an intriguing hydrogen carrier because of their high hydrogen capacity (19.6 wt %), low molecular weight (30.87 g mol^{-1}), easy storage and transportation due to its excellent stability in solid and aqueous solutions at room temperature.[30] The hydrolysis reaction of AB releases 3 mol of H_2 per mol of AB consumed in the presence of an appropriate catalyst as shown in equation (1).[31]

$$NH_3BH_3 + 2H_2O \rightarrow NH_4^+ + BO_2^- + 3H_2 \qquad (1)$$

Currently various combinations of noble and non-noble metal catalysts have been explored and acknowledged for their superior catalytic activities, i.e. Ru,[32] RuNi,[32] PdAg,[19] CoPd,[33] MoO_{3-x},[34] Pd/MoO_{3-x},[35] Fe(pincer) complex,[36] Pd@MIL-101,[37] OsH_2 complex[38] and so on. However, the rare combination of Ag NRs along with a bimetallic combination of Ru, Pd, Ni and Co has not been much explored. In an attempt to design visible and near-infrared active catalyst, these bimetallic nanorods were used as a catalyst to carry out the dehydrogenation reaction at room temperature.

All prepared catalysts exhibited H_2 production activity from AB aqueous solution under inert atmosphere (Ar) at room temperature in dark conditions as shown in Figure 7 (A). No H_2

was produced in the blank test without adding the catalyst and no induction period was observed in the stoichiometric (H_2 /AB = 3/1) H_2 production. Among all catalysts, Ag NRs displayed the least amount of H_2 and the catalytic activity decreased in the following order RuAg > NiAg > CoAg > PdAg > Ag. This might be due to the inherent property and the chemical nature of the metal introduced onto Ag NRs. The high catalytic activity can be attributed to the synergistic effect originating from the integration of Ru and Ag NRs.

To study the Ag-LSPR effect for developing more efficient catalyst, the reaction was carried out under visible light irradiation (λ > 420 nm) using a Xe lamp. As shown in Figure 7 (B), the catalytic performance of all catalysts was significantly enhanced in the following order: RuAg > NiAg > CoAg > PdAg > Ag. Enhancement factor (R_L/R_D) was calculated to study the differences in the rate of the reaction in dark and light condition by the simple division of reaction rate under light (R_L) and dark (R_D) conditions. The enhancement factor (values in parentheses) follows the order of PdAg (1.84) > Ag (1.53) > RuAg (1.34) > CoAg (1.22) > NiAg (1.01). The enhancement order was found to be in agreement of the absorption intensity of the longitudinal mode of the NRs as observed by UV-vis spectroscopy.

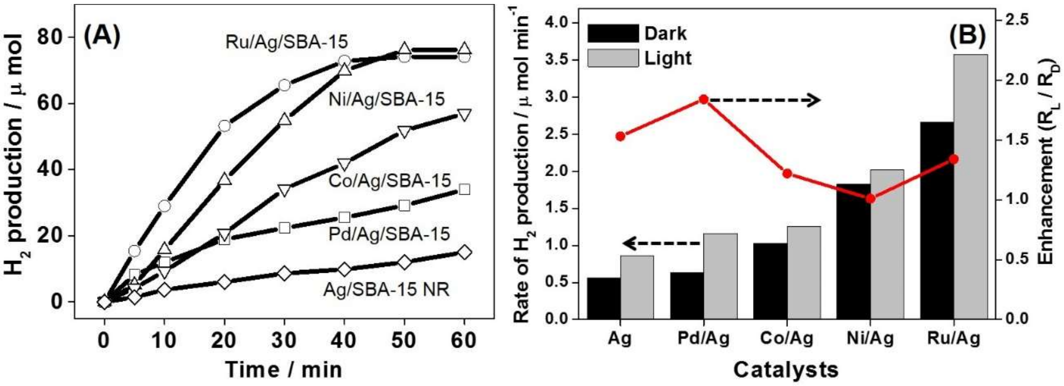

Figure 7. (A) Time course of H_2 production from AB over prepared catalysts under dark condition. (B) Reaction rate comparison and their corresponding enhancements under visible light irradiation. Reaction conditions: catalyst (20 mg), water (5 mL), Xe lamp (500 W) and AB (20 μmol) at room temperature.

To study the effect of loading amount of second metal, the weight percentage (wt %) loading of Ru was varied as follows: 0.0, 0.25, 0.5 and 1.0 wt % on Ag NRs (1.0 wt % on silica). It was found out that the catalytic activity increased on increasing the loading amount of Ru in both dark and light irradiation conditions as shown in Figure 8 (A). However, 0.5 wt % was found out to be the optimum ratio in terms of reaction rate and enhancement factor (R_L/R_D) calculations. This might be due to the maximum possible surface contact between the two metals, increasing beyond that affects the surface coverage of Ag and hence decreasing the enhancement under visible light irradiation conditions.

The stability of the most efficient and active catalyst Ru/Ag/SBA-15 was investigated by carrying out recycling experiments in dark and under light irradiation conditions. After each cycle, the system was purged with argon gas, followed by AB (20 µmol) injection and subsequently, monitoring the activity by GC. As shown in Figure 8 (B), consistent performance was observed even after 4th cycle under visible light irradiation condition, thus displaying remarkable stability and durability of the prepared catalyst.

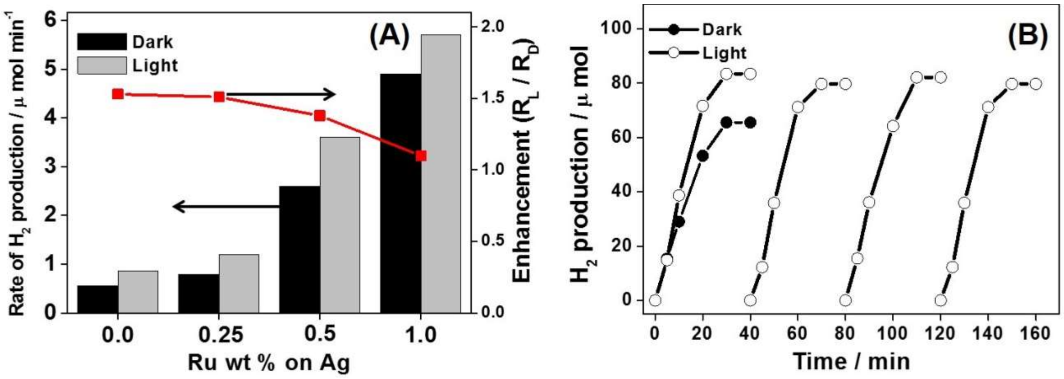

Figure 8. (A) Reaction rate and enhancements for AB dehydrogenation reaction over different weight percentage of Ru on Ag/SBA-15 NR, (B) Recyclability test for hydrogen production from AB over Ru/Ag/SBA-15 under dark and visible light irradiation.

Plasmonic catalysis in NP reduction

Nitrophenols are one of the most common organic pollutants found in industrial and agricultural wastewaters whereas aminophenol (4-AP) is an important intermediate for the large scale synthesis of analgesic, antipyretic drugs, dye, polymer and natural products.[39] Till date, many processes have been developed for the treatment of 4-NP such as oxidation, degradation, adsorption, and coagulation. Similarly, 4-AP can be synthesized by various methods like iron-acid reduction of nitrochlorobenzenes or catalytic hydrogenation of 4-NP in an acidic medium.

However, both methods face the drawbacks of iron sludge disposal and usage of corrosive acids. To overcome the disadvantages, an efficient and greener route can be employed for the chemical reduction of 4-NP to 4-AP. In this study, the reaction is catalysed by Ag and M/Ag nanorods in which NPs serve a dual role to catalyse the dehydrogenation of AB and hydrogenation of 4-NP. AB was used as a convenient H_2 source instead of conventional $NaBH_4$ because of the high stability and non-toxic property of AB.[40]

The presence of 4-NP can be detected by UV-vis spectroscopy, in which it shows a strong absorption peak at 317 nm in aqueous solution. The appearance of a new peak at 400 nm upon addition of AB is attributed to the formation of 4-NP anions by H^+ dissociation from 4-NP in basic AB solution. The reaction kinetics were monitored by the decreasing absorption peak intensity of 4-NP anions at 400 nm in the presence of Ag catalyst. The process is also accompanied by the appearance of a new peak at 296 nm assigned to the 4-aminophenol. Figure 9 (A) shows the reaction kinetic plot of $\ln(C/C_0)$ vs. time, where C and C_0 signify the concentration of 4-NP at time t and t_0, respectively. The rate constants under dark conditions follow the order of RuAg > NiAg > CoAg > PdAg > Ag in the presence of sufficient amount of AB acting as a mild reducing agent. The dehydrogenation of AB and hydrogenation of 4-NP to 4-AP apparently take place on the surface of both the NPs. The increased rate is attributed to the inherent property of the second metal incorporation and the synergistic bonding existing between the bimetals.

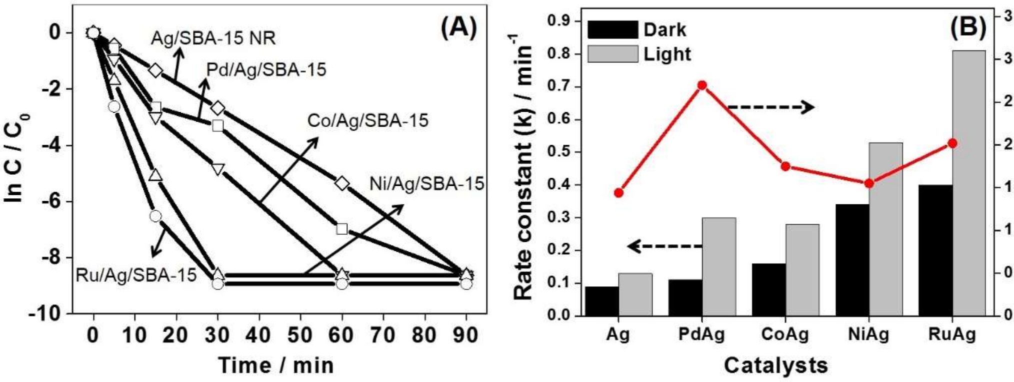

Figure 9. (A) Time course plot of 4-NP reduction to 4-AP under dark conditions. (B) Reaction rate constant comparison and their corresponding enhancements under visible light irradiation. Reaction conditions: catalyst (5 mg), water (20 mL), 4-NP (0.4 mM), Xe lamp (500 W) and AB (0.5 mL, 0.05 M) at room temperature.

On irradiating with visible light irradiation, all rate constants of the reaction was found to be enhanced with their rate constants following the order of RuAg > NiAg > PdAg > CoAg > Ag. Enhancement factor (k_L/k_D) was calculated to study the differences in the rate of the reaction in dark and light condition by the simple division of rate constant values under light (k_L) and dark (k_D) conditions. The enhancement factor (values in parentheses) follows the order of PdAg (2.7) > RuAg (2.02) > CoAg (1.75) > NiAg (1.55) > Ag (1.44). The enhancement order was dependent on the absorption intensity of the longitudinal mode of the NRs (among bimetals only) as observed by UV-vis spectroscopy. The catalytic activity enhancement in the reduction of 4-NP is almost consistent with that observed in the AB dehydrogenation (Figure 8B vs. Figure 9B), thus indicating that the dehydrogenation of AB may be the rate-determining step in the tandem reaction.

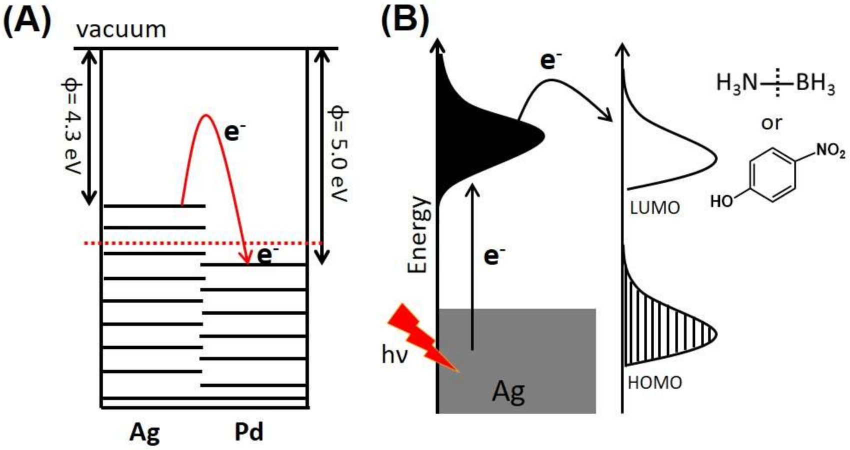

Figure 10. (A) Work function and fermi energy level distribution of Ag and Pd NPs. (B) Photo-excited plasmonic states of Ag NRs transferring electrons to the adsorbate molecules.

The early mechanistic studies on plasmonic catalysis were proposed by Tatsuma *et al.* in 2004 to explain the enhanced photocatalytic activities under visible light irradiation.[41] Under irradiation conditions, the excited hot electrons transfer to the available adsorbate orbitals to form a transient negative ion (TNI), which reacts on the surface of metal.[42] The work function value of Ag (4.3 eV) is considerably lower than that of Pd (5.0 eV), Ru (4.8 eV), Ni (4.7 eV) and Co (4.7 eV), which makes the positioning of their fermi energy levels lower than to Ag as shown in Figure 10.[43,44] Hence, the electron transfer from Ag to the second metal is quite feasible. The photo-excited plasmonic states of the Ag transfer energy to the unoccupied adsorbate (reactant) states, leading to the bond weakening and hence cleavage of reactants to products.[45] An important characteristic of utilizing solely the plasmonic metal nanostructures is their high reaction rates due to the effective coupling of light harvesting and catalytic activity, unlike semiconductor materials. Furthermore, the electric field enhancements in metal NPs near their resonance frequencies can lead to as much as 1000 times by generating hot spots, in comparison to the incident electromagnetic field.

5.4 Conclusions

In summary, I have synthesized silver nanorods supported on mesoporous silica by a single step microwave-assisted alcohol reduction method. The bimetallic catalysts M/Ag/SBA-15, deposited by LSPR assisted method followed by $NaBH_4$ reduction, were successfully synthesized and explored for their plasmonic catalytic activity in dark or under light irradiation conditions. Ru/Ag/SBA-15 displayed most active catalytic performance in dark or under light irradiation for AB dehydrogenation (2.6 and 3.6 μmol min^{-1}) and 4-NP reduction (0.8 and 2.0 min^{-1}), whereas Pd/Ag/SBA-15 exhibited maximum enhancement effects for efficient hydrogen production from AB ($R_L/R_D = 1.84$) and chemical reduction of 4-NP ($k_L/k_D = 2.7$). The remarkable enhancement and catalytic activity were attributed to the synergistic bonding of Ag with Ru, Pd, Ni, Co and their light absorption intensity in the UV-vis spectroscopy. In addition, Ru/Ag/SBA-15 showed high stability for the hydrogen production from AB up to four consecutive runs. The present study includes series of catalytic system explored for AB hydrolysis in hydrogen storage application. It is reasonable to expect that plasmonic photocatalysis will play more important roles in near future including energy and environmental applications in air cleaning, water splitting, and CO_2 reduction, which can play a significant role in serving the society. Till date, the research conducted on plasmonic nanostructures has illustrated to be one of the most promising materials for solar to chemical energy conversion. They will definitely prove to be the building blocks in the design and synthesis of composite photocatalyst materials in the near future. Furthermore, major advancements are needed in their mechanistic pathway, theoretical predictive models (FDTD simulations) and new synthetic strategies. We hope that this work can help and contribute a bit in the understanding and application of the phenomenon.

5.5 References

[1] J.A. Schuller, E.S. Barnard, W. Cai, Y.C. Jun, J.S. White and M. L. Brongersma, *Nat. Mater.*, 2010, **9**, 193.

[2] A. F. Koenderink, A. Alù and A. Polman, *Science*, 2015, **348**, 516.

[3] D. K. Gramotnev and S. I. Bozhevolnyi, *Nat. Photonics*, 2010, **4**, 83.

[4] G. Chen, H. Ågren, T. Y. Ohulchanskyy and P. N. Prasad, *Chem. Soc. Rev.*, 2015, **44**, 1680.

[5] W. L. Barnes, A. Dereux and T. W. Ebbesen, *Nature*, 2003, **424**, 824.

[6] P. Nordlander and E. Prodan, *Nano Lett.*, 2004, **4**, 2209.

[7] a) J. B. Jackson and N. J. Halas, *Proc. Natl. Acad. Sci. U. S. A.*, 2004, **101**, 17930; b)R. Zhang, Y. Zhang, Z. C. Dong, S. Jiang, C. Zhang, L. G. Chen, L. Zhang, Y. Liao, J. Aizpurua, Y. Luo, J. L. Yang and J. G. Hou, *Nature*, 2013, **498**, 82.

[8] a) M. Xiao, R. Jiang, F. Wang, C. Fang, J. Wang and J. C. Yu, *J. Mater. Chem. A*, 2013, **1**, 5790; b) W. Hou and S. B. Cronin, *Adv. Funct. Mater.*, 2013, **23**, 1612.

[9] a) D. Pissuwan, S. M. Valenzuela and M. B. Cortie, *Trends Biotechnol.*, 2006, **24**, 62; b) X. Ding, C. H. Liow, M. Zhang, R. Huang, C. Li, H. Shen, M. Liu, Y. Zou, N. Gao, Z. Zhang, Y. Li, Q. Wang, S. Li and J. Jiang, *J. Am. Chem. Soc.*, 2014, **136**, 15684.

[10] X. Li, D. Xiao and Z. Zhang, *New J. Phys.*, 2013, **15**, 023011.

[11] D. B. Ingram, P. Christopher, J. L. Bauer and S. Linic, *ACS Catal.*, 2011, **1**, 1441.

[12] P. Christopher, H. Xin and S. Linic, *Nat. Chem.*, 2011, **3**, 467.

[13] A. Marimuthu, J. Zhang and S. Linic, *Science*, 2013, **339**, 1590.

[14] M. A. Mahmoud, B. Garlyyev and M. A. El-Sayed, *J. Phys. Chem. C*, 2015, **119**, 18618.

[15] H. Chen, L. Shao, Q. Li and J. Wang, *Chem. Soc. Rev.*, 2013, **42**, 2679.

[16] Q. Yang, Q. Xu, S. H. Yu and H. L. Jiang, *Angew. Chem. Int. Ed.*, 2016, **128**, 3749.

[17] a)X. Yang, Y. Yu and Z. Gao, *ACS Nano*, 2014, **8**, 4902–4907; b) L. Brus, *Nat. Mater.*, 2016, **15**, 824.

[18] a) K. Fuku, R. Hayashi, S. Takakura, T. Kamegawa, K. Mori and H. Yamashita, *Angew. Chem. Int. Ed.*, 2013, **52**, 7446; b) K. Mori, P. Verma, R. Hayashi, K. Fuku

and H. Yamashita, *Chem. Eur. J.*, 2015, **21**, 11885; c) P. Verma, Y. Kuwahara, K. Mori and H. Yamashita, *Chem. Eur. J.*, 2017, **23**, 3616.

[19] a) P. Verma, Y. Kuwahara, K. Mori and H. Yamashita, *J. Mater. Chem. A*, 2015, **3**, 18889–18897; b) P. Verma, Y. Kuwahara, K. Mori and H. Yamashita, *J. Mater. Chem. A*, 2016, **4**, 10142.

[20] R. J. White, R. Luque, V.L. Budarin, J.H. Clark and D.J. Macquarrie, *Chem. Soc. Rev.*, 2009, **38**, 481.

[21] a) C. Y. Li, M. Meng, S. C. Huang, L. Li, S. R. Huang, S. Chen, L. Y. Meng, R. Panneerselvam, S. J. Zhang, B. Ren, Z. L. Yang, J. F. Li and Z. Q. Tian, *J. Am. Chem. Soc.*, 2015, **137**, 13784; b) P. Yang, J. Zheng, Y. Xu, Q. Zhang and L. Jiang, *Adv. Mater.*, 2016, 28, 10508; c) R. Asapu, N. Claes, S. Bals, S. Denys, C. Detavernier, S. Lenaerts and S. W. Verbruggen, *Appl. Catal. B Environ.*, 2017, **200**, 31.

[22] a) S. Rodal-Cedeira, V. Montes-García, L. Polavarapu, D. M. Solís, H. Heidari, A. La Porta, M. Angiola, A. Martucci, J. M. Taboada, F. Obelleiro, S. Bals, J. Pérez-Juste and I. Pastoriza-Santos, *Chem. Mater.*, 2016, **28**, 9169; b) R. He, Y. C. Wang, X. Wang, Z. Wang, G. Liu, W. Zhou, L. Wen, Q. Li, X. Wang, X. Chen, J. Zeng and J. G. Hou, *Nat. Commun.*, 2014, **5**, 4327.

[23] a) E. Kazuma, T. Yamaguchi, N. Sakai and T. Tatsuma, *Nanoscale*, 2011, **3**, 3641; b) Qi-C. Sun, Y. Ding, S. M. Goodman, H. H. Funke and P. Nagpal, *Nanoscale*, 2014, **6**, 12450.

[24] D. Zhao, J. Feng, Q. Huo, N. Melosh, G.H. Fredrickson, B.F. Chmelka and G.D. Stucky, *Science*, 1998, **279**, 548.

[25] A. M. Alkilany, L. B. Thompson, S. P. Boulos, P. N. Sisco and C. J. Murphy, *Adv. Drug Deliv. Rev.*, 2012, **64**, 190.

[26] B. Pietrobon, M. McEachran and V. Kitaev, *ACS Nano*, 2009, **3**, 21.

[27] P. K. Jain, X. Huang, I. H. El-Sayed and M. A. El-Sayed, *Acc. Chem. Res.*, 2008, **41**, 1578.

[28] a) P. A. Hobson, S. Wedge, J. A. E. Wasey, I. Sage and W. L. Barnes, *Adv. Mater.*, 2002, **14**, 1393; b) X. Gu, T. Qiu, W. Zhang and P. K. Chu, *Nanoscale Res. Lett.*, 2011, **6**, 199.

[29] K. S. Lee and M. A. El-Sayed, *J. Phys. Chem. B*, 2006, **110**, 19220.

[30] A. Gutowska, L. Li, Y. Shin, C. M. Wang, X. S. Li, J. C. Linehan, R. S. Smith, B. D. Kay, B. Schmid, W. Shaw, M. Gutowski and T. Autrey, *Angew. Chem. Int. Ed.*, 2005, **44**, 3578.

[31] M. Chandra and Q. Xu, *J. Power Sources*, 2006, **156**, 190.

[32] K. Mori, K. Miyawaki and H. Yamashita, *ACS Catal.*, 2016, **6**, 3128.

[33] H. Göksu, H. Can, K. Sendil, M. S. Gultekin and O. Metin, *Appl. Catal. A Gen.*, 2014, **488**, 176.

[34] H. Cheng, T. Kamegawa, K. Mori and H. Yamashita, *Angew. Chem. Int. Ed.*, 2014, **53**, 2910.

[35] H. Cheng, X. Qian, Y. Kuwahara, K. Mori and H. Yamashita, *Adv. Mater.*, 2015, **27**, 4616.

[36] P. Bhattacharya, J. A. Krause and H. Guan, *J. Am. Chem. Soc.*, 2014, **136**, 11153.

[37] Q. Yang, Y.-Z. Chen, Z. U. Wang, Q. Xu and H.-L. Jiang, *Chem. Commun.*, 2015, **51**, 10419.

[38] M. A. Esteruelas, A. M. López, M. Mora and E. Oñate, *ACS Catal.*, 2015, **5**, 187.

[39] a) A. M. Tafesh and J. Weiguny, *Chem. Rev.*, 1996, **96**, 2035; b) H. Cheng, M. Wen, X. Ma, Y. Kuwahara, K. Mori, Y. Dai, B. Huang and H. Yamashita, *J. Am. Chem. Soc.*, 2016, **138**, 9316.

[40] a) X. Wang, D. Liu, S. Song and H. Zhang, *J. Am. Chem. Soc.*, 2013, **135**, 15864; b) H. Göksu, S. F. Ho, Ö. Metin, K. Korkmaz, A. Mendoza Garcia, M. S. Gültekin and S. Sun, *ACS Catal.*, 2014, **4**, 1777; c)

Chapter VI

Pd/Ag and Pd/Au Bimetallic Nanocatalysts on Mesoporous Silica for Plasmon-mediated Enhanced Catalytic Activity under Visible Light Irradiation

6.1 Introduction

The collective oscillation of conduction electrons of noble metals, which gives rise to strongly concentrated intensities of electric field, are generally called as localized surface plasmon resonance (LSPR).[1,2] The plasmon induced field intensity shows maxima at the surface while decays exponentially on going away from the surface. The wavelength and intensity of LSPR depends strongly on the nature of metal, size and morphology of nanostructures. The variation in the morphology of the nanostructures also changes the number of LSPR peaks accounting for their polarization modes due to different geometrical symmetries. The plasma frequency (ω_p) can be varied depending on the metal carrier concentration (N), as shown in equation 1, where m_{eff} is the effective mass of carriers and e is the electronic charge.

$$\omega_p = \sqrt{\frac{Ne^2}{\varepsilon_0 m_{eff}}} \quad (1)$$

However, N is fixed of the order of 10^{23} cm^{-3}, while this concept can be applied to tunability for semiconductor plasmons.[3]

Plasmon enhanced photocatalytic reactions can be grouped into two categories; i) a combination of metal and semiconductor, where reaction usually takes place on the surface of semiconductor and the metal NPs helps in enhancing the absorption of light intensity[16,18], ii) pure metal plasmonic catalysis (Ag, Au or Cu), where reaction is controlled truly and wholly by the metal NPs.[17] Both types have their own significance, however the group ii) can dominate in terms of single site catalysis and higher photon efficiency. The plasmonic catalysis based on the pure metal nanostructures can be classified into two mechanisms including plasmonic heating and hot electron transfer. Plasmonic heating arises due to decay of LSPR by electron-photon relaxation. Hot electron transfer can be understood in terms of sensitization. The hot electrons generated upon light irradiation are usually transferred into the lowest unoccupied molecular orbital (LUMO) leading to the weakening of chemical bonds and thus increasing the rate of reaction. However, at present, it is difficult to prove and provide evidence for the occurrence of either mechanism. Understanding the stepwise mechanism caused by the metal NPs is quite challenging. Among most commonly encountered plasmonic metals (e.g. Ag, Au or Cu), Au is found to be more suitable for plasmonic catalysis because of its atmospheric stability and resistance towards oxygen.

These plasmonic nanostructures are now recently being studied in combination with other plasmonic or catalytically active metals in order to improve the optical and/or catalytic activity and selectivity.[4] Bimetallic nanostructures are continuously being explored for their distinctive advantages over monometallic nanostructures because of their additional diversity in the choice of composition and structure.[14] Various bimetallic nanostructures have been synthesized in the recent past with variety of structures including core-shell, alloy, nanowires, dendrite, three-component systems and so on.[58-61] A plethora of synthetic approaches have been developed to synthesize these bimetallic nanostructures, such as wet chemical, photochemical, microwave, electrochemical or so on.[5-8] Their composition and morphology can play remarkable role in various fields of technologies including optical sensing,[9,15] surface enhanced Raman scattering (SERS), solar cells, photonics and nanobio detection/sensing.[10-13] Much effort has already been formulated in the development of new techniques to synthesize bimetallic nanostructures. Hence, novel plasmonic bimetallic nanostructures need to be developed for the continuous advancement in the field of plasmonics.

In this chapter, I have developed Pd/M (M=Ag, Au) based plasmonic bimetallic nanocatalyst supported on SBA-15 mesoporous silica. A detailed and systematic study has been done in order to study the superior plasmonic properties as well as catalytic performances of Pd/M bimetallic nanocatalysts than monometallic M/SBA-15 catalysts. Suzuki coupling and hydrolytic dehydrogenation of ammonia borane (AB) for hydrogen production were selected as a model reactions to study the plasmonic catalytic activities and explore the wide applicability of the prepared catalysts. It is demonstrated that the localized surface plasmon charge of Pd/M NPs enhances the catalytic activity to a greater extent than monometallic NPs under visible light irradiation.

6.2 Experimental

6.2.1 Materials

Tetraethyl orthosilicate ($(C_2H_5O)_4Si$)), hydrochloric acid (HCl), 1-hexanol ($C_6H_{13}OH$), ethylene glycol ($C_2H_6O_2$), acetone, silver nitrate ($AgNO_3$), hydrogen tetrachloroaurate ($HAuCl_4.4H_2O$), sodium laurate, iodobenzene (C_6H_5I), bromobenzene (C_6H_5Br), chlorobenzene (C_6H_5Cl), palladium (II) acetate ($Pd(OAc)_2$) and ethanol were purchased from Nacalai Tesque Inc. Triblock pluronic P123® ($M_w = 5800$, $PEO_{20}PPO_{70}PEO_{20}$) and ammonia borane (NH_3BH_3) were obtained from Sigma-Aldrich Co. Phenylboronic acid was bought from Tokyo Chemical Industries Co. Ltd. All chemicals were used as received without any further purification.

6.2.2 Preparation of SBA-15

SBA-15 was synthesized as per method reported in literature, using Pluronic P123® as a structure directing agent and tetraethyl orthosilicate as a silica source under acidic conditions ($pH < 1$). Briefly, P123 was dissolved in 0.1 N HCl with continuous stirring at 40° C for 2 h at 400 rpm. After assurance of uniform dispersion, TEOS was slowly added to the reaction mixture under vigorous stirring at 40° C and was continuously stirred for 24 h. The obtained mixture was transferred to the Teflon bottle followed by aging at 80° C for 24 h. The white suspension was then filtered, washed with ample amounts of deionized water and dried at 80° C overnight. Finally, calcination at 550° C was done for a period of 5 h in order to ensure the complete removal of the organic templates used during the synthesis.

6.2.3 Preparation of Au/SBA-15

1 wt % of Au was incorporated on SBA-15 by the Microwave polyol method using ethylene glycol as a solvent and reducing agent. 0.1 g of SBA-15 was well dispersed in ethylene glycol (40 ml) by continuous stirring and ultrasonication. Uniform and complete dispersion of the support and metal precursor solution is an important step in the synthesis. After complete dispersion, 600 μL of $HAuCl_4$ (9.62 mM) solution was injected onto the reaction solution, followed by argon gas bubbling for 15 minutes. Subsequently, the reaction mixture was exposed to continuous wave MW irradiation (500 W, 2450 ± 30 MHz) for a period of 3 min. The yellowish-orange transparent solution first changed to colorless followed by pink indicating the formation of reduced Au NPs. The resultant product was filtered and washed well with distilled water and acetone followed by drying at 80° C in air overnight. The obtained sample was named as Au/SBA-15.

6.2.4 Preparation of Ag/SBA-15

The incorporation of 1 wt % Ag onto mesoporous silica was also done in a similar way with a little modification. At first, the SBA-15 mesoporous silica support was well dispersed into the solvent. In this case, 1-hexanol served as the solvent and reducing agent. Again the complete dispersion of the support was ensured followed by the addition of sodium laurate (surface ligand) and precursor $AgNO_3$ aqueous solution. The inert atmosphere conditions were maintained by flowing Ar gas through the reaction mixture followed by MW heating (500 W, 2450 ± 30 MHz) for 3 minutes. The colorless solution changed to bright yellow after heating, confirming the formation of reduced metal NPs. The obtained solid was filtered with lots of water and dried overnight in air at 80 ˚C. The obtained solid catalyst was named as Ag/SBA-15.

6.2.5 Preparation of Pd/M/SBA-15

Pd was deposited onto M/SBA-15 (M = Au, Ag) by LSPR-assisted deposition method under visible light irradiation. 0.1 g of M/SBA-15 was suspended and ultrasonicated in water (20 mL) till it becomes a clear solution. Subsequently solution was bubbled with continuous flow of Ar gas to ensure complete inert atmosphere conditions. It was followed by the injection of as calculated amounts of $Pd(OAc)_2$ (1.93 mM) solution prepared in acetic acid. The reaction mixture was then irradiated by a Xe lamp (500 W; San-Ei Electric Co. Ltd. XEF-501S) with a continuous stirring for a period of 2 h. The resultant solution was filtered and washed well with distilled water and acetone followed by drying at 80 ˚C in air overnight. The obtained catalyst was named as Pd/M/SBA-15.

6.2.6 Characterization

The overall characterization of the prepared catalysts, M/SBA-15 and Pd/M/SBA-15 (M=Au, Ag), was established by UV-vis, N_2 physisorption, transmission electron microscopy (TEM) and extended X-ray absorption fine structure (EXAFS) analysis. Shimadzu UV-2450 spectrophotometer was used to collect the reflectance UV-vis spectra of powdered samples. $BaSO_4$ was used as a reference solid and the spectra were collected by employing Kubelka-Munk function. BET surface area measurements were performed by using a BEL-SORP max system (BEL Japan, Inc.) at -196° C. Degassing of the samples was done in vacuum at 200° C for 3 h in order to remove the adsorbed impurities. TEM micrographs were obtained with a Hitachi Hf-2000 FE-TEM equipped with Kevex energy-dispersive X-ray detector operated at 200 kV. A 500 W Xenon lamp (San-Ei Electric Co. Ltd. XEF-501S) was used to carry out reactions under visible light irradiation. Au L_{III}-edge, Ag K-edge and Pd K-edge XAFS spectra were recorded by using a fluorescence-yield collection technique at the beam line 01B1 station with an attached Si (111) monochromator at SPring-8, JASRI, Harima, Japan (prop. No. 2014A1045 and 2015A1149). The data analysis and examination was finally carried out by Rigaku EXAFS analysis programme (REX2000). ESCA-3400 electron spectrometer was used to characterize core level electrons of Ag 3d, Pd 3d and Au 4f, by X-ray photoelectron spectroscopy.

6.2.7 Suzuki coupling reaction

The coupling of aryl halides and boronic acid was carried out by using suspension of catalyst in ethanol. 20 mg of catalyst along with 41.5 mg of K_2CO_3 base, 36.6 mg of phenylboronic acid was weighed in a Pyrex reactor (32 mL). 5.5 mL of ethanol was added onto the reactor and sealed with rubber septum. The reaction mixture was bubbled with Ar gas for 30 min, followed by injecting haloarene (0.2 mmol) through the rubber septum. The reactor was stirred under xenon lamp irradiation with a glass filter cutting out the ultraviolet portion of light. The amount of product formed was calibrated by using Shimadzu GC2014 gas chromatograph. The similar set of reactions was also performed without irradiation conditions.

6.2.8 Hydrolytic dehydrogenation of AB

The catalytic reaction of dehydrogenation of AB was carried out in an aqueous suspension of catalysts. Briefly, 20 mg of catalyst was dispersed in distilled water (5 mL) in a Pyrex tube (32 mL), sealed with a rubber septum. After bubbling Ar gas for 30 min, AB (20 µmol) was injected through the rubber septum and stirred continuously under either dark conditions or photo irradiation (320 mW cm^{-2}) using glass filter. The amount of hydrogen in the gas phase was measured by using Shimadzu GC-14B gas chromatograph.

6.3 Results and discussion

Synthesis and characterization of M/SBA-15 and Pd/M/SBA-15

In the previous chapter, a detailed discussion of synthesis and characterization of size controlled Ag and Pd/Ag bimetallic NPs supported within mesoporous silica is mentioned.[19-21] In this chapter, I have extended the previous work to Au NPs, which is known to be more stable, and a comparative study has been done with that of Ag. Spherical yellow Ag NPs and Au NPs within mesoporous channels can be synthesized by employing 1-hexanol and ethylene glycol respectively as a reducing agent and solvent.

With the interaction of UV and visible spectrum of light irradiation, plasmonic nanostructures has the ability to showcase resonant behavior with the incoming flux of photons. It is desirable to carefully design the nanostructures that can possibly interact with the entire solar spectrum, either by changing the composition, size or shape of metal NPs. The optical properties of the prepared catalysts investigated by UV-vis spectroscopy are shown in Figure 1. Ag and Au supported catalysts exhibited characteristic absorption attributing to the localized surface plasmon resonance (LSPR) at approximately 400 and 520 nm, respectively. Pd/SBA-15 did not exhibit significant absorption at more than 400 nm, while SBA-15 was completely transparent in the UV-vis range. Figure 1 (A) and (B) also show the optical properties of the bimetallic Pd/M plasmonic catalysts with increased overall absorption width, which could be due to increased electron density on the surface of metals. The appearance of a single peak in the UV-vis spectra confirmed the spherical shape of the nanostructures, which was further validated by TEM micrographs. It can be expected that the significant light absorption originated from plasmonic metals even after Pd deposition can successfully drive the catalytic reaction under visible light irradiation.

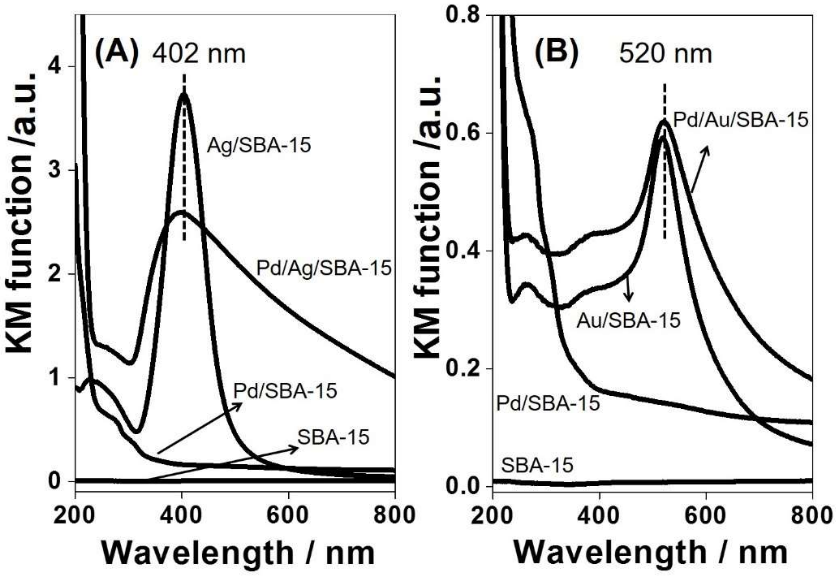

Figure 1. DR UV-Vis spectra of the prepared catalysts (A) Ag/SBA-15 & Pd/Ag/SBA-15 and (B) Au/SBA-15 & Pd/Au/SBA-15 along with Pd/SBA-15 and SBA-15.

Figure 2 (A) and (B) show the TEM images of the bimetallic Pd deposited Ag and Au NPs along with their pertinent histograms. Both samples exhibited spherical shape with average particle size of 4.2 and 4.9 nm for Pd/Ag and Pd/Au, respectively. From the micrographs, it can be observed that the growth of NPs occurred within the hexagonal mesoporous channels of silica showing narrow size distribution. There was no significant change in the size and morphology of NPs after Pd deposition.

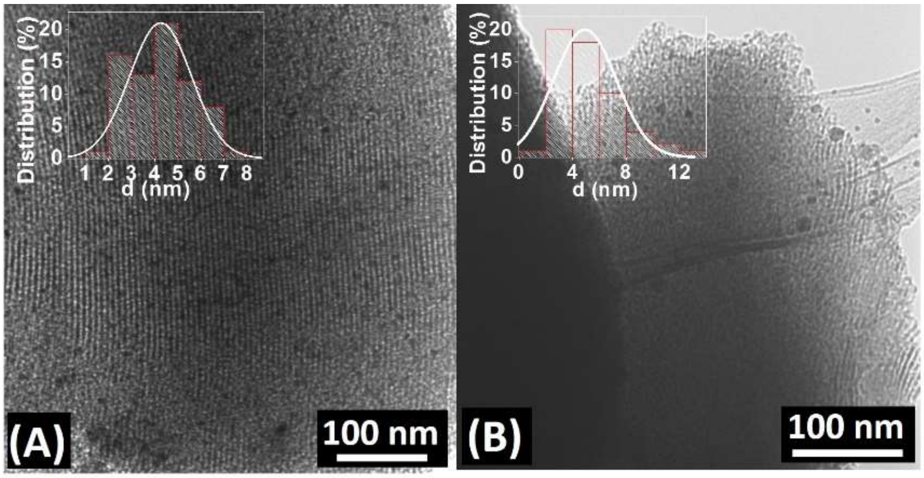

Figure 2. TEM micrographs and histograms (inset) for (A) Pd/Ag/SBA-15 and (B) Pd/Au/SBA-15.

The N_2 adsorption-desorption measurements were performed in order to study the changes induced in the textural characteristics of the prepared catalysts after metal incorporation. The textural parameters including mesoporous volume determined by Barrett-Joyner-Halenda (BJH) and surface area calculated by Brunauer-Emmett-Teller (BET) method, have been summarized in Table 1. The mesoporous volume and surface area of SBA-15 decreased from 1.32 to 1.18 $cm^3\ g^{-1}$ and 756 to 642 $m^2\ g^{-1}$ respectively for Pd/Au catalyst, while 1.32 to 1.10 $cm^3\ g^{-1}$ and 756 to 692 $m^2\ g^{-1}$ respectively for Pd/Ag catalyst. The successive decrease of mesoporous volume after plasmonic metals incorporation and Pd deposition confirms the accommodation of metal NPs within the pores of silica.

Table 1. Textural properties of the prepared catalysts.

Catalyst	**Mesopore volume (cm^3g^{-1})**	**BET surface area (m^2g^{-1})**
SBA-15	1.32	756
Au/SBA-15	1.21	668
Pd/Au/SBA-15	1.18	642
Ag/SBA-15	1.24	717
Pd/Ag/SBA-15	1.10	692

The local structures of the Au, Ag and Pd species supported on mesoporous silica were investigated by extended X-ray absorption fine structure (EXAFS) measurements. Figure 3 (A) represents the Fourier transforms (FT) of Au L_{III}-edge EXAFS of supported Pd/Au and Au catalysts along with standard samples including Au foil and $HAuCl_4$. SBA-15 supported Pd/Au and Au samples exhibited a main peak at 2.55 Å, similar to that of Au foil, assignable to contiguous Au-Au metallic bonding. The peak due to Au-Cl bond centered at 1.91 Å, which was observed for precursor $HAuCl_4$ solution, was not detected in Pd/Au and Au catalysts. Figure 3 (B) displays FT-EXAFS spectra at Ag K-edge of Ag and Pd/Ag supported catalysts, in addition to the Ag foil and AgO as reference samples. The intense peak at 2.7 Å is ascribed to the adjoining Ag-Ag metallic bond for Ag and Pd/Ag, confirming the presence of Ag^0 species. The obvious different peak of AgO at approximately 1.9 Å represents Ag-O-Ag bonding. Figure 3 (C) represents Pd K-edge FT-EXAFS spectra of Pd foil and PdO reference samples along with bimetallic Pd/Ag and Pd/Au samples. The appearance of a shoulder peak and shorter Pd-Pd distance in bimetallic Pd/Ag and Pd/Au samples, in contrast to the Pd foil, may be attributed to the existence of heteroatomic bonding.

XPS analysis was conducted to characterize the surface composition and chemical state of prepared samples. Figure 4 summarizes the spectrum of Ag 3d, Au 4f and Pd 3d core electrons for Ag, Au, Pd, Pd/Ag and Pd/Au nanostructures supported on SBA-15. The occurrence of doublet peaks $4f_{5/2}$, $4f_{7/2}$ for Au $3d_{3/2}$, $3d_{5/2}$ for Ag and Pd, confirming the metallic state of formed nanostructures. Figure 4 (a) and (b) show the shift in the binding energy of bimetallic Ag 3d and Au 4f core electrons towards higher and lower values, respectively, compared to monometallic supported catalysts.

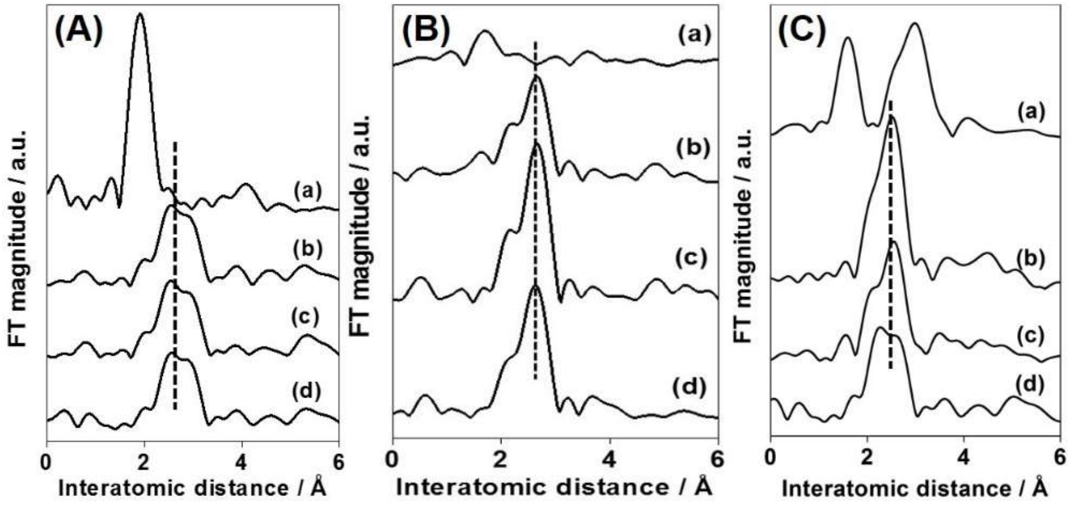

Figure 3. Fourier transforms of EXAFS spectra of (A) Au LIII-edge of (a) HAuCl4, (b) Au foil, (c) Au/SBA-15 and (d) Pd/Au/SBA-15. (B) Ag K-edge of (a) AgO, (b) Ag foil, (c) Ag/SBA-15 and (d) Pd/Ag/SBA-15. (C) Pd K-edge of (a) PdO, (b) Pd foil, (c) Pd/Ag/SBA-15 and (d) Pd/Au/SBA-15.

The integration of Ag with Pd induces the charge transfer from Ag atoms to Pd atoms owing to the net difference in electronegativity (Ag: 1.93 and Pd: 2.20), while opposite charge transfer occurs from Pd to Au because of larger electronegativity of Au (2.54) than Pd. Thus XPS proves to be a strong evidence to display the existence of bimetallic interaction via electron transfer mechanisms situated adjacent to each other.

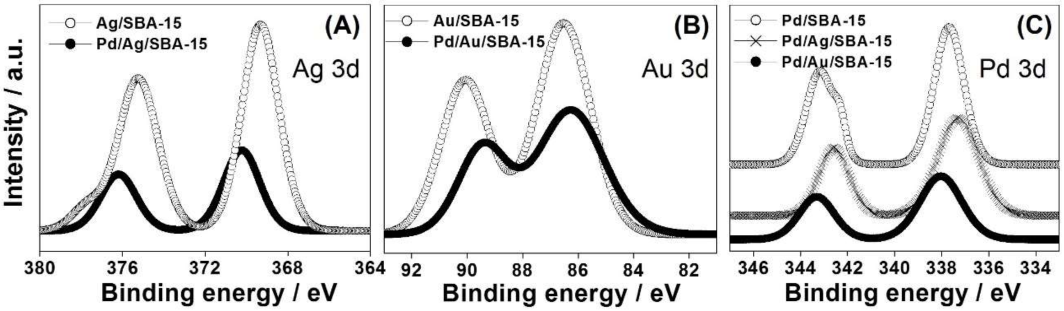

Figure 4. XPS spectra of (A) Ag 3d, (B) Au 4f and (C) Pd 3d for Ag/SBA-15, Au/SBA-15, Pd/Ag/SBA-15, Pd/Au/SBA-15 and Pd/SBA-15 catalysts.

Comparison of plasmonic photocatalysis

The optical properties of bimetallic nanostructures made to explore the catalytic activity of as-prepared Pd/Ag/SBA-15 and Pd/Au/SBA-15 for visible light enhanced reactions. In this report, I did two catalytic reactions, Suzuki coupling reaction and dehydrogenation of ammonia borane, to estimate the catalytic activity under irradiation conditions. An activity comparison has also been performed with that of prepared catalyst Pd/SBA-15, in order to study the synergistic effect of bimetallic Pd/Ag and Pd/Au NPs.

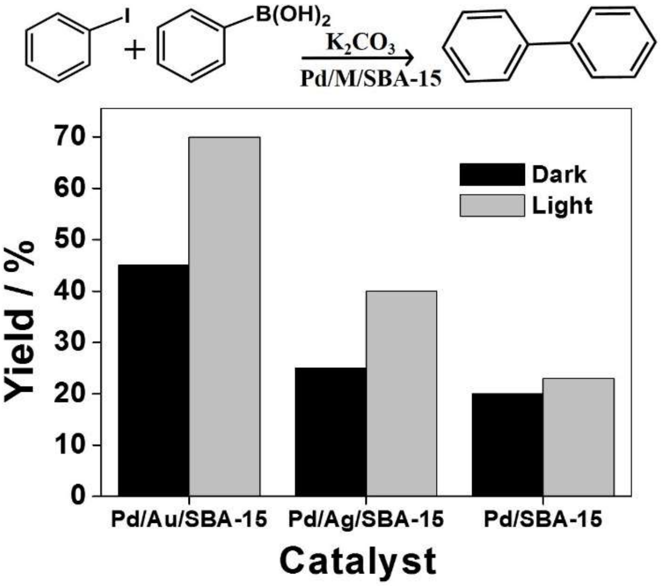

Figure 5. Results of Pd/M/SBA-15 for Suzuki coupling reaction under dark and visible light irradiation conditions.

The Pd-catalyzed Suzuki coupling reaction is an important carbon-carbon bond formation reaction[24-27], proven to be efficient industrially as well.[55-56] The commercial availability of the boronic reagents and mild reaction conditions make it even more environmentally safer in comparison to other coupling reactions involving organometallic reagents. The reaction studies were carried out at room temperature for 2 h in the presence of Pd/M/SBA-15, K_2CO_3 and ethanol used as the catalyst, base and solvent respectively. The optimum amount of Pd was found to be 0.5 wt % onto 1 wt % Au and Ag incorporated in mesoporous silica for both catalytic reactions. The reaction was first accomplished with iodobenzene as an aryl halide. No reaction products were observed using bare Ag and Au supported catalysts without Pd. The significant superior activity of Pd/Au catalyst in comparison to Pd/Ag was observed under both dark and light irradiation conditions, as shown in Figure 5. The effect of substituents as well as halide groups on aryl halides were investigated, as summarized in Table 2. The enhanced activity of aryl halides under visible light irradiation was observed with a reactivity trend of I > Br > Cl which may be due to the reluctance of halogen to undergo oxidative addition with Pd NPs.

Table 2. Scope of reaction with different substituents on the aryl halide.

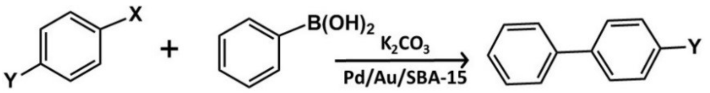

-X	-Y	Time (h)	Yield (%) Dark	Yield (%) Light
I	H	2	45	70
I	OCH_3	2	28	58
I	NO_2	2	64	80
Br	H	2	5	15
Br	OCH_3	6	3	11
Cl	H	8	1	4
Cl	NO_2	4	10	23

To study the effect of substituents on the susceptibility of the reaction, linear free energy relationship originally defined by Hammett, has been employed as mentioned in equation 2.

$$\log\frac{k}{k_0} = \sigma \ \rho \qquad (2)$$

Where k and k_0 are the rate constants for substituted and unsubstituted reactants respectively, σ is the substituent constant, which depends upon the nature and position of substituent and ρ is the reaction constant, a measure of sensitivity of the reaction to the electronic substituent effects. The Hammett ρ value for *p*-substituted iodobenzenes obtained under visible light irradiation was 0.11, which was substantially smaller than 0.31 observed under dark conditions. This low ρ value indicates the acceleration of the oxidative addition, which is considered the rate-determining step in the Suzuki coupling reaction, by the LSPR effect via electron transfer from excited Ag or Au NPs to the active Pd NPs.

In an effort to compare the potential catalytic ability of the Pd/Ag/SBA-15 and Pd/Au/SBA-15, the hydrogen production from ammonia borane (AB) was performed under dark and visible-light irradiation conditions. AB is the most extensively studied hydrogen storage material because of its high hydrogen content (19.6 wt %), non-toxicity and stability at RT, which strongly follows the criteria decided by US Department of energy (DOE) targets for onboard applications.[23] The reaction was carried out in aqueous solution of catalyst and AB in an inert atmosphere and the amount of hydrogen produced was monitored by gas chromatography. In this case, Pd/Ag catalyst showed superior catalytic activities to those of Pd/Au catalyst under both dark and light irradiation conditions, as shown in Figure 6.

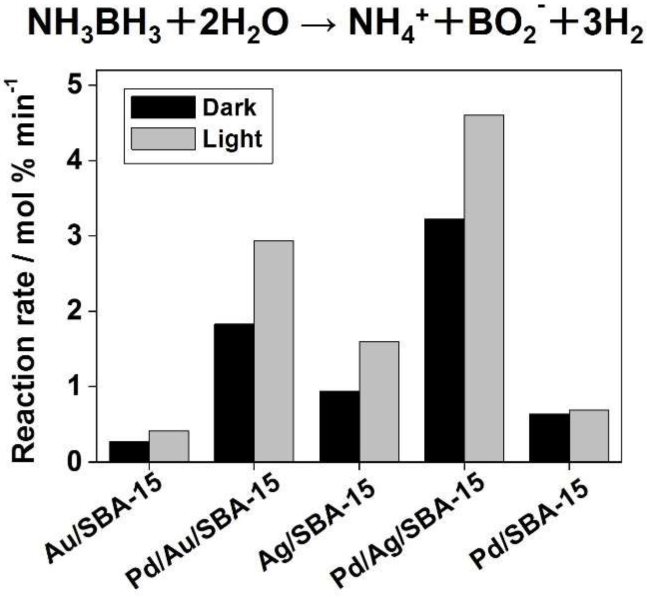

Figure 6. Reaction rates of M/SBA-15 and Pd/M/SBA-15 (M = Au, Ag) catalysts for AB dehydrogenation reaction under dark and visible light irradiation conditions.

The results in the AB dehydrogenation reaction include the contribution of Ag and Au, because Ag and Au are also active for this reaction, so it is difficult to compare both reaction. The Pd/Au catalyst showed superior performance in the coupling reaction, whereas Pd/Ag catalyst demonstrated excellent activity in the dehydrogenation reactions.

Figure 7 represents the performance increase by the wavelength dependence of catalytic performance over Pd/M/SBA-15 (M = Ag and Au) using monochromatic light irradiation (λ =

400, 570 and 650 nm) for AB dehydrogenation reaction. It was interesting to observe that the increasing rates of catalytic performance per light intensities were consistent with the LSPR absorption of Ag and Au NPs. Pd/Ag/SBA-15 and Pd/Au/SBA-15 showed superior activity at different wavelengths of 400 nm and 570 nm respectively. The different behavior of both NPs under monochromatic light irradiation, arising from different light absorption, can be responsible for their different response towards catalytic reactions.

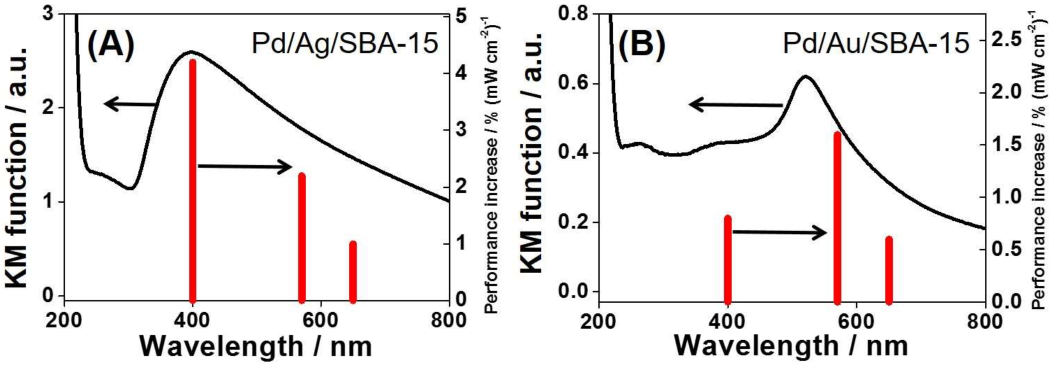

Figure 7. Wavelength dependence of (A) Pd/Ag/SBA-15 and (B) Pd/Au/SBA-15 under monochromatic light irradiation for AB dehydrogenation reaction.

A plausible mechanism has been proposed to understand the tentative reaction pathway under visible light irradiation. The resonant excitation of plasmonic NPs, which is accomplished by the matching of frequencies with that of the incident electromagnetic radiation, undergoes relaxation within tens of femtoseconds.[3,32,33] The possible outcomes of relaxation are either via radiative or non-radiative emission. It has already been studied that the possible mode of relaxation for metal NPs having diameter less than 30 nm is the non-radiative Landau damping process, which asserts the formation of electron-hole pairs.[28,29]

The conduction electron-hole pairs are generated by the elevated electric fields due to the accomplishment of the resonant condition between plasmonic metal nanostructures and its interaction with the electromagnetic radiation.[36]

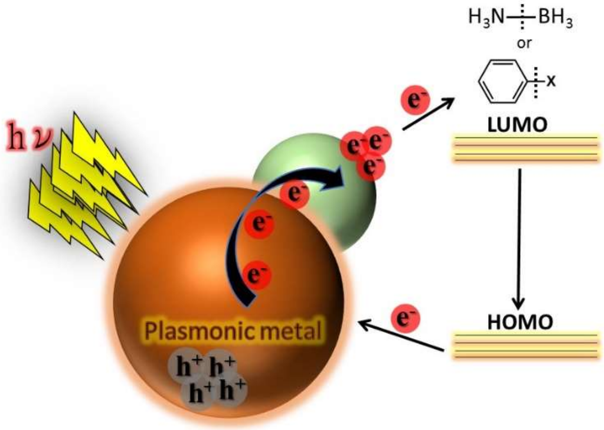

Scheme 1. Plausible mechanism for the enhanced catalytic activities under visible light irradiation in the presence of plasmonic metal NP.

These energetic electrons or so called hot electrons make themselves available at the surface Pd sites of the bimetallic Pd/M nanocatalysts.[57] This can be well supported with the considerably higher work function values of Pd (5.0 eV) than that of Ag (4.3 eV) and Au (4.7 eV).[34] Therefore, the lower fermi level of Pd than that of Ag and Au makes the electron transfer process quite feasible.[35] The energetic electrons generated upon resonant excitation of plasmonic metal NPs are accumulated to the lowest unoccupied molecular orbital (LUMO) of the reactant molecules through the Pd NPs, which transform them into the ionic/transient species and hence lead to their bond weakening, as shown in Scheme 1.[30] Q. Xiao et al. has recently reported the confirmation of bond weakening or elongation under irradiation conditions based on the theoretical DFT calculations.[31] After the activation of the reactant molecules, the electrons return to the HOMO and ultimately back to the plasmonic metal NPs. Not much of attention has been paid to this aspect of the plasmonic catalysis, but we hope that this work can influence and help in understanding the mechanism of LSPR-mediated chemical reaction.

6.4 Conclusions

A comparative study has been performed for Pd deposited Ag and Au NPs supported on mesoporous silica. The catalytic activity of these bimetallic NPs were explored for visible light-driven Suzuki coupling and AB dehydrogenation reactions, where specific performances were observed by Pd/Au and Pd/Ag NPs. A plausible mechanism of the plasmonic catalysis under light irradiation conditions is proposed, in which the electron transfer from plasmonic metal to active Pd and then to the adsorbed organic molecules enhance the bond weakening and/or cleavage.

6.5 References

[1] H. Cheng, X. Qian, Y. Kuwahara, K. Mori and H. Yamashita, *Adv. Mater.*, 2015, **25**, 4616.

[2] H. Cheng, K. Fuku, Y. Kuwahara, K. Mori and H. Yamashita, *J. Mater. Chem. A*, 2015, **3**, 5244.

[3] J. G. Smith, J. A. Faucheaux and P. K. Jain, *Nano Today*, 2015, **10**, 67.

[4] Y. C. Tsao, S. Rej, C. Y. Chiu and M. H. Huang, *J. Am. Chem. Soc.*, 2014, **136**, 396.

[5] S. Guo, S. Dong and E. Wang, *ACS Nano*, 2010, **4**, 547.

[6] K. J. Major, C. De and S. O. Obare, *Plasmonics*, 2009, **4**, 61.

[7] V. Abdelsayed, A. Aljarash, M. S. El-Shall, Z. A. Al Othman and A. H. Alghamdi, *Chem. Mater.*, 2009, **21**, 2825.

[8] S.-S. Chang, C.-L. Lee and C. R. C. Wang, *J. Phys. Chem. B*, 1997, **101**, 6661.

[9] S. Law, L. Yu, A. Rosenberg and D. Wasserman, *Nano Lett.*, 2013, **13**, 4569.

[10] Q. Zhou, G. Meng, N. Wu, N. Zhou, B. Chen, F. Li and Q. Huang, *Sensors Actuators B Chem.*, 2016, **223**, 447.

[11] D. Wang, Y. Li, G. Li Puma, C. Wang, P. Wang, W. Zhang and Q. Wang, *Appl. Catal. B Environ.*, 2015, **168-169**, 25.

[12] N. J. Halas, S. Lal, S. Link, W. S. Chang, D. Natelson, J. H. Hafner and P. Nordlander, *Adv. Mater.*, 2012, **24**, 4842.

[13] G. D. Osowiecki, E. Barakat, A. Naqavi and H. P. Herzig, *Opt. Express*, 2014, **22**, 20871.

[14] D. Manchon, J. Lermé, T. Zhang, A. Mosset, C. Jamois, C. Bonnet, J.-M. Rye, A. Belarouci, M. Broyer, M. Pellarin and E. Cottancin, *Nanoscale*, 2015, **7**, 1181.

[15] T. J. Antosiewicz and S. P. Apell, *RSC Adv.*, 2015, **5**, 6378.

[16] J. Cui, Y. Li, L. Liu, L. Chen, J. Xu, J. Ma, G. Fang, E. Zhu, H. Wu, L. Zhao, L. Wang and Y. Huang, *Nano Lett.*, 2015, **15**, 6295.

[17] J. Yang, Y. Li, L. Zu, L. Tong, G. Liu, Y. Qin and D. Shi, *ACS Appl. Mater. Interfaces*, 2015, **7**, 8200.

[18] X. Lang, X. Chen and J. Zhao, *Chem. Soc. Rev.*, 2014, **43**, 473.

[19] P. Verma, Y. Kuwahara, K. Mori and H. Yamashita, *J. Mater. Chem. A*, 2015, **3**, 18889.

[20] K. Mori, P. Verma, R. Hayashi, K. Fuku and H. Yamashita, *Chem. - A Eur. J.*, 2015, **21**, 11885.

[21] K. Fuku, R. Hayashi, S. Takakura, T. Kamegawa, K. Mori and H. Yamashita, *Angew. Chemie Int. Ed.*, 2013, **52**, 7446.

[22] B. L. Newalkar, J. Olanrewaju and S. Komarneni, *Chem. Mater.*, 2001, **13**, 552.

[23] E. K. Abo-Hamed, T. Pennycook, Y. Vaynzof, C. Toprakcioglu, A. Koutsioubas and O. A. Scherman, *Small*, 2014, **10**, 3145.

[24] N. Miyaura, T. Yanagi, A. Suzuki, *Synthetic Commun.* 1981, **11,** 513.

[25] K. Mori, M. Kawashima and H. Yamashita, *Chem. Commun.*, 2014, **50**, 14501.

[26] D. W. Old, J. P. Wolfe and S. L. Buchwald, *J. Am. Chem. Soc.*, 1998, **120**, 9722.

[27] X. Huang, Y. Li, Y. Chen, H. Zhou, X. Duan and Y. Huang, *Angew. Chemie Int. Ed.*, 2013, **52**, 6063.

[28] C. Burda, X. Chen, R. Narayanan and M. a. El-Sayed, *Chem. Rev.*, 2005, **105,** 1025.

[29] D. D. Evanoff and G. Chumanov, *ChemPhysChem*, 2005, **6**, 1221.

[30] S. Linic, U. Aslam, C. Boerigter and M. Morabito, *Nat. Mater.*, 2015, **14**, 567.

[31] Q. Xiao, S. Sarina, E. Jaatinen, J. Jia, D. P. Arnold, H. Liu and H. Zhu, *Green Chem.*, 2014, **16**, 4272.

[32] N. Del Fatti, C. Voisin, M. Achermann, S. Tzortzakis, D. Christofilos and F. Vallée, *Phys. Rev. B*, 2000, **61**, 16956.

[33] S. Link, S. Link, M. a. El-Sayed and M. El-Sayed, *J. Phys. Chem. B*, 1999, **103**, 8410.

[34] S. Trasatti, *J. Electroanal. Chem.* 1971, **33,** 351.

[35] A. Tanaka, K. Fuku, T. Nishi, K. Hashimoto and H. Kominami, *J. Phys. Chem. C* ., 2013, **117,** 16983.

[36] M. J. Kale, T. Avanesian and P. Christopher, *ACS Catal.*, 2014, **4**, 116.

[37] A. Henglein and D. Meisel, *Langmuir*, 1998, **14**, 7392.

[38] T. Ung, M. Giersig, D. Dunstan and P. Mulvaney, *Langmuir*, 1997, **13**, 1773.

[39] P. Mulvaney, J. Pérez-Juste, M. Giersig, L. M. Liz-Marzán and C. Pecharromán, *Plasmonics*, 2006, **1**, 61.

[40] C. Sönnichsen, T. Franzl, T. Wilk, G. von Plessen, J. Feldmann, O. Wilson and P. Mulvaney, *Phys. Rev. Lett.*, 2002, **88**, 077402.

[41] C. Ropers, D. J. Park, G. Stibenz, G. Steinmeyer, J. Kim, D. S. Kim and C. Lienau, *Phys. Rev. Lett.*, 2005, **94**, 113901.

[42] H. Chen, L. Shao, Q. Li and J. Wang, *Chem. Soc. Rev.*, 2013, **42**, 2679.

[43] T. Ding, D. Sigle, L. Zhang, J. Mertens, B. de Nijs and J. Baumberg, *ACS Nano*, 2015, **9**, 6110.

[44] S. K. Dondapati, M. Ludemann, R. Müller, S. Schwieger, a. Schwemer, B. Händel, D. Kwiatkowski, M. Djiango, E. Runge and T. a. Klar, *Nano Lett.*, 2012, **12**, 1247.

[45] D. Dorfs, T. Härtling, K. Miszta, N. C. Bigall, M. R. Kim, A. Genovese, A. Falqui, M. Povia and L. Manna, *J. Am. Chem. Soc.*, 2011, **133**, 11175.

[46] K. S. Lee and M. a. El-Sayed, *J. Phys. Chem. B*, 2006, **110**, 19220.

[47] C. L. Nehl and J. H. Hafner, *J. Mater. Chem.*, 2008, **18**, 2415.

[48] C. Novo and P. Mulvaney, *Nano Lett.*, 2007, **7**, 520.

[49] H. Chen, L. Shao, K. C. Woo, T. Ming, H. Q. Lin and J. Wang, *J. Phys. Chem. C*, 2009, **113**, 17691.

[50] K. a. Willets and R. P. Van Duyne, *Annu. Rev. Phys. Chem.*, 2007, **58**, 267.

[51] S. Kubo, A. Diaz, Y. Tang, T. S. Mayer, I. C. Khoo and T. E. Mallouk, *Nano Lett.*, 2007, **7**, 3418.

[52] H. Chen, X. Kou, Z. Yang, W. Ni and J. Wang, *Langmuir*, 2008, **24**, 5233.

[53] K. Mayer, J. Hafner, *J. Chem. Rev.,* 2011, **111,** 3828.

[54] A. J. Haes, S. Zou, G. C. Schatz and R. P. Van Duyne, *J. Phys. Chem. B*, 2004, **108**, 109.

[55] F. Wang, C. Li, H. Chen, R. Jiang, D. Sun, Q. Li, J. Wang, J. C. Yu, C. Yan and L. Sun, *J. Am. Chem. Soc.*, 2013, **135**, 5588.

[56] P. P. Fang, A. Jutand, Z. Q. Tian and C. Amatore, *Angew. Chemie - Int. Ed.*, 2011, **50**, 12184.

[57] W. Xie and S. Schlücker, *Nat. Commun.*, 2015, **6,** 7570.

[58] Q. Zhang, J. Xie, J. Lee, J. Zhang and C. Boothroyd, *Small*, 2008, **4**, 1067.

[59] M. Gong, X. Jin, R. Sakidja and S. Ren, *Nano Lett.*, 2015, **15**, 8347.

[60] K. Haldar, S. Kundu and A. Patra, *ACS Appl. Mater. Interfaces*, 2014, **6**, 21946.

[61] S. Schlünemann, G. dodekatos and H. Tüysüz, *Chem. Mater.*,2015, **27**, 7743.

Chapter VII

Enhancement of Ag-based Plasmonic Photocatalysis in the Hydrogen Production from Ammonia Borane by the Assist of Single-site Ti-oxide Moiety within the Silica Framework

7.1 Introduction

In the early 20th century, the initial studies on the optical properties of metallic colloids by Gustav Mie formed the basis of the research in the field of plasmonics.[1] In nanoplasmonics, metallic nanostructures serves as a class of highly sensitive optical antennas that layout the transformation of solar energy via localized surface plasmon resonance (LSPR).[2-4] The free electrons present on the metal surface interacts strongly with the incoming incident light radiation, generating collective oscillations, known as surface plasmon polariton or surface plasmons (SPs). These plasmons are able to confine light into metal-dielectric interfaces, enhancing the local electromagnetic field at the interface. In this phenomenon, metal nanostructures are always present in nanoscale regimes, which add on to the advantage of having surface-active sites and enhanced catalytic activities. The enhanced activity under exposure conditions for a particular reaction can be understood by one of the three possible mechanisms; i) photothermal conversion, ii) local enhancement of electric field and iii) generation and injection of hot electrons.[5] As per scientific and technological perspectives, noble metals especially Ag and Au have gained recent attention due to their interesting plasmonic properties showing efficient catalysis under visible light irradiation.

Recently, variety of plasmonic nanostructures has been developed by the combination with dye sensitizers, metal nanoclusters, polymers, solar cells and also in fluorescence enhancement techniques.[6] In my group, plasmon-related research activities have been mainly targeted on the insulator supported pure plasmon metal[7] and semiconductor[8] based plasmon catalysts explored for variety of application reactions. In the initial stage of its development, the improbability of the mechanism for example extremely short lifetimes of charge carriers, had been a huge question. However, many experimental studies and observations have proved the participation of hot electrons-induced chemical reactions.[9,10]

On the other hand, it has been well studied that isolated Ti-oxide moieties incorporated within mesoporous silica framework can serve as an efficient photocatalyst, under UV light exposure conditions. These oxide moieties are tetrahedrally coordinated and found to be highly dispersed at atomic level. They are popularly termed as “single-site photocatalyst” due to the direct tetrahedral coordination with oxygen atoms and substitution of Si atoms by transition metal in the whole silica matrix.[11,12] The generation of adjoining electron-hole pairs, which is different from that of bulk semiconductors like TiO_2, accounts for its special properties. Combination of mesoporous materials along with highly dispersed transition metal oxide moieties creates attractive hybrid materials due to their better adsorption and catalytic properties.[13,14] Having the disadvantage of being active only under UV light, more sophisticated functionalized photocatalytic system that can harness the ideal energy source of solar light needs to be developed. In the present study, I have designed and constructed new type of photocatalytic system by introducing the titanium oxide moieties along with plasmonic Ag NPs within the framework of silica, in order to bridge together the vis-active plasmonic and UV-active single-site photocatalysts. An unexpected high reaction rate in the hydrogen production from ammonia borane (AB), attributing to the combined effect of both optical properties, was observed under UV-vis light irradiation.

7.2 Experimental

7.2.1 Materials

Tetraethyl orthosilicate ($(C_2H_5O)_4Si)$), hydrochloric acid (HCl), 1-hexanol ($C_6H_{13}OH$), Tetra n-butyl titanate (TBOT), acetone, silver nitrate ($AgNO_3$), sodium laurate, and ethanol were purchased from Nacalai Tesque Inc. Triblock pluronic P123® (Mw = 5800, $PEO_{20}PPO_{70}PEO_{20}$) and ammonia borane (NH_3BH_3) were obtained from Sigma-Aldrich Co. All chemicals were used as received without any further purification.

7.2.2 Synthesis of SBA-15

Mesoporous silica SBA-15 was synthesized according to the method reported in literature utilizing Pluronic P123® as a structure directing agent and tetraethyl orthosilicate (TEOS) as a silica source under acidic conditions ($pH < 1$).[44]

7.2.3 Synthesis of Ti-SBA-15

The Ti-containing mesoporous silica (Ti-SBA-15) was prepared by using tetraethyl orthosilicate (TEOS) and titanium tetrabutoxide ($Ti(OBu)_4$, TBOT) as the starting material sources of Si and Ti, respectively.[16] Briefly, 2.67 g of P123® was mixed firmly with 100 mL of 0.1 M HCl solution and stirred well for 2 h at 40 ˚C at 400 rpm. After complete dispersion, TEOS and TBOT was slowly added into the solution and stirred continuously for 24 h at 40 ˚C. The obtained mixture was transferred to the Teflon bottle followed by aging at 80 ˚C for 24 h. The white suspension was then filtered, washed with ample amounts of deionized water and dried at 80 ˚C overnight. Finally, calcination at 550 ˚C was done for a period of 5 h in order to ensure the complete removal of the organic templates used during the synthesis. The content of Ti in Ti-SBA-15 was varied from 0 to 1.0 mol % per Si atom.

7.2.4 Synthesis of Ag/SBA-15 and Ag/Ti-SBA-15

The incorporation of Ag (1 wt %) onto SBA-15 (0.2 g) and Ti-SBA-15 (0.2 g) was carried out by microwave assisted alcohol reduction method.[7] At first, the silica support was ultrasonicated well with 1-hexanol (40 mL) for 30 min. Further, sodium laurate (surface directing agent, 10 mg) and precursor $AgNO_3$ aqueous solution (100 mmol, 0.2 mL) was injected into the solution followed by Ar bubbling for 15 min. The resultant mixture was then exposed to microwave irradiation (500 W) for a period of 3 min. The solution was then filtered and dried in air at 80 ˚C.

7.2.5 Synthesis of $Ag/TiO_2/SBA$-15

At first, TiO_2/SBA-15 was synthesized by internal hydrolysis method.[45] The calculated amount of titanium source, TBOT, was first dissolved in isopropanol and injected into SBA-15 powder maintained in Ar atmosphere. The obtained suspension was stirred for 2 h in order to completely adsorb the Ti source on silica. Later, the suspension was filtered and washed with isopropanol, followed by drying overnight at 80 ˚C in air. The sample was then calcined at 500 ˚C for 4 h. The content of TiO_2 in TiO_2/SBA-15 was adjusted to be 10 wt%. The prepared TiO_2/SBA-15 was used as a support to deposit Ag (1 wt %) using the above mentioned procedure similar to that of Ag/SBA-15 and Ag/Ti-SBA-15.

7.2.6 Characterization

The overall characterization of the prepared supports and catalysts was established by UV-vis, N_2 physisorption, transmission electron microscopy (TEM), field emission scanning electron microscopy (FE-SEM), X-ray photoelectron spectroscopy (XPS) and extended X-ray absorption fine structure (EXAFS) analysis. Shimadzu UV-2450 spectrophotometer was used to collect the reflectance UV-vis spectra of powdered samples. $BaSO_4$ was used as a reference solid and the spectra were collected by employing Kubelka-Munk function. Brunauer–Emmett–Teller

(BET) surface area measurements were performed by using a BEL-SORP max system (MicrotracBEL) at -196° C. Degassing of the samples was done in vacuum at 200° C for 3 h in order to remove the adsorbed impurities. TEM micrographs were obtained with a Hitachi Hf-2000 FE-TEM equipped with Kevex energy-dispersive X-ray detector operated at 200 kV. Field-emission scanning electron microscope (FE-SEM) images were obtained with a JEOL JSM-6500F. Ag K-edge XAFS spectra were recorded by using a fluorescence-yield collection technique at the beam line 01B1 station with an attached Si (111) monochromator at SPring-8, JASRI, Harima, Japan (prop. No. 2014A1045, 2015A1149, 2016A1095 and 2016A1057). Ti K-edge X-ray absorption fine structure (XAFS) spectra of Ti-containing porous silica were recorded at 25° C in fluorescence mode at the BL-7C facility of the Photon Factory at the High-Energy Acceleration Research Organization (KEK) in Tsukuba, Japan. The data analysis and examination was finally carried out by Rigaku EXAFS analysis program (REX2000). ESCA-3400 electron spectrometer was used to characterize samples for X-ray photoelectron spectroscopy.

7.2.7 Hydrolytic dehydrogenation of AB

The catalytic reaction of dehydrogenation of AB was carried out in an aqueous suspension of catalysts. Briefly, 20 mg of catalyst was dispersed in distilled water (5 mL) in a quartz vessel (66 mL), sealed with a rubber septum. After bubbling Ar gas for 30 min, AB (20 μmol) was injected through the rubber septum and stirred continuously under either dark conditions or photo irradiation (320 mW cm^{-2}). A 500 W Xenon lamp (San-Ei Electric Co. Ltd. XEF-501S) was used to carry out reactions under UV-visible light irradiation. The amount of hydrogen in the gas phase was measured by using Shimadzu GC-14B gas chromatograph equipped with a TCD detector.

7.3 Results and Discussion

Synthesis and characterization of Ti-containing mesoporous silica, Ti-SBA-15

The characterization of Ti incorporated mesoporous silica was carried out in order to confirm the porosity, surface area and the state of Ti-oxide moieties present within the framework of silica. The process was executed by XRD, N_2 physisorption, XAFS and UV-vis measurements. The low-angle XRD measurement of SBA-15 and Ti-SBA-15 exhibited two peaks at around 1.0–2.0° corresponding to a hexagonal structure, demonstrating ordered mesoporous structures. Figure 1 (A) shows the Ti K-edge X-ray absorption near-edge structure (XANES) spectra of

Ag/Ti-SBA-15, Ti-SBA-15, TBOT and TiO_2. A single pre-edge peak at 4968 eV for Ti-SBA-15 and Ag/Ti-SBA-15, similar to that of TPOT, was observed. This peak can be assigned to the electronic transition from 1s to t_{2g}, confirming the isolated Ti-oxide moieties in Ti-SBA-15 and Ag/Ti-SBA-15 in tetrahedral geometry. However, in TiO_2, well defined pre-edge peaks from 4964 to 4974 eV represent titanium in octahedral geometry.[15] In Figure 1 (B), the intense peak of absorption observed in the UV region for Ti-oxide species below 280 nm can be assigned to ligand to metal charge transfer (LMCT) transition from oxygen (O^{2-}) to tetrahedral titanium (Ti^{4+}) which is different from the absorption peak observed in TiO_2 powder from 200-400 nm due to bandgap excitation. This blue shift in the absorption wavelength can be ascribed to the size quantification effects due to extremely small and unsaturated Ti-oxide moieties with tetrahedral geometry.[16, 17] Also, Figure 1B shows the different mol % doping of Ti (1a - 1d) within the framework of SBA-15. The optimum doping amount was found out to be 0.5 mol % (1c), confirmed by catalytic reaction performance, as discussed later.

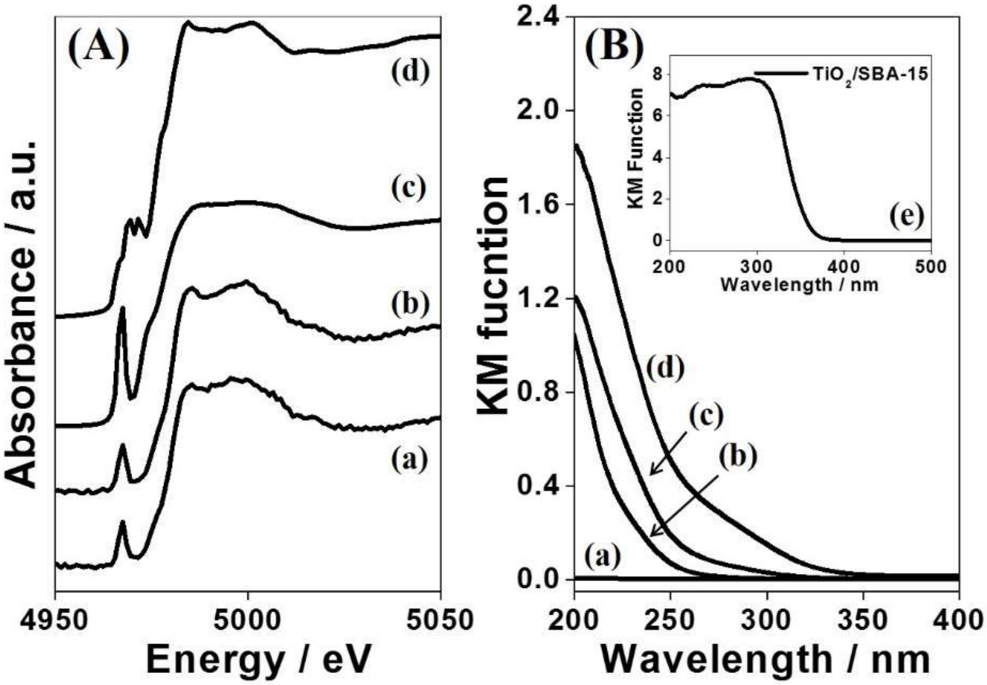

Figure 1. (A) Ti K-edge XANES spectra of (a) Ag/Ti-SBA-15, (b) Ti-SBA-15, (c) TBOT, (d) TiO_2 and (B) UV-vis spectra of (a) SBA-15, (b) Ti-SBA-15 (0.25 mol %), (c) Ti-SBA-15 (0.5 mol %), (d) Ti-SBA-15 (1.0 mol %), (e) TiO_2/SBA-15.

Table 1. Textural properties and particle size of prepared catalysts determined by N_2-physisorption measurements and TEM images, respectively.

Sample	**Surface area (m^2g^{-1})**	**Total pore volume (cm^3g^{-1})**	**Pore size (nm)**	**Ag particle size (nm)**
SBA-15	668	0.61	6.1	---
Ti-SBA-15	805	0.88	7.2	---
TiO_2/SBA-15	531	0.66	7.2	---
Ag/SBA-15	575	0.49	4.2	3.1
Ag/Ti-SBA-15	596	0.67	6.1	3.2
Ag/TiO_2/SBA-15	569	0.62	6.7	4.4

The SEM micrographs for SBA-15 were found to be typical rope-like morphology, forming an aggregation of wheat like structures, due to the domination of long range forces over particle formation. In contrast, the Ti-SBA-15 morphology was observed to be spherical as shown in Figure 2. The addition of TBOT during synthesis procedure might slows down the condensation rate of silica, lowering the curvature energy and hence leading to more regular morphology.[18] The N_2 adsorption-desorption measurements were carried out to determine specific surface area, pore volume and pore size of prepared catalysts as summarized in Table 1. It was observed that incorporation of Ag NPs decreased the pore size and pore volume, while still maintaining the high surface area and type-IV isotherms, hence showing the high dispersity of NPs within the mesopores of SBA-15 and Ti-SBA-15. The surface area, pore size and pore volume had no effect on the size of metal NPs and their hydrogen generation ability.

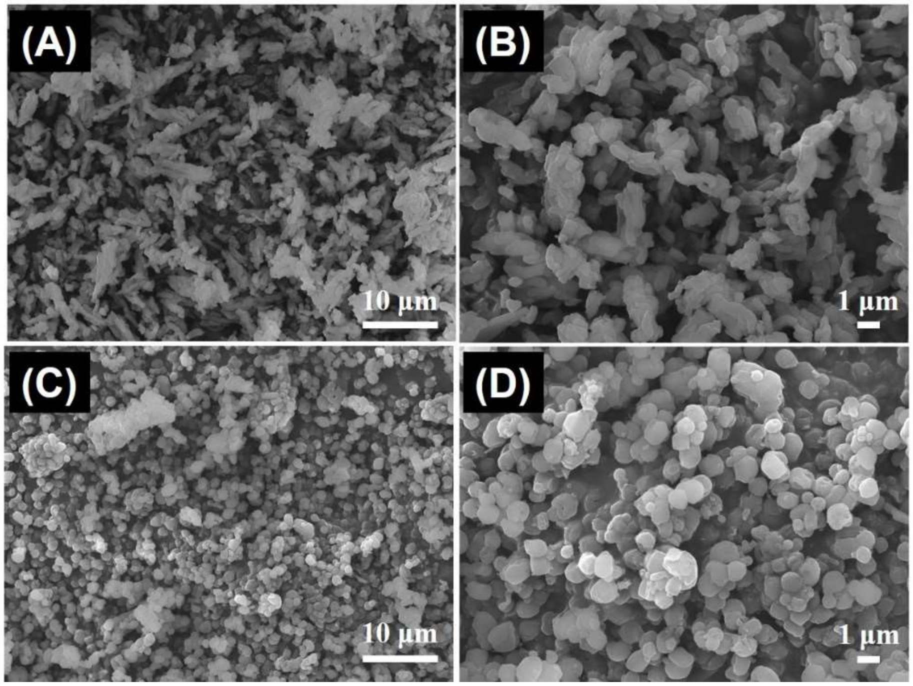

Figure 2. SEM micrographs for (A, B) SBA-15 and (C, D) Ti-SBA-15.

Synthesis and characterization of Ag NPs deposited on Ti-SBA-15

Designing rapid synthetic techniques for metal nanoparticles would be very advantageous in order to embellish the scientific creativity. Microwave chemistry is gaining much attention because of uniform heating, short reaction times and improved product yield to form NPs of very small size and narrow distribution.[19] In the present study, Ag NPs were deposited within the confined mesopores of SBA-15 and Ti-SBA-15 by an established procedure[7] employing microwave irradiation to achieve NPs of very small size and narrow distribution as can be seen in Figure 3. It represents TEM micrographs along with their pertinent histograms for Ag/SBA-15, Ag/Ti-SBA-15 and Ag/TiO_2/SBA-15 catalysts with average particle sizes of 3.1, 3.2 and 4.4 nm, respectively. The effect of Ti incorporation on the size of Ag NPs seems to be less significant. However, with TiO_2 deposited silica, TiO_2 (patches) can be seen in the following TEM micrograph (red arrows) along with small sized spherically grown Ag NPs.

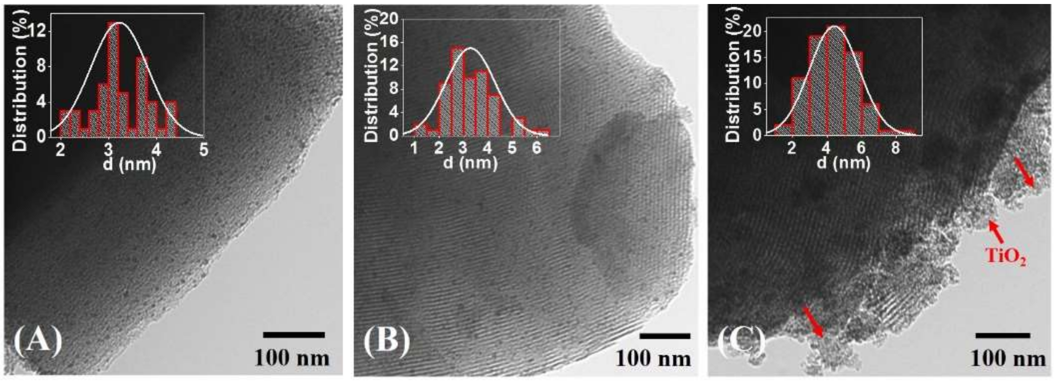

Figure 3. TEM images and histograms (inset) for (A) Ag/SBA-15, (B) Ag/Ti-SBA-15 and (C) Ag/TiO_2/SBA-15.

Interaction of polaritons with the incoming photons and reaction systems should be carefully monitored in order to achieve the maximum performance.[20,21] The DR UV-vis spectrum of support material without Ag i.e. SBA-15, Ti-SBA-15 and TiO_2/SBA-15 has already been discussed in the previous section (Figure 1B). As shown in Figure 4, all Ag based catalysts displayed sharp plasmonic peak at 405, 410, 420 nm for Ag/SBA-15, Ag/Ti-SBA-15 and Ag/TiO_2/SBA-15, respectively. The shifting of plasmonic peak towards higher wavenumbers resulted from the increment of the NP size as confirmed by TEM (Table 1).

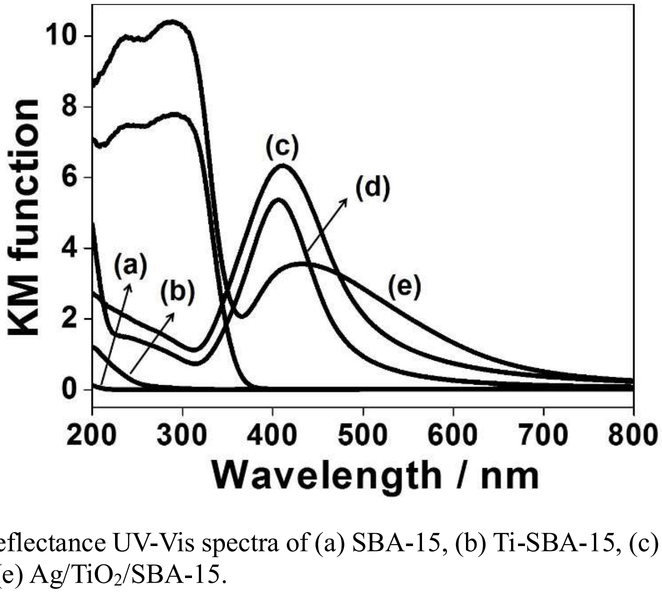

Figure 4. Diffuse reflectance UV-Vis spectra of (a) SBA-15, (b) Ti-SBA-15, (c) Ag/Ti-SBA-15, (d) Ag/SBA-15 and (e) Ag/TiO_2/SBA-15.

The local structure of supported Ag NPs was also characterized by Fourier transforms (FT) of Ag K-edge extended X-ray absorption fine structure (EXAFS) spectra, as presented in Figure 5. The main peak shown by Ag foil at approximately 2.7 Å is assigned to the contiguous Ag-Ag bond in the metallic state. The FT-EXAFS spectrum of all samples were found to be similar to that of Ag foil but different from the spectral peak of AgO at 1.7 Å arising from Ag-O bonds, thus indicating the absence of silver oxide species within these samples.

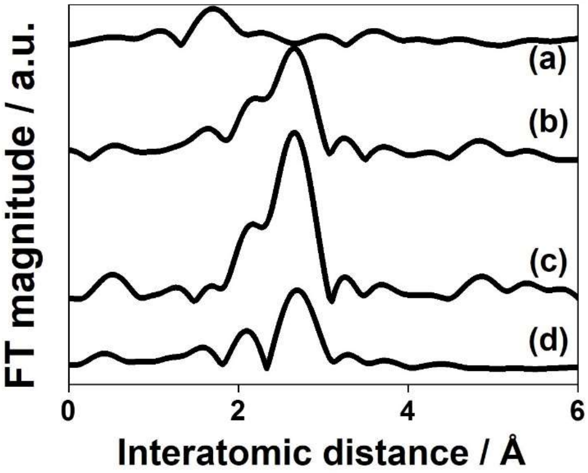

Figure 5. Ag K-edge EXAFS spectra of (a) AgO, (b) Ag foil, (c) Ag/SBA-15 and (d) Ag/Ti-SBA-15.

In XPS, as widely known, the binding energy (B.E.) of electron depends on two factors; i) the oxidation state of the atom, ii) local chemical and physical environment.[22] XPS measurement was carried out to study the effect of local chemical environment around silver and the spectra obtained is shown in Figure 6. The core level spectrum representing two strong peaks due to the splitting of 3d doublet by 6.0 eV also confirms the metallic nature of Ag.[23] The peaks observed at binding energies of 375.2 eV and 369.3 eV (Figure 4 (a)) are ascribed to $3d_{3/2}$ and $3d_{5/2}$ core levels of Ag in Ag/SBA-15 respectively. The shifting of B.E. towards lower values with incorporation of Ti-oxide and TiO_2 moieties (Figure 4 (b) and (c)) confirms the possible interactions of Ti-oxide and Ag. This shift can be interpreted as the electron transfer process from Ti-oxide moieties to Ag, hence creating electron rich Ag species, which ultimately assist in the enhanced rate of reaction as will be mentioned the following section.

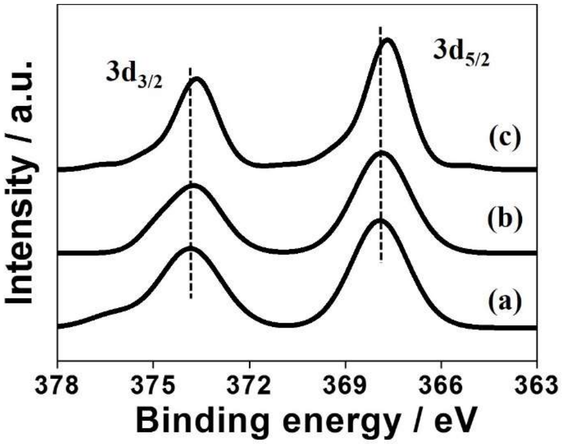

Figure 6. XPS spectra of Ag 3d for (a) Ag/SBA-15 (b) Ag/Ti-SBA-15 and (c) Ag/TiO_2/SBA-15.

Catalytic dehydrogenation activity of Ag NPs supported on Ti-SBA-15

The sustainable production of H_2 is a hot topic considering its role in replacing non-renewable resources. Due to its high demand at industrial processes such as the synthesis of ammonia, fertilizers, oil refining and notion of making it as a green energy carrier, molecular hydrogen production has become an exceptionally important priority.[24,25] Numerous efforts have been put forward in order to establish a safe and efficient storage system of hydrogen.[26,27]

One of promising approaches towards clean and safe hydrogen storage materials is the utilization of chemical hydrides[28], borohydrides,[29,30] ammoniates[31,32] and ammonia borane[33-34] (AB), thereby promoting the field of hydrogen energy. Considering the hydrolysis of AB, the reaction rate is almost negligible at RT in the absence of catalyst. This reaction is of paramount importance because AB has gained significant attention to act as a potential hydrogen storage material by the virtue of its high hydrogen content (19.6 wt %), non-toxicity, solubility and stability in water at RT. In recent years, a combination of various bimetallic nanoparticles such as FeNi, Pd/Ag, NiPt, Ag@CoNi, Pt-Co@GO, Ru@Co, Cu@Co_3O_4, CuCo@MOF, Pt/CNT, Ni_2P etc. have been tested for hydrogen production from AB.[35-42] In the present study, Ti-SBA-15, Ag/SBA-15, Ag/Ti-SBA-15, Ag/TiO_2/SBA-15 and physical mixture of (Ti + Ag)/SBA-15 catalysts were examined for this reaction at RT conditions. AB is capable of producing 3 equivalents of hydrogen via hydrolysis in the presence of appropriate catalysts as the following equation 1.[43]

$$NH_3BH_3 + 2H_2O \longrightarrow NH_4^+ + BO_2^- + 3H_2 \qquad (1)$$

The observed hydrogen production rates calculated at 20 min of reaction, have been summarized in Figure 7. An approximate equivalent ratio of H_2/AB = 3.0 was observed under dark and light irradiation conditions. A trace of hydrogen was evolved in the presence of bare Ti-SBA-15 catalyst because of its acidic nature. It should be noted that the optimum doping of Ti (0.5 mol % per Si) in Ag/Ti-SBA-15 could lead to reaction rate of as high as 2.4 μmol min^{-1}, which is 2.8 times higher than Ag/SBA-15 (0.84 μmol min^{-1}) under dark conditions, demonstrating that the isolated Ti species (tetrahedral geometry) increase the reaction rate. This could also be due to the morphological variations of the support materials (see Figure 2), which possibly affect the diffusion of reactant molecules. Ag/TiO_2/SBA-15 exhibited least activity (0.33 μmol min^{-1}) after bare Ti-SBA-15, thus giving an evidence that aggregated Ti-oxide moieties (octahedral geometry) have little effect on the catalysis of Ag NPs. A physical mixture of both the components (Ti + Ag) displayed an average reaction rate of 0.41 μmol min^{-1}, hence validating the necessity of creation of heterojunction at atomic level.

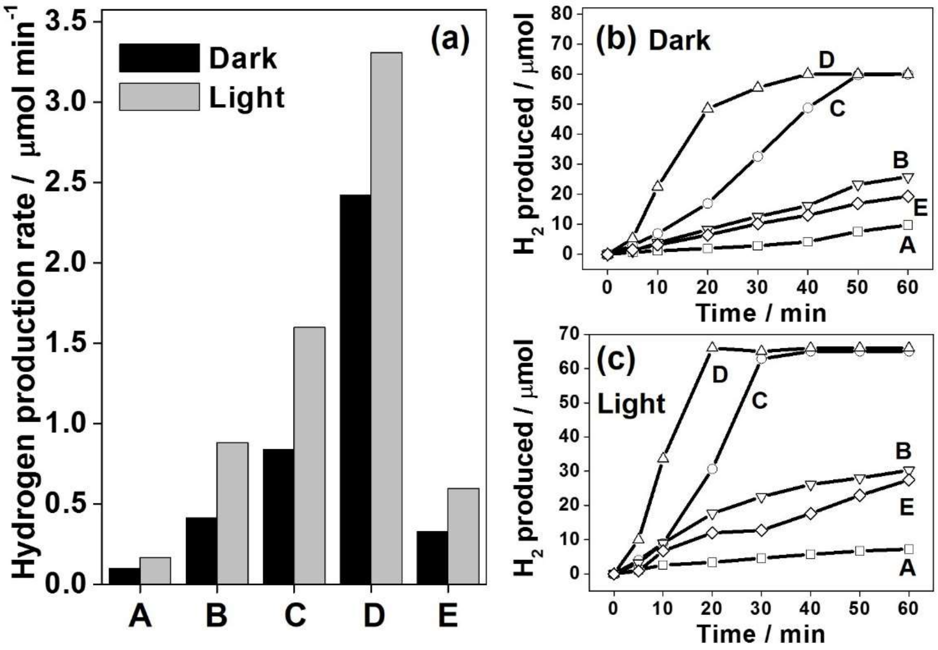

Figure 7. (a) Reaction rate comparison for AB dehydrogenation at room temperature, (b) Dark and (c) Light irradiation time profile hydrogen production for (A) Ti-SBA-15, (B) (Ag+Ti)/SBA-15, (C) Ag/SBA-15, (D) Ag/Ti-SBA-15 and (E) Ag/TiO_2/SBA-15.

Under UV-vis light irradiation (500W Xe lamp), employing quartz vessel for catalytic reaction without the usage of filter, all reaction rates found to be significantly enhanced. Ag/Ti-

SBA-15 was found to be the most active with the highest hydrogen production rate of 3.3 μmol min^{-1} showing a maximum enhancement effect among all samples, where 0.5 mol % of Ti-oxide doping was found to be the optimum ratio to achieve the highest catalytic activity. The cut-off filter was utilized in order to understand the effect of irradiating UV-vis and only Vis light irradiation. As shown in Figure 8, the reaction was carried out in dark and light irradiation condition with and without filter (cut-off filter shorter than $\lambda < 420$ nm). The maximum activity and reaction rate (3.3 μmol min^{-1}) was observed under light irradiation without filter proving that the exploitation of both UV and visible light is the main cause of the increased catalytic activity of the prepared catalyst. Also, the effect of temperature was found to be insignificant under visible light irradiation during the course of reaction. The equation reported by Christopher et al. also evidences the negligible thermal effect during plasmonic catalytic reaction as the following equation 2.

$$T = T_{\infty} + \frac{I_0 K_{abs}\ r_0}{6 k_{\infty}} \tag{2}$$

Upon inclusion of all parameters in equation, $I_0 = 320$ mWcm^{-2}, $r_0 = 3 - 50$ nm, $T_{\infty} = 298$ K, and the values calculated by Christopher et al. ($K_{abs} = 3$, $k_{\infty} = 40$ mWm^{-1}K^{-1}), the temperature increase due to plasmonic heating effect was found to be less than 0.002 K.[46]

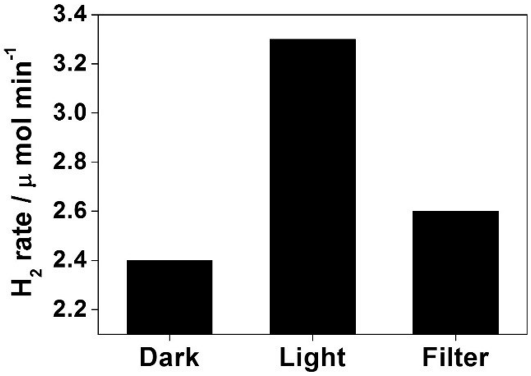

Figure 8. Hydrogen production rate comparison of Ag/Ti-SBA-15 under dark and light irradiation, with and without filter.

The plausible mechanism for hydrolysis of AB involves adsorption of AB on the metal NPs to form an activated complex, which is the rate determining step for the reaction. The complex intermediates further attacked by H_2O molecule, leading to the cleavage of B-N bond, and hence producing H_2. The improved reaction rate of Ag/Ti-SBA-15 than Ag/SBA-15 under dark conditions can be explained due to the heteroatomic interaction of Ag and Ti, as observed by XPS. Here, I predict the accelerated hydrogen production activity is due to the presence of Lewis acidic Ti^{3+} site, which leads to the cooperative activation of Lewis basic NH_3BH_3 with the assistance of Lewis acid sites. Thus the increased surface charge density of Ag NPs accounts for better reaction activity of Ag/Ti than Ag NPs. This effect is more pronounced under visible light irradiation due to the effective charge separation of Ag by LSPR effect.

On illuminating the NPs with light irradiation, the electromagnetic field develops a force on the conduction electrons, making them to move on the surface of NP. This leads to the creation of dipole, i.e. collection of positive and negative charges on either side of the NP surface. Even after the removal of field, electrons show displacement from equilibrium position and oscillate with a certain frequency called as resonant or plasmonic frequency. It establishes when the frequency of incident light matches with the oscillating electron frequency against the restoring force.

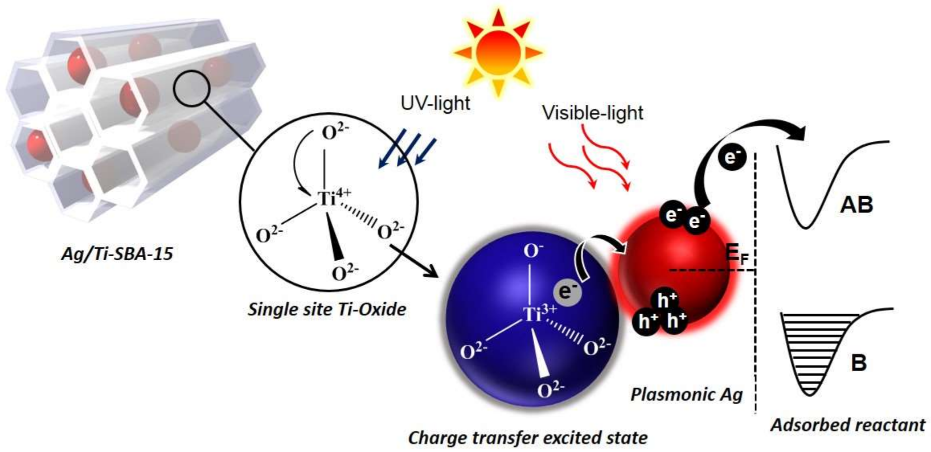

Scheme 1. Illustration of the light-induced charge transfer pathway on the prepared catalyst under UV and visible light irradiation (B: Bonding AB: Antibonding).

For Ag NPs, this resonant condition falls into the visible region of spectrum. Upon UV light irradiation of 200-270 nm, the Ti oxide moieties undergo excitation and form an excited charge transfer state that leads to the formation of trapped hole centres (O^-) and electron centres (Ti^{3+}). The location of e^- - h^+ pairs within the charge transfer excited state is much near to each other as compared to bulk TiO_2 semiconductor, accounting for its unique photocatalytic activity. The creation of heterojunction between Ag and Ti-oxide moieties can exploit both UV and visible light irradiation as illustrated in Scheme 1 by possible charge transfer from the excited Ti-oxide moieties to plasmonic Ag nanostructure to further antibonding molecular orbital of AB. This charge/electron relay enhances the cleavage of B-N bond in AB and hence the overall rate of hydrogen production. As shown in Figure 6, XPS measurement analysis also confirms the possible interactions between the species due to change in the position of B.E.

7.4 Conclusions

In conclusion, a novel catalyst, based on tetrahedrally coordinated Ti-oxide moieties and plasmonic Ag, was designed with superior optical and catalytic activities. The reaction rate for AB dehydrogenation of 3.3 μmol min^{-1} was observed under light irradiation conditions which was almost six times higher than that of Ag/TiO_2/SBA-15 having octahedrally coordinated Ti-oxide moieties and twice to that of Ag/SBA-15 catalyst without Ti species. The superior catalytic activity of Ag/Ti-SBA-15 was attributed to the combined effect of UV and visible light absorption and synergistic interaction between the two components. The high catalytic activity also arises from the optimum doping amount of Ti-oxide moieties within the framework and the associated effective charge relay derived from both photo-responsive components. I hope this work can felicitate the designing of new catalysts by fulfilling the ideal condition of efficiently utilizing solar energy to foster clean photocatalytic system.

7.5 References

[1] M. A. Garcia, *J. Phys. D: Appl. Phys.*, 2011, **44**, 283001.

[2] M. L. Brongersma, N. J. Halas and P. Nordlander, *Nat. Nanotechnol.*, 2015, **10**, 25.

[3] A. Tanaka, K. Hashimoto and H. Kominami, *J. Am. Chem. Soc.*, 2014, **136**, 586.

[4] H. Yamaguchi, M. Ikeda, K. Matsuda and M. Irie, *Bull. Chem. Soc. Jpn.*, 2006, **79**, 1413.

[5] J. G. Smith, J. A. Faucheaux and P. K. Jain, *Nano Today*, 2015, **10**, 67.

[6] (a) Z. Yan, Z. Wang, Z. Miao and Y. Liu, *Anal. Chem.*, 2016, **88**, 922; (b) J. A. Fan, C. Wu, K. Bao, J. Bao, R. Bardhan, N. J. Halas, V. N. Manoharan, P. Nordlander, G. Shvets and F. Capasso, *Science*, 2010, **328**, 1135; (c) T.F. König, P. A. Ledin, J. Kerszulis, M. A. Mahmoud, M. A. El-Sayed, J. R. Reynolds and V. V Tsukruk, *ACS Nano*, 2014, **8**,

6182; (d) M. Long, Z. Chen, T. Zhang, Y. Xiao, X. Zeng, J. Chen, K. Yan and J. Xu, *Nanoscale*, 2016, **8**, 6290; (e) A. J. Wood, B. Chen, S. Pathan, S. Bok, C. J. Mathai, K. Gangopadhyay, S. A. Grant and S. Gangopadhyay, *RSC Adv.*, 2015, **5**, 78534.

[7] (a) P. Verma, Y. Kuwahara, K. Mori and H. Yamashita, *J. Mater. Chem. A*, 2015, **3**, 18889; (b) K. Mori, P. Verma, R. Hayashi, K. Fuku and H. Yamashita, *Chem. Eur. J.*, 2015, **21**, 11885; (c) K. Fuku, R. Hayashi, S. Takakura, T. Kamegawa, K. Mori and H. Yamashita, *Angew. Chem. Int. Ed.*, 2013, **52**, 7446; (d) P. Verma, Y. Kuwahara, K. Mori and H. Yamashita, *J. Mater. Chem. A*, 2016, **4**, 10142.

[8] (a) H. Cheng, T. Kamegawa, K. Mori and H. Yamashita, *Angew. Chem. Int. Ed.*, 2014, **53**, 2910; (b) H. Cheng, X. Qian, Y. Kuwahara, K. Mori and H. Yamashita, *Adv. Mater.*, 2015, **27**, 4616; (c) H. Cheng, M. Wen, X. Ma, Y. Kuwahara, K. Mori, Y. Dai, B. Huang and H. Yamashita, *J. Am. Chem. Soc.*, 2016, **138**, 9316.

[9] (a) R. Long, Y. Li, L. Song and Y. Xiong, *Small*, 2015, **11**, 3873; (b) Y. Shi, J. Wang, C. Wang, T. T. Zhai, W. J. Bao, J. J. Xu, X. H. Xia and H. Y. Chen, *J. Am. Chem. Soc.*, 2015, **137**, 7365.

[10] W. Xie and S. Schlücker, *Nat. Commun.*, 2015, **6**, 7570.

[11] (a) K. Mori, Y. Miura, S. Shironita and H. Yamashita, *Langmuir*, 2009, **25**, 11180; (b) T. Kamegawa, D. Yamahana, H. Seto and H. Yamashita, *J. Mater. Chem. A*, 2013, **1**, 891.

[12] H. Yamashita and K. Mori, *Chem. Lett.*, 2007, **36**, 348.

[13] T. Kamegawa, N. Suzuki, M. Che and H. Yamashita, *Langmuir*, 2011, **27**, 2873.

[14] (a) Y. Kuwahara, D. Y. Kang, J. R. Copeland, P. Bollini, C. Sievers, T. Kamegawa, H. Yamashita and C. W. Jones, *Chem. Eur. J.*, 2012, **18**, 16649; (b) Y. Kuwahara, D. Y. Kang, J. R. Copeland, N. A. Brunelli, S. A. Didas, P. Bollini, C. Sievers, T. Kamegawa, H. Yamashita and C. W. Jones, *J. Am. Chem. Soc.*, 2012, **134**, 10757; (c) Y. Kuwahara, K. Nishizawa, T. Nakajima, T. Kamegawa, K. Mori and H. Yamashita, *J. Am. Chem. Soc.*, 2011, **133**, 12462.

[15] H. Yamashita and M. Anpo, *Curr. Opin. Solid State Mater. Sci.,* 2003, **7**, 471.

[16] H. Yamashita, M. Honda, M. Harada, Y. Ichihashi, M. Anpo, T. Hirao, N. Itoh and N. Iwamoto, *J. Phys. Chem. B*, 1998, **102**, 10707.

[17] H. Yamashita, Y. Ichihashi, M. Harada, G. Stewart, M. A Fox and M. Anpo, *J. Catal.*, 1996, **158**, 97.

[18] D. Zhao, J. Sun, Q. Li and G.D. Stucky, *Chem. Mater.*, 2000, **12**, 275.

[19] M. B. Gawande, S. N. Shelke, R. Zboril and R. S. Varma, *Acc. Chem. Res.*, 2014, **47**, 1338.

[20] Y. Kang, Y. Gong, Z. Hu, Z. Li, Z. Qiu, X. Zhu, P. M. Ajayan and Z. Fang, *Nanoscale*, 2015, **7**, 4482.

[21] D. Tsukamoto, Y. Shiraishi, Y. Sugano, S. Ichikawa, S. Tanaka and T. Hirai, *J. Am. Chem. Soc.,* 2012, **134**, 6309.

[22] G. Xue, Q. Dai and S. Jiang, *J. Am. Chem. Soc.,* 1988, **110**, 2393.

[23] A. Barrie and N. E. Christensen, *Phys. Rev. B*, 1976, **14**, 2442.

[24] R. Chaubey, S. Sahu, O. O. James and S. Maity, *Renew. Sustain. Energy Rev.*, 2013, **23**, 443.

[25] I. Dincer, *Int. J. Hydrogen Energy*, 2012, **37**, 1954.

[26] S. Dutta, *J. Ind. Eng. Chem.,* 2014, **20***,* 1148.

[27] E. S. Cho, A. M. Ruminski, S. Aloni, Y.-S. Liu, J. Guo and J. J. Urban, *Nat. Commun.*, 2016, **7**, 10804.

[28] W. Wang, T. B. Rauchfuss, L. Bertini and G. Zampella, *J. Am. Chem. Soc.*, 2012, **134**, 4525.

[29] A. Chinnappan, J. M. C. Puguan, W.-J. Chung and H. Kim, *J. Power Sources*, 2015, **293**, 429.

[30] C.-C. Chou, C.-H. Hsieh and B.-H. Chen, *Energy*, 2015, **90**, 1973–1982.

[31] Z. Wu, C. Tang, P. Zhou, Z. Liu, Y. Xu, D. Wang and B. Fang, *J. Mater. Chem. A*, 2015, **3**, 13050.

[32] Y. Yang, Y. Liu, Y. Li, M. Gao and H. Pan, *Chem. Asian J.*, 2013, **8**, 476–481.

[33] (a) E. K. Abo-Hamed, T. Pennycook, Y. Vaynzof, C. Toprakcioglu, A. Koutsioubas and O. A. Scherman, *Small*, 2014, **10**, 3145; (b) M. Chandra and Q. Xu, *J. Power Sources*, 2006, **156**, 190.

[34] K. Mori, T. Taga and H. Yamashita, *ChemCatChem*, 2015, **7**, 1285.

[35] Q. L. Zhu, D.C. Zhong, U. B. Demirci and Q. Xu, *ACS Catal.*, 2014, **4**, 4261.

[36] L. Yang, J. Su, X. Meng, W. Luo and G. Cheng, *J. Mater. Chem. A*, 2013, **1**, 10016.

[37] M. Li, J. Hu, Z. Chen and H. Lu, *RSC Adv.*, 2014, **4**, 41152.

[38] W. W. Zhan, Q. L. Zhu and Q. Xu, *ACS Catal.*, 2016, **6**, 6892.

[39] Y. Yamada, K. Yano, Q. Xu and S. Fukuzumi, *J. Phys. Chem. C.,* 2010, **114**, 16456.

[40] J. Li, Q.-L. Zhu and Q. Xu, *Catal. Sci. Technol.*, **2015**, 5, 525.

[41] W. Chen, J. Ji, X. Feng, X. Duan, G. Qian, P. Li, X. Zhou, D. Chen and W. Yuan, *J. Am. Chem. Soc.*, 2014, **136**, 16736.

[42] C. Y. Peng, L. Kang, S. Cao, Y. Chen, Z. S. Lin and W. F. Fu, *Angew. Chem. Int. Ed.*, 2015, **54**, 15725.

[43] K. Mori, K. Miyawaki and H. Yamashita, *ACS Catal.*, 2016, **6**, 3128.

[44] D. Zhao, J. Feng, Q. Huo, N. Melosh, G.H. Fredrickson, B.F. Chmelka and G.D. Stucky, *Science,* 1998, **279**, 548.

[45] X. Qian, T. Kamegawa, K. Mori, H. X. Li and H. Yamashita, *J. Phys. Chem. C,* 2013, **117**, 19544.

[46] P. Christopher, H. Xin and S. Linic, *Nat. Chem.*, 2011, **3**, 467.

Chapter VIII

General Conclusions

The research work carried out in the present PhD thesis dealt with designing of the Ag based visible light sensitive plasmonic materials supported on mesoporous silica for variety of application reactions. Various combinations of bimetallic systems have been studied combining the LSPR effect of Ag in order to exploit the broad spectrum range of solar radiation reaching the surface of earth. A representative image of plasmonic metal NPs explored for three catalytic reactions in the entire thesis under visible light irradiation is shown in Figure 1.

In Chapter I, the author has explained the basics of localized surface plasmonic resonance (LSPR) effect followed by its application in conventional catalytic reactions. The recent research work has been cited for better understanding of the research field. The possible mechanistic pathways by hot electrons and holes has been explained.

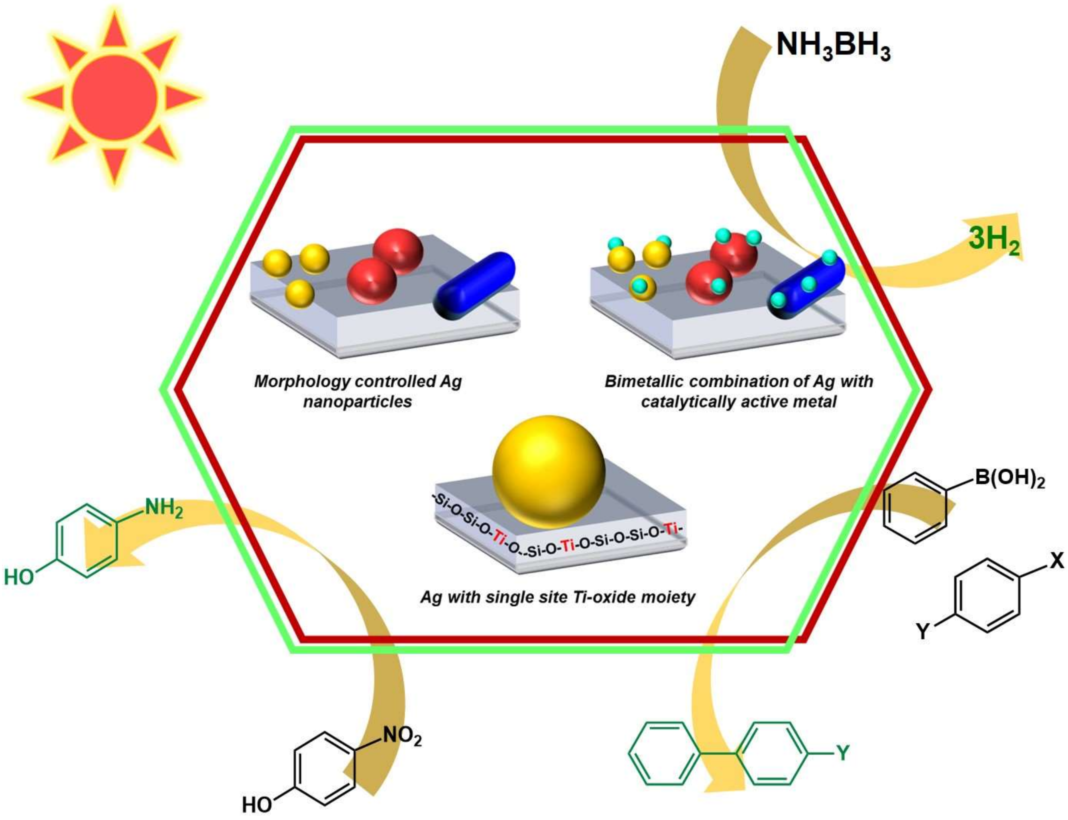

Figure 1. Plasmonic metal NPs supported on mesoporous silica explored for various catalytic reactions under light irradiation conditions.

Chapter II dealt with the size and color controlled Ag NPs and nanorods synthesized within the channels of mesoporous silica by rapid and uniform microwave-assisted alcohol reduction method in the presence and absence of surface modifying organic ligands. It was found that smaller NPs displayed higher catalytic activities in ammonia borane dehydrogenation under dark, whereas the catalytic performance under light irradiation increased with the increasing size of Ag NPs. The blue nanorods in particular showed the maximum enhancement due to their light absorption intensity owing to Ag-LSPR effect. A similar tendency in the LSPR-enhanced catalytic activity was observed in the tandem reaction consisting of dehydrogenation of AB and hydrogenation of 4-nitrophenol. Furthermore, the effect of light irradiation and temperature was studied in order to rule out the thermal effect arising from infrared light irradiation. The mechanism of reaction was also explored by studying the effect of charge scavengers and hence concluded that dehydrogenation of AB is promoted by the change of charge density of Ag NP derived from LSPR.

The previous study described in Chapter II was extended from monometallic to bimetallic system in Chapter III. The size and color controlled Ag NPs and nanorods were deposited by Pd NPs on the surface, to create an efficient and synergistic bimetallic catalytic system for increased activities and enhancements under light irradiation conditions. An LSPR-assisted method was established to carry out efficient deposition of Pd NPs on plasmonic Ag NPs under visible light irradiation. The bimetallic catalysts were characterized by HAADF-TEM, UV-Vis, FT-EXAFS, N_2 physisorption and X-ray diffraction analysis. Pd/Ag bimetallic catalysts were explored for ammonia borane dehydrogenation and Suzuki-Miyaura coupling reaction at room temperature. The order of increasing catalytic activity was found to be in accordance with the Ag-LSPR absorption intensity.

Chapter IV included the case of another bimetallic system of plasmonic Ag NPs with catalytically active Pt metal NPs. The Pt/Ag plasmonic catalyst supported on mesoporous silica found to exhibit maximum enhancement for 0.25 wt % of Pt deposited on Ag. The enhanced reaction rate was explained by a plausible reaction pathway for the hot electrons in the ammonia borane dehydrogenation. The effects of temperature and light were also carefully studied and explained, in order to elucidate the effect of thermal infrared heating. The recyclability of the catalyst was also investigated by doing reaction up to three runs in dark and under light irradiation conditions.

Chapter V the author performed the synthesis and characterization of series of bimetallic catalysts M/Ag/SBA-15 on Ag nanorods, where M = Ru, Ni, Co and Pd. Ru/Ag/SBA-15 found to exhibit the most active catalytic activities in the ammonia borane dehydrogenation and nitrophenol reduction reaction. However, Pd/Ag/SBA-15 displayed maximum enhancements under light irradiation conditions. The remarkable enhancement and catalytic activity were attributed to the synergistic bonding of Ag with Ru, Pd, Ni, Co and their light absorption intensity in the UV-vis spectroscopy. In addition, Ru/Ag/SBA-15 showed high stability for the hydrogen production from AB up to four consecutive runs.

In Chapter VI, the research on Pd/Ag bimetallic NPs has been extended and compared systematically with Pd/Au NPs. The bimetallic heterojunction was confirmed by X-ray photoelectron spectroscopy (XPS), and further characterized by TEM, FT-EXAFS and UV-vis spectra. Mesoporous silica supported Pd/Ag and Pd/Au NPs were explored for their plasmonic and catalytic activities in the hydrogen production from ammonia borane and Suzuki-Miyaura coupling reaction. Furthermore, a plausible mechanism of plasmonic catalysis was also proposed, in which the electron transfer from the plasmonic metal to active Pd species and then to adsorbed organic molecules enhances the bond weakening of the reactant molecules.

Finally, Chapter VII dealt with the synthesis of Ag-plasmonic catalyst supported on single site Ti-oxide modified mesoporous silica material. UV active Ti-oxide moiety combined with visible light sensitive plasmonic Ag NPs to design an efficient photocatalytic system utilizing broad spectrum of solar energy. A reaction rate for AB dehydrogenation of 3.3 μmolmin^{-1} was observed under light irradiation, which is almost six times higher than that of Ag/TiO$_2$/SBA-15 having octahedrally coordinated Ti-oxide moieties and twice that of Ag/SBA-15 catalyst without Ti species. The superior catalytic activity of Ag/Ti-SBA-15 was attributed to the combined effect of UV and visible-light absorption and synergistic interaction between the two components. Furthermore, effect of light filter, non-plasmonic active metal, method of NP deposition, mol % ratio of Ti-oxide were also investigated.

The field of plasmonics has grown dramatically over the past decade and new directions are continuously emerging. This thesis has only covered a brief snapshot of mono and bimetallic Ag and Au based nanocatalysts for their efficient catalysis under visible light irradiation. The catalysts of plasmonic nanostructures that exploits extreme light concentration and manipulation are witnessing particularly rapid developments and show significant future promise. In spite of significant advances on SPR-based photocatalysis, the extent of research work undertaken is still less compared to that of conventional catalytic studies. Novel approaches for the synthesis and study of plasmonic nanoarchitectures with controlled morphology are highly desirable. The mechanism underlying plasmonic enhancement, however, remain inconsistent within the field. In the first chapter of present thesis, I have summarized several possible mechanisms that have been put forth previously in the literature, namely charge transfer and local electric field enhancement. While most of these aspects have been studied in some detail, it is difficult to compare the results of different studies because of the wide range in materials preparation and properties. Further studies are needed in order to fully understand these effects and to optimize this phenomenon for maximum photoconversion efficiency.

Although this branch of plasmonic science and technologies research has witnessed significant efforts in the past two decades, new hypotheses needs to be developed that provides the conceptual framework to understand the photochemical processes on plasmonic nanoparticles. There are still a number of issues that have yet to be addressed. Some future outlooks to further broaden this research area can be to identify how different sites in a reactive system affect the reaction mechanisms. Another important area is to find the mechanism responsible for the above-mentioned transfer of charge from an excited nanoparticle to an adsorbate molecules. Although the above stated issues are important, the commercial impact of this field ultimately depends on ability to demonstrate chemical transformations on plasmonic metal nanoparticles. Recent progress in theoretical quantum chemical analysis of surface chemical transformations on metals (for example, density functional theory, time-dependent density functional theory and different variations of these) also represent a reasonable starting point for such models.

List of Publications

[1] Kohsuke Mori, Priyanka Verma, Ryunosuke Hayashi, Kojirou Fuku and Hiromi Yamashita,
"Color-controlled Ag nanoparticles and nanorods within confined mesopores: Microwave-assisted rapid synthesis and application in plasmonic catalysis under visible-light irradiation",
Chem. Eur. J., 2015, **21**, 11885-11893.

[2] Priyanka Verma, Yasutaka Kuwahara, Kohsuke Mori and Hiromi Yamashita,
"Synthesis and characterization of Pd/Ag bimetallic nanocatalyst on SBA-15 mesoporous silica as a plasmonic catalyst",
J. Mater. Chem. A, 2015, **3**, 18889-18897.

[3] Priyanka Verma, Yasutaka Kuwahara, Kohsuke Mori and Hiromi Yamashita,
"Pd/Ag and Pd/Au bimetallic nanocatalysts on mesoporous silica for plasmon-mediated enhanced catalytic activity under visible light irradiation",
J. Mater. Chem. A, 2016, **4**, 10142-10150. **[Front cover]**

[4] Priyanka Verma, Kaile Yuan, Yasutaka Kuwahara, Kohsuke Mori and Hiromi Yamashita,
"Enhancement of plasmonic activity by Pt/Ag bimetallic nanocatalyst supported on mesoporous silica in the hydrogen production from hydrogen storage material",
Appl. Catal. B., 2017, DOI: 10.1016/j.apcatb.2017.05.017.

[5] Priyanka Verma, Yasutaka Kuwahara, Kohsuke Mori and Hiromi Yamashita,
"Synthesis of mesoporous silica supported Ag nanorods-based bimetallic catalysts and investigation of their plasmonic activity under visible light irradiation",
Catal. Sci. Technol., 2017, **7**, 2551-2558.

[6] Priyanka Verma, Yasutaka Kuwahara, Kohsuke Mori and Hiromi Yamashita,
"Enhancement of Ag-based plasmonic photocatalysis in the hydrogen production from ammonia borane by the assist of single-site Ti-oxide moiety within the silica framework",
Chem. Eur. J., 2017, **23**, 3616-3622. **[Front Cover]**

<Related works>

[7] PMK Reddy*, Priyanka Verma* and Ch. Subrahmanyam, (*equal contribution)
"Bio-waste derived adsorbent material for methylene blue adsorption",
J. Taiwan Inst. Chem. Eng., 2016, **58**, 500-508.

[8] Kohsuke Mori, Priyanka Verma, Yasutaka Kuwahara and Hiromi Yamashita,
"Plasmonic photocatalyst using nano-porous Space",
Chemical Industry, 2016, **67**, 51-56. (Review article, ISSN: 0451-2014)

[9] Divya Mathur, S. Bhatia, Priyanka Verma, Rajendra Saxena, Virendra Parmar and Ashok K Prasad,
"Diastereoselective Acetylation Studies on 4-C-hydroxymethyl-1, 2-O-isopropylidene-3-O-alkyl-β-L-threo-pentofuranose: Key Precursor for Biocompatible Sugar-PEG Copolymers",
Trends in Carbohydrate Research, 2011, **3**, 42-50.

[10] Miriam Navlani-García, Priyanka Verma, Yasutaka Kuwahara, Kohsuke Mori and Hiromi Yamashita,
"Morphology-controlled Pd nanocrystals as catalysts in tandem dehydrogenation-hydrogenation reactions",
J. Chem. Sci., 2017, in press.

[11] Priyanka Verma, Miriam Navlani-García, Yasutaka Kuwahara, Kohsuke Mori and Hiromi Yamashita,
"Mesoporous silica supported PdAg bimetallic nanoparticles as a plasmonic catalyst for chemoselective hydrogenation of p-nitrostyrene under visible light irradiation",
J. Chem. Sci., 2017, in press.

Acknowledgement

The author, Priyanka Verma, wishes to express her deepest gratitude to Professor Hiromi Yamashita for the instructive guidance and encouragement throughout the present work. Heartily thanks are made to Professor Shinji Fujimoto (Division of Materials and Manufacturing science, Graduate School of Engineering, Osaka University), and Professor Tohru Sekino (The Institute of Scientific and Industrial Research, Osaka University), who acted as examiner of the dissertation, for their helpful and useful suggestions.

The author wishes to thank Associate Professor Kohsuke Mori (Division of Materials and Manufacturing Science, Graduate School of Engineering, Osaka University) for his encouragement, numerous discussions and insightful suggestions. I would like to thank Assistant Professor Yasutaka Kuwahara (Division of Materials and Manufacturing Science, Graduate School of Engineering, Osaka University), for his suggestions, support, encouragement and fruitful advises. I am also indebted to Technical Officer Tetsutaro Ohmichi (Division of Materials and Manufacturing Science, Graduate School of Engineering, Osaka University) and Office administrator Natsuko Hirozawa (Division of Materials and Manufacturing Science, Graduate School of Engineering, Osaka University) for their support throughout my stay in Yamashita laboratory.

I would also like to acknowledge Mr. Ryunosuke Hayashi and Mr. Kaile Yuan for their experimental assistance and lively discussion. I owe my sincere gratitude to all my colleagues Assistant Prof. Miriam Navlani García, Assistant Prof. Meicheng Wen, Dr. Ai Nozaki, Mr. Kazuki Nakatsuka, Mr. Yusuke Isaka, Mr. Haibo Yin and all other lab members and students whom I met in this laboratory led by Professor Hiromi Yamashita during the period of 3 years.

This study was supported financially by the 'Project for **F**uture **R**esearchers at **I**ITH to **E**nhance **N**etwork **D**evelopment with **S**cholarship of Japan (FRIENDSHIP)' via Japan International Corporation Agency (JICA). I would like to thank all the JICA coordinators who have helped me in the during the course of my study in Japan. My acknowledgments to Dr. Junko Komoto, Ms. Junko Yamanoi, Mr. R.S. Sreekanth, Ms. Miki Matsuo and Ms. Yuko Yokota.

Last but not the least, I wish to thank my parents, Meena Verma and Kamal Kishore Verma, brother and beloved family for their constant support and encouragement.

Priyanka VERMA
June, 2017